TECHNISCHE UNIVERSITÄT DRESDEN

Nonlinear electronic conductivity in lithium niobate domain walls

Master-Arbeit
zur Erlangung des Hochschulgrades
Master of Science
im Master-Studiengang Physik

vorgelegt von

Manuel Peter Zahn
geboren am 01.01.1997 in Dresden

Institut für Angewandte Physik
Fakultät Physik
Bereich Mathematik und Naturwissenschaften
Technische Universität Dresden
2022

Eingereicht am 31.01.2022
Persistent Identifier: urn:nbn:de:bsz:14-qucosa2-776392

1. Gutachter: Prof. Dr. Lukas M. Eng
2. Gutachter: PD Dr. Stephan Krohns

Abstract

Applying ferroelectric materials for nanoelectronic circuits opens, next to exploiting completely new functionalities, the possibility of improving resource efficiency in electronic circuits. Due to its defined and easy-to-manipulate domain structure, lithium niobate ($LiNbO_3$, LNO) is a promising candidate to realize such circuits. As a prerequisite, a detailed understanding of the underlying conduction mechanisms is required for a future large scale application.

The main field of attention of this thesis is the domain wall conductivity in lithium niobate, investigated with temperature-dependent dc conductivity measurements as well as higher-harmonic current analysis under alternating-voltage excitation. Thereby the parameters of the electric field are of special interest, comprising the static dc field and both the amplitude and the frequency of the ac excitation voltage. Prior to the analysis of the experimental results, the setups are characterized in depth and a theoretical framework to calculate higher-harmonic current contributions generated by non-ohmic conduction models is derived.

In case of high static offset voltages, an ohmic-like conductance is observed, which is ascribed to the intrinsic conductivity of the domain wall. For lower static offset fields, a diode-like current-voltage characteristic is found, originating from the junction of the domain wall and the metallic contact electrode. The results are compared to measurements at an industrial Schottky diode taken under the same conditions. Based on the theory of metal-semiconductor junctions, the effective donor density within the conducting domain wall is estimated to be of the order of $10^{19}/\mathrm{cm}^3$, which agrees well with theoretical calculations in the literature.

An equivalent circuit based on two diodes and two resistors is proposed to model the observed non-ohmic conductance. For all experimental techniques, a good agreement between this model and the experimental data is observed, proving especially the non-ohmic conductivity to be of Schottky-type.

Kurzfassung

Der Einsatz von ferroelektrischen Materialien in nanoelektronischen Anwendungen bietet neben der Erschließung ganz neuer Funktionalitäten die Möglichkeit, zukunftsweisende Wege für die Bereitstellung ressourceneffizienter Bauelemente zu finden. Durch seine einfachen und gut kontrollierbaren Domänen und Domänenwände ist Lithiumniobat ($LiNbO_3$, LNO) ein geeignetes Material zur Realisierung und Untersuchung beispielhafter elektronischer Schaltungen. Für einen erfolgreichen praktischen Einsatz ist ein detailliertes Verständnis der beteiligten Leitungsmechanismen notwendig.

Schwerpunkt der Arbeit bildete daher die Untersuchung der Leitfähigkeit der ferroelektrischen Domänenwände in Lithiumniobat mittels temperaturabhängiger Gleichstrom-Leitfähigkeitsmessungen sowie der Messung der Grund- und Oberwellen des Stromes bei Wechselstrom-Anregung. Dabei stand insbesondere die Variation der Parameter des elektrischen Felds, bestehend aus Gleichspannung sowie - für die Wechselstrommessungen - Amplitude und Frequenz des Wechselfeldanteiles, im Vordergrund. Vor der Analyse der experimentellen Ergebnisse erfolgte eine umfangreiche Charakterisierung der verwendeten Versuchsaufbauten und die Herleitung des theoretischen Gerüsts für die Berechnung von Oberwellen bei nichtlinearer Leitfähigkeit.

Bei hoher Gleichspannung wurde einerseits eine ohmsche Leitfähigkeit beobachtet, welche auf die intrinsische Leitung in der Domänenwand zurückgeführt werden kann. Bei geringer Gleichspannung hingegen konnte eine diodenartige Leitfähigkeit nachgewiesen werden, welche auf den Kontakt zwischen Domänenwand und metallischer Elektrode zurückgeführt wurde. Die Ergebnisse wurden mit Referenzmessungen an einer industriellen Schottky-Diode verglichen. Die Theorie der Metall-Halbleiter-Kontakte erlaubte die Bestimmung der effektive Donatorendichte in der Domänenwand, welche mit etwa $10^{19}/\mathrm{cm}^3$ mit Ergebnissen theoretischer Berechnungen aus der Literatur gut übereinstimmt.

Zur Modellierung der nichtlinearen elektronischen Leitfähigkeit wurde ein Ersatzschaltbild vorgeschlagen, bestehend aus zwei Dioden und zwei Widerständen. Über alle experimentellen Methoden hinweg, konnte eine hohe Übereinstimmung der Ergebnisse mit dem Model festgestellt und insbesondere der Charakter der Nichtlinearität als Schottky-artig bestätigt werden.

Contents

List of symbols, glossary, and conventions

$\mathbf{A_T}$	transimpedance, amplification of a current-voltage (IV)-converter, $[A_T] = \mathrm{V/A}$.
cutoff frequency	characteristic frequency of an electronic circuit element, where the amplitude reaches a damping of $-3\,\mathrm{dB}$ below a reference level, commonly applied for high-pass and low-pass filters.
$\boldsymbol{\delta}_Z$	dielectric loss angle. It is defined as the angle in the complex plane between the impedance $\mathbf{Z}$ and the negative imaginary axis (coincides with the direction of an ideal capacitor).
$\mathbf{E_a}$	activation energy, $[E_a] = \mathrm{eV}$.
$\boldsymbol{\epsilon}$	permittivity, also expressed as relative permittivity $\varepsilon_r = \varepsilon/\varepsilon_0$ with $\varepsilon_0 = 8.854 \cdot 10^{-12}\,\frac{\mathrm{As}}{\mathrm{Vm}}$ the permittivity of free space. $[\varepsilon] = \frac{\mathrm{A\,s}}{\mathrm{V\,m}}$.
HHCC	higher-harmonic current contributions, Fourier coefficients $m > 1$ of the electric current occuring when an electric one-port (two terminals) with non-ohmic current-voltage characteristic is excited by a sinusoidial voltage.
$\mathbf{I}$	current. A numerical index $m \in \mathbb{N}$ identifies the order for the case that a higher-harmonic contribution is considered. $[\mathrm{I}] = \mathrm{A}$.
$\mathbf{k_B}$	Boltzmann constant, $k_B = 1.381 \cdot 10^{-23}\,\mathrm{J/K}$ [1].
LIA	lock-in amplifier, extremly narrow-band amplifier at an externally provided fundamental frequency f_1. Recent devices can also amplify around an integer multiple of the fundamental frequency ("higher-harmonics") [2].
LNO	lithium niobate, $\mathrm{LiNbO_3}$, applied ferroelectric material within this thesis with 5 mol-%-MgO doping.
$\mathbf{n}$	ideality factor, characterizes the certain kind of deviation between the current-voltage-characteristic of a metal-semiconductor junction and the ideal Shockley equation (equ. 2.3).
$\mathbf{N_d}$	doping concentration, $[N_d] = 1/\mathrm{cm}^3$.
Nyquist diagram	plot of real part versus imaginary part of a complex quantity for all points obtained by varying a real value parameter. The Nyquist plot is commonly used to plot the impedance $\mathbf{Z}$ of a one-port circuit element while sweeping the frequency.
$\mathbf{q}$	elementary charge, $q = 1.602 \cdot 10^{-19}\,\mathrm{C}$ [1].
$\mathbf{R}$	resistance, real part of the complex impedance $\mathbf{Z}$.
$\mathbf{R^2}$	coefficient of determination. $R^2 \in (0, 1)$. It determines the quality of a (nonlinear) fit of a parametrized functional relationship to of

	measured data, while $R^2 = 1$ corresponds to perfect agreement. [3].
T	temperature, [T] = K.
THD	total harmonic distortion. Quantity to measure the quality of a sinusoidal signal. With given Fourier coefficients $I_1, I_2, ...$, the total harmonic distortion is defined as THD = $\sqrt{I_2^2 + I_3^2 + ...}/I_1$.
U	voltage. A numerical index $m \in \mathbb{N}$ identifies the quantity as the ac voltage amplitude of the mth harmonic order. [U] = V.
$\mathbf{U_c}$	characteristic voltage of a Schottky barrier. It is applied in the Shockley equation given in equ. 2.3.
X	reactance, imaginary part of the complex impedance **Z**.
Z	complex impedance, generalization of the resisance R for ac measurements with sinusoidal evolution of voltage and current over time, $\mathbf{Z} = R + \mathbf{i}X$, $[\mathbf{Z}]$ = V/A.

Furthermore, this thesis applies the following conventions:

- complex quantities are written in bold and roman letters;
- for quantities connected to ac measurements, amplitudes (e.g., U_m, $|\mathbf{I}_m|$) represent the root mean square value of the sine wave;
- the mth harmonic corresponds to a quantity oscillating with frequency mf_1 where f_1 being the fundamental excitation frequency. Non-oscillating dc quantities are interpreted as 0th-harmonic order;
- diagrams that display several harmonic orders, use a standardized color convention: m = 1: black (—), m = 2: red (—), m = 3: blue (—), m = 4: green (—), m = 5: gray (—), m = 6: orange (—), m = 7: teal (—), m = 8: lime (—).
- numerical values and their uncertainties are rounded according to the recommendations by the Particle Data Group [4].

1 Introduction

Ferroelectricity, the existence of strongly coupled switchable permanent dielectric dipoles within a solid material, is one of the longest-known long-range order phenomena. Similar to ferromagnetism, domains of equal electric dipole orientation (order parameter) are formed, separated by domain walls with fundamentally different physical properties. Since decades, ferroelectric materials have been investigated with respect to conduction mechanisms [5], dielectric [6], and optical properties. Due to these functional properties, ferroelectric materials are applied to a number of optical and nanoelectronic devices with substantial success. They facilitate realizing complex electronic circuits within a single material, and are candidates for resource-efficient nanoelectronics with closed-loop material supply chains. Within the upcoming field of nanotechnology, ferroelectric domain walls are intensively studied now, as they form a pseudo-2D system with potentially enhanced and tunable electrical conductivity [7].

A vast number of innovations during the last years are driven by the needs of computing technology, due to a continuously increasing demand of calculation capacities. For that reason, the computing industry by today already requires a noticeable and tremendously growing amount of resources [8] and will be the key industry to achieve the global sustainable development goals [9]. On the other hand, the exponential increase in computation power that was proposed as early as 1965 by Gordon Moore [10] and has hold for more than 40 years, has been slowed down in recent years, especially in terms of the computing frequency and the related single-thread performance [11]. Ferroelectric domain wall electronics is considered as one possible way to tackle these challenges, as it can in principle enable the integration of complex electronic circuits within a single material, providing compact and easy-to-recycle circuits [12].

A potential candidate material for these electronic applications is lithium niobate $LiNbO_3$ (LNO), which is in the main focus of the present thesis. Lithium niobate is widely applied in microwave filters (e.g., bulk acoustic wave filter, BAW), in nonlinear optics (e.g., second-harmonic generation), and in further electronic applications, e.g., in non-volatile memories [13]. Thereby, the domain walls, which have been proven to be conductive in 2012 [14], gained special interest. Compared to other ferroelectrics, the huge bulk vs. domain wall contrast in conductivity, which can easily reach several orders of magnitude, makes it a prominent candidate for the preparation of well-defined and

long-term domain arrangements. Godau *et al.* [15] demonstrated the possibility of efficient tuning and strong enhancement of LNO domain wall conductivity by electric fields.
The following experiments are motivated by current-voltage (IV)-curves as shown in fig. 1.1a, measured on a conductivity-enhanced LNO domain wall, macroscopically contacted with evaporated chromium electrodes. In contradiction to previous experiments by Godau *et al.* [15] and Thiessen [16], they exhibit pronounced non-ohmic and asymmetric IV-characteristics, which motivates to postulate the equivalent circuit shown in fig. 1.1b. It consists of two distinct current paths, each containing an intrinsic ohmic contribution by the domain wall and a diode-like part caused by the interface towards the metal electrodes (injection barrier). The red line in fig. 1.1a presents a fit according to the equivalent circuit model established in this thesis, indicating an excellent agreement with the measured data. Hence, it is the main goal of this thesis to investigate the characteristic parameters, i.e. the resistance, the diode saturation current and the characteristic diode voltage, of the components within the equivalent circuit model and their microscopic origin.

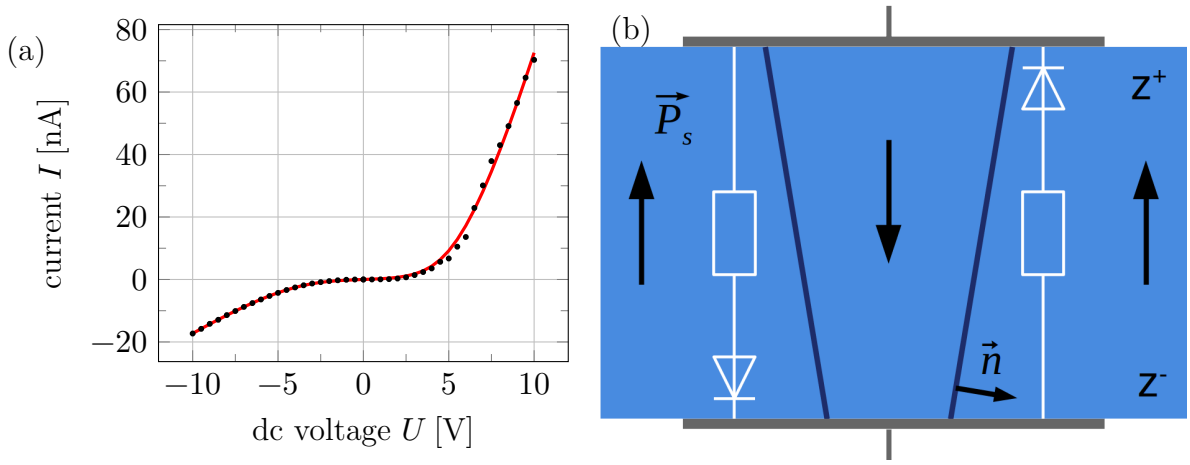

Figure 1.1: Non-ohmic dc conductivity of a conductive LNO domain wall. **(a)** Asymmetric IV-curve recorded for a macroscopically-contacted conductivity-enhanced LNO domain wall (sample *mz13c*, described in more detail in sec. 4.1). During the enhancement-process according to the protocol of Godau *et al.* [15], the conductivity increased by four orders of magnitude. **(b)** Equivalent circuit proposed in order to interpret the IV-curve shown in (a). The characteristic parameters of the involved circuit elements (resistance, saturation current, and characteristic voltage of the diodes) are investigated within this thesis. Due to the orientation of the permanent polarization $\vec{P}_s$, a head-to-head type domain wall is observed. $\vec{n}$ defines the orientation of the domain wall normal vector.

Lithium niobate can be considered as a semiconductor with a wide optically determined bandgap of 3.87 eV [17, 18]. Thermally activated hopping is the dominant conduction mechanism below room temperature, realized by small polarons [16, 19]. In turn, the metal-domain wall junctions on top and at the bottom of the device form metal-semiconductor

contacts, exhibiting typical features such as rectification. The theoretical details are summarized in chapter 2 later.
As a first major experimental method, temperature and voltage-dependent dc conductivity measurements were performed, adding a further dimension to the data shown in fig. 1.1a. The conductance is thereby either dominated by the intrinsic conduction or the injection barrier depending on the voltage range, and characterizing parameters can be determined for both contributions.
As a second method, dielectric spectroscopy was performed, focusing especially on the generation of higher-harmonic current responses due to the nonlinear conductivity behavior. Since the intrinsic domain wall conduction is assumed to be ohmic, this approach mostly provides insights into the metal-semiconductor junction (Schottky injection barrier). Similarities between an industrial Schottky diode and a LNO domain wall were found by sweeping parameters such as the ac amplitude, dc offset voltage and ac frequency. A quantity of high interest thereby is the characteristic diode voltage $U_c = nk_BT/q$, as it depends, under certain conditions, on the charge carrier density inside the "semiconductor", here the LNO domain wall.
All experiments were performed by home-built experimental setups, assembled or notably improved during the present thesis. Therefore, chapter 3 deals with the description and fundamental characterization of these setups and derives their possible application range. A major focus is the right selection of an appropriate lock-in amplifier (LIA) needed for dielectric spectroscopy and higher-harmonic current demodulation. The material specific results on LNO are shown in chapter 4.

2 Theoretical background and literature review

2.1 Fundamental properties of lithium niobate

Some key properties of lithium niobate, such as crystallographic structure, ferroelectricity, bulk and domain wall electrical conductivity are briefly introduced here.

At room temperature, lithium niobate ($LiNbO_3$, LNO) is an optically transparent solid. For temperatures below the ferroelectric transition that occurs between 1140 and 1200 K depending on chemical composition and doping, lithium niobate exhibits a threefold symmetry with respect to the z-axis. It is a member of the trigonal crystal system and belongs to the point group $3m$ [20]. The non-centrosymmetric structure defines a distinguishable orientation in z-direction and with that the z+ and z- side of the crystal. The lithium ions occur in two different stable positions within the unit cell. Together with the niobium ions they form a switchable permanent electric dipole moment of 75 - 80 µC/cm^2 [21].
Lithium niobate crystals are typically grown by the Czochralski technique from a melt of Li_2CO_3 and Nb_2O_5 powders. Depending on their ratio, the exact chemical composition may vary, while stoichometric ([Li]/([Li] + [Nb]) = 0.5) and congruent ([Li]/([Li] + [Nb]) = 0.484) compositions are the most common ones [22]. For all experiments considered here, congruent LNO with 5 mol-% Mg-doping was used. According to Gopalan *et al.* [5], magnesium atoms sit on the lithium vacancies and avoid the formation of Nb_{Li} (niobium atom on lithium position) anti-site defects, which results in a suppression of electron traps involving two electrons on neighboring atomic sides, termed bipolarons.
A huge number of electron traps are observed in LNO, acting as potential sites for electron hopping transport. These include atomic defects, e.g., iron impurities, as well as different kinds of polaronic excitations. Detailed characterizations are given by Gopalan *et al.* [5] and Thiessen [16]. Several electrical and optical investigations identified free small electron polaron hopping as the dominant current transport mechanism in bulk LNO crystals below room temperature [19, 23, 24]. Domain wall conductivity is observed only at inclined domain walls, as their head-to-head or tail-to-tail character attracts negative

or positive charge carriers, respectively. This is supported by theoretical calculations by Eliseev *et al.* [25] and Xiao *et al.* [26].
LNO exhibits weak bulk dark conductivity that strongly depends on the annealing conditions. Depending on the temperature range, different polaronic transport mechanisms are observed in congruent LNO [27]. Iron impurities have been identified to strongly influence these conduction properties in magnesium doped LNO, as they, e.g., contribute to the photoconductivity [28].
For the first time, domain wall conductivity in LNO was found by Schröder *et al.* [14] under super-bandgap illumination. Next to dc investigations, also ac conductivity was reported and investigated by Schröder *et al.* [29] at both the macroscopic and nanoscopic length scale, up to a frequency of 10 kHz. Based on these results, domain wall conductivity is also expected above 10 kHz, which is an important requirement for high frequency electronic circuits.
The inclination angle, and accordingly the dc conductivity of LNO domain walls, can be increased by several orders of magnitude when applying a further voltage pulse treatment in opposite direction to the poling field, as described by Godau *et al.* [15]. An alternative procedure to increase the domain wall conductivity was developed by Werner *et al.* [30]. Depending on the nanoscopic arrangement of the domain wall, the conductivity results to be long-term stable for several months, or shows decreasing domain wall conductivity. Lofty [31] faced this phenomenon and developed a categorization scheme for the temporal stability of LNO domain walls. Since the small polarons exhibit hopping-like transport, the theory of activated hopping transport is discussed in more detail in the next section.

2.2 Theory of activated hopping transport

One part of the present thesis deals with the in-depth analysis of the temperature-dependent conductivity of LNO's domain walls. Therefore, a comprehensive overview on possible thermally activated hopping mechanisms and their specific temperature dependencies is given in the following.

The general phenomenon of thermally activated conduction covers a broad range of mechanisms observed in disordered solids that show localized electronic states [32]. Thereby, the overlap of electronic wave functions of neighboring atoms is sufficiently small and a relevant tunneling barrier is formed between them.
In the experiments presented later, the electronic transport will be investigated by temperature-dependent dc conductivity measurements. Since this method offers a unique possibility to differentiate nanoscopic details of the effective transport mechanisms, the latter are categorized and discussed with respect to the expected functional dependence

of the conductivity $\sigma(T)$ that, in general, is expressed as:

$$\sigma(T) = \tilde{\sigma}_0 T^{-\alpha} \exp\left(-\left[\frac{T_0}{T}\right]^{\beta}\right). \tag{2.1}$$

Here, $\tilde{\sigma}_0$ is a constant prefactor related to the sample geometry, while T_0 is a characteristic temperature, which can be expressed via $T_0 = E_a/k_B$ as an energy E_a, also termed hopping activation energy. Especially the dimensionless coefficients α and β depend on the underlying nanoscopic processes and are therefore of special interest to be determined. First, three major groups of conductivity can be classified based on the coefficient β:

- $\beta = 1$**: Thermally activated hopping**
  The hopping sites are distributed randomly in real space, but equal in energy [33, 34]. This is especially the case, when the hopping sites are generated by a single type of impurities [35]. Hopping between neighboring sites is characterized by a hopping probability that only depends on the real space distance. Due to $\beta = 1$, the exponential term reduces to a Boltzmann-distribution-like expression. The density of states (DOS) close to the Fermi level is assumed to be constant.

- $\beta = \frac{1}{4}$**: Mott variable-range hopping**
  The hopping sites are still randomly distributed in real space, but furthermore, also randomly distributed in energy [36]. Consequently, the hopping probability P becomes a function of the real-space distance R and the energy difference ΔE between the hopping sites. It is typically given by:

  $$P \propto \exp\Big(\underbrace{-\tilde{\alpha}R - \frac{\Delta E}{k_B T}}_{:=\mathcal{R}}\Big), \tag{2.2}$$

  with $\tilde{\alpha}$ being the reciprocal typical dimension of the electronic orbitals, which are often considered to be s-character-like [36]. Due to the specific relation of R and ΔE in equ. 2.2, Mott variable-range hopping can be interpreted as a four-dimensional hopping process, with the energy difference acting as the additional dimension with different normalization. The inner expression of the exponential term in equ. 2.2 then reflects an effective distance in the extended vector space, and thus is termed range $\mathcal{R}$.

- $\beta = \frac{1}{2}$**: Efros–Shklovskii variable-range hopping**
  Efros and Shklovskii [37] extended the variable-range hopping model proposed by Mott [36] when considering the density of states (DOS) around the Fermi-level in more detail, since mostly these electrons contribute to the dc conductivity. A reduction of the DOS due to Coulomb interaction of the electrons is found, resulting

in a change to $\beta = \frac{1}{2}$.

Based on these fundamental types, numerous combinations of α and β may occur for real transport phenomena:

- $\alpha = 0$, $\beta = 1$: **Simple thermally-activated hopping**
  Thermally activated hopping with constant DOS close to the Fermi level.
- $\alpha = 0$, $\beta = \frac{1}{4}$: **Mott variable-range hopping**
  Hopping sites are randomly distributed in energy with constant DOS near the Fermi level [36]. Prototype of variable-range hopping.
- $\alpha = 0$, $\beta = \frac{1}{2}$: **Efros–Shklovskii variable-range hopping**
  Hopping sites are randomly distributed in energy with dominant Coulomb interactions, between electrons close to the Fermi level [37].
- $\alpha = 1$, $\beta = 1$: **Adiabatic polaron hopping**
  Polaronic transport with a large overlap integral between closest hopping sites [16]. The electrons can immediately follow the ionic motion, corresponding to the adiabatic limit of the Born-Oppenheimer approximation [38].
- $\alpha = \frac{3}{2}$, $\beta = 1$: **Non-adiabatic polaron hopping**
  Polaronic transport with a small overlap integral and therefore low hopping rates. The Born-Oppenheimer approximation is not fulfilled.
- $\alpha = 0.35$, $\beta = \frac{1}{4}$: **Variable-range hopping with constant distance**
  Mott variable-range hopping with constant real-space distance between the hopping sites. The formula was derived by a percolation-theory approach [39].
- $\alpha = \frac{9}{2}$, $\beta = \frac{1}{2}$: **Efros-Shklovskii hopping with polaronic pseudo-bandgap**
  Due to strong electron-phonon interaction, a smaller rigid gap appears in the DOS around the Fermi level, in addition to the Coulomb gap [40]. This transport mechanism is observed, e.g., in rare-earth manganites.

In general, the parameter β dominates the temperature dependence as it enters exponentially in equ. 2.1, while α enters via a power law only. Therefore, α is challenging to be determined and in most cases additional experimental techniques, e.g., optical methods such as photoluminescence analysis [19, 41], are required in order to specify a single transport mechanism precisely.

2.3 Metal-semiconductor junctions

Metal electrodes, evaporated or sputtered, are most commonly used as electrical contacts to ferroelectrics, and hence needed in any potential ferroelectric nano-electronic device. A selection of conduction models for metal-semiconductor junctions relevant to explain the non-ohmic conductivity observed at LNO domain wall-metal interfaces, and to determine the set of involved parameters, such as the ideality factor n, are introduced in this section.

Metal-semiconductor junctions are fundamental solid-state devices and are extensively studied within semiconductor theory. These studies generally consider classical semiconductors such as silicon (Si) or gallium arsenide (GaAs), but also can be transferred to LNO-metal junctions, as LNO exhibits a thermally activated electronic transport (realized by small polaron hopping [16]) as well. Despite under certain conditions a metal-semiconductor junction can exhibit ohmic IV-characteristics [42], the following considerations focus on the situation of a rectifying IV-curve (termed Schottky contact), in particular on a junction between a metal and a n-type semiconductor. This corresponds to a head-to-head domain wall in LNO, since the conductivity therein is realized by electron transport [26]. The relevant quantities influencing the junction's IV-characteristics are the work function of the metal on the one hand, and the band gap and the doping concentration N_d of the semiconductor on the other hand.
The band diagram of a Schottky contact is shown in fig. 2.1. In forward direction, the electrons are forced to pass from the semiconductor into the metal. A first description is given by the diffusion model, which is based on classical electrodynamics. Within this model, a diffusive charge-carrier motion due to thermal activation is superimposed by the electrostatic force due to the barrier potential. Despite its simplicity, the model already predicts correctly the electric current I as a function of applied voltage U, also known as Shockley diode equation [43]:

$$I = I_s \left[\exp\left(\frac{qU}{nk_BT} \right) - 1 \right] = I_s \left[\exp\left(\frac{U}{U_c} \right) - 1 \right]. \tag{2.3}$$

Thereby, I_s is the saturation current that will be discussed later, n is the ideality factor with $n = 1$ for the diffusion model, and $U_c = nk_BT/q$ the characteristic voltage of the Schottky barrier.
The second model, to be discussed in more detail, is the thermionic-emission theory, which interprets the transmission across the barrier as a combination of thermal activation and tunneling through the barrier on the activated energy level. Two extreme cases can be distinguished, where the temperature and the doping concentration of the semiconductor N_d have opposite influence on the dominating effect. According to Rhoderick and Williams [42], they can be distinguished by introducing an additional renormalized scale

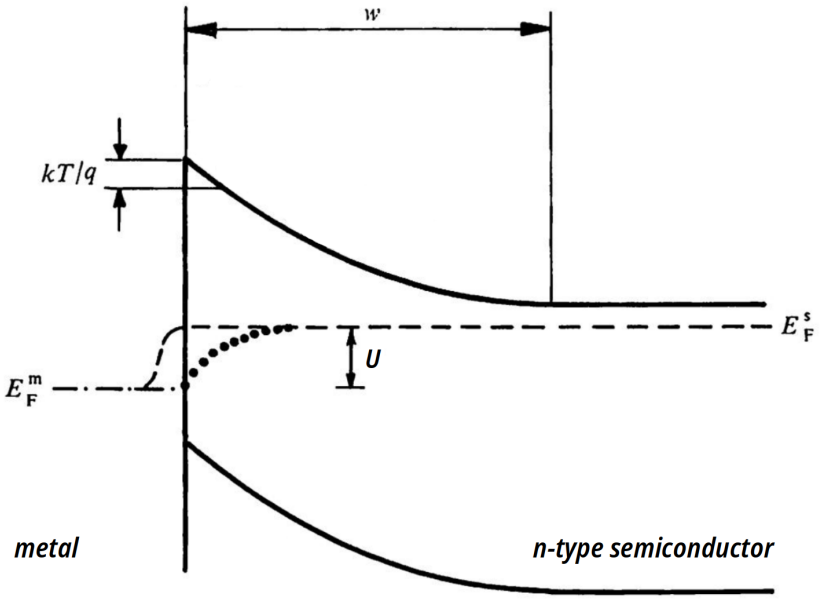

Figure 2.1: Band diagram of a forward-biased Schottky barrier with the semiconductor on the right hand side. The dashed line represents the evolution of the quasi-Fermi level between the metal E_F^m and the semiconductor E_F^s level, according to the thermionic emission theory, the circles represent the diffusion theory. U is the applied voltage and w the width of the barrier. Fig. reproduced from Rhoderick and Williams [42].

based on the effective mass $m^\star = m_0 m_r$ of the electrons and the dielectric permittivity of the semiconductor $\varepsilon = \varepsilon_0 \varepsilon_r$:

$$U_d = \frac{\hbar}{2}\left(\frac{N_d}{m^\star \varepsilon}\right)^{1/2}. \tag{2.4}$$

The so-called doping voltage U_d is related to the diodes characteristic voltage U_c via:

$$U_c = \frac{n k_B T}{q} = U_d \coth\left(\frac{qU_d}{k_B T}\right). \tag{2.5}$$

Whenever the temperature is high or the doping concentration is low ($k_B T \gg qU_d$), the electrons become dominantly highly activated and pass the barrier at energies where it is already narrowed down. This is termed thermionic-field emission with the extreme case that the electrons are thermally lifted over the barrier termed thermionic emission.
In the other case of low temperatures or high doping concentrations ($qU_d \gg k_B T$), the electrons get only weakly activated and tunnel through the full width of the barrier. This is called field emission and will turn out to be the dominant case on the domain wall-electrode junction later in sec. 4.2. Though the ideality factor n is between 1 and 2 for conventional semiconductors at room temperature, it can increase significantly in case

of thermionic-field emission. Since $U_c \approx U_d$, the ideality factor is given in this case by

$$n = \frac{q \cdot \hbar}{2k_B T}\sqrt{\frac{N_d}{m^\star \varepsilon}}. \tag{2.6}$$

Notably, there is no upper limit for n, provided the doping concentration is sufficiently high. Furthermore, the ideality factor can be used to estimate the (effective) doping concentration of a semiconductor, which will be done in sec. 4.2.
A remaining problem is the precise form and especially the temperature dependence of the saturation current I_s in equ. 2.3. According to Rhoderick and Williams [42], I_s appears as:

$$I_s = A^\star T^2 \exp\left(\frac{-q\Phi_{eff}}{k_B T}\right), \tag{2.7}$$

where Φ_{eff} is the effective potential barrier height and $A^\star$ is a material specific parameter, the so-called Richardson constant. As the Schottky barrier-like conductivity will be superimposed by a hopping transport as discussed in sec. 4.3 later on, it is worth to calculate the activation energy E_a with the following definition motivated by equ. 2.1 using $\beta = 1$ and $\alpha = 0$:

$$\begin{aligned}
E_a &:= -k_B \frac{\partial \ln I}{\partial 1/T} \\
&\underset{equ.2.3,2.7}{=} -k_B \frac{\partial}{\partial 1/T} \ln\left(A^\star T^2 \exp\left(\frac{-q\Phi_{eff}}{k_B T}\right)\left[\exp\left(\frac{qU}{nk_B T}\right) - 1\right]\right) \\
&= -k_B \frac{\partial}{\partial 1/T} \ln(A^\star T^2) - \cancel{k_B} \frac{\partial}{\partial 1/T}\left(\frac{-q\Phi_{eff}}{\cancel{k_B} T}\right) \\
&\quad - k_B \frac{\partial}{\partial 1/T} \ln\left(\exp\left(\frac{qU}{nk_B T}\right) - 1\right) \\
&= \underbrace{2k_B T + q\Phi_{eff}}_{:=E_0} - \underbrace{k_B T}_{:=A} \underbrace{\frac{q}{nk_B T}}_{:=1/U_c} U \frac{1}{1 - \exp\left(-\frac{qU}{nk_B T}\right)} \\
&= E_0 - A \cdot \frac{U/U_c}{1 - \exp(-U/U_c)}.
\end{aligned} \tag{2.8}$$

The last line will be used in the experimental part in sec. 4.3 to fit observed results and determine the parameters E_0, A, and U_c.
A different model for the saturation current was proposed by Tietze *et al.* [44], motivated by experimental results on semiconductors:

$$I_s(T) = I_s(T_0) \exp\left[\left(\frac{T}{T_0} - 1\right)\frac{qU}{nk_B T}\right]\left(\frac{T}{T_0}\right)^{\frac{x_{T,I}}{n}}. \tag{2.9}$$

Thereby $x_{T,I} \approx 2$ is a numerical constant and T_0 a reference temperature where $I_s(T_0)$ is known. Due to the increased complexity, the activation energy E_a can not be calculated

analytically, as obtained in the model discussed above. By numerical evaluation it is found that E_a has a Lorentzian-like maximum at $U = 0$.

2.4 Alternating-current measurements in solid-state physics

Alternating current measurements are performed in different scientific communities within the field of solid-state physics. Dielectric spectroscopy and precise measurements of IV-curves are introduced and compared here as being two main motivations to measure alternating currents. For each motivation, corresponding to a scientific community, a recently published example is discussed.

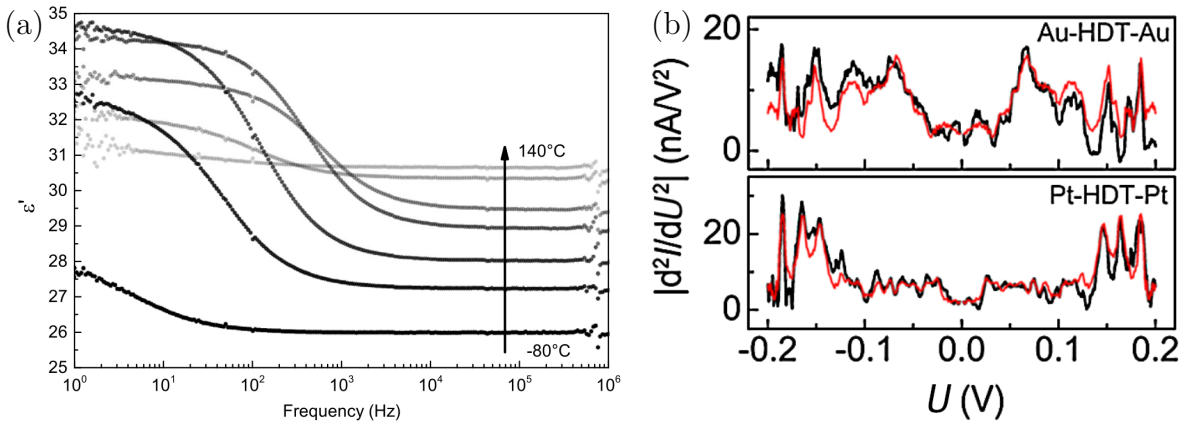

Figure 2.2: Examples for ac current measurements in solid-state physics. **(a)** Dielectric spectroscopy on mono-domain 5 % MgO-$LiNbO_3$ revealing a Debye-like relaxation with a temperature-dependent cutoff frequency. Figure reprinted from Meyer *et al.* [45]. $T = -80\,°C$, $0\,°C$, $40\,°C$, $80\,°C$, $100\,°C$, $130\,°C$ and $140\,°C$. **(b)** Precise measurement of the IV-characterictic of single molecule (1,6-hexanedithiol, HDT) contacts between gold and platinum electrodes (black). Since the curve is expected to be symmetric around $U = 0$, the red line represents the symmetrized curve obtained by $f_{sym}(U) = [f(U) + f(-U)]/2$. Figure reprinted from Kim *et al.* [46].

In general, the generation and detection of alternating currents is connected with several additional challenges as compared to direct-current measurements, e.g., finite bandwidths, harmonic distortion, and imperfect filter characteristics. Nevertheless, different motivations can be distinguished to apply ac measurements and tackle the consequences. Effects only appearing due to the alternating excitation voltages themselves are the first motivation. This field is known as dielectric spectroscopy and is applied to analyze liquids and gases as well. Typically, the frequency of the electric field is the most important

quantity to vary. A common task in dielectric spectroscopy is to determine the maximum frequency up to which the displaceable charged components within the crystal such as ions, electrons, or quantized excitations can follow the electric field due to their inertia. This results in distinguishable contributions to the permittivity or dielectric constant ε, revealing information on the local forces acting on these components.

A typical example for dielectric spectroscopy is shown in fig. 2.2a, realized on bulk MgO-doped LNO as it is investigated here as well. That image depicts the dielectric constant ε as a function of the alternating electric field frequency. According to Meyer *et al.* [45], within the investigated range, the maximum transfer frequency of the electrons contributing to hopping between neutral $Mg_{Li}^{\bullet}$ defects (using Kröger–Vink notation) and niobium sites is reached and a decrease of the dielectric constant is observed above this frequency. The maximum transfer frequency increases with temperature since the electrons get stronger activated resulting in a larger hopping frequency. It has to be noted that the observed transition frequencies lay within the expected frequency range of interface-barrier layer capacitors, especially generated on a single junction of LNO and one contact electrode. A clear distinction of internal and external contributions is therefore crucial for these kinds of measurements. A huge number of scientific instruments has been constructed especially for dielectric spectroscopy measurements, e.g., summarized by Krohns [47]. A similar investigation on a different ferroelectric material, namely $YMnO_3$, is reported by Ruff *et al.* [48].

As a second motivation for ac measurements, the precise quantification of phenomena in the IV-characteristics already existing under dc conditions is observed. In these cases, the frequency is chosen sufficiently large to achieve precise results and small enough to avoid side effects due to the alternating field as described above. As a most striking difference to dielectric spectroscopy, the frequency is kept constant and the chosen frequency value should not influence the observed results. The measurements are typically performed with lock-in amplifiers (LIAs) and appropriate IV-converters, providing uniquely high signal-to-noise ratios.

Within this motivation, further subgroups can be identified. A first sub-motivation is the reduction of low-frequency electronic noise in case of small signal amplitudes. These are, e. g., thermal (Johnson) and shot noise, described in more detail by Horowitz and Hill [49]. The ac investigation of dc phenomena is frequently used within electronic investigations of single molecules. Typical frequencies for this type of measurements are between 10 and 100 Hz.

A second sub-motivation is the identification of nonlinearities in IV-curves, which can be accomplished in principle by using a classical ampere-meter and measuring the absolute current. However, the following requested numerical differentiation of the IV-curve is sensitive to numerical errors. As summarized by Nandi *et al.* [50], quite a number

of electronic transport phenomena exhibit non-ohmic conductivity, even increasing by including heterostructures. As it is derived in app. C as a side result, weak non-ohmic conductivity ($\frac{\partial I}{\partial U} \gg U\frac{\partial^2 I}{\partial U^2}$) can be easily determined by applying an electric field of frequency f_1 and measuring the induced alternating electric currents at $f_2 = 2f_1$, $f_3 = 3f_1$ and so on - the higher-harmonic currents.

An example motivated by the identification of non-ohmic conductivity is shown in fig. 2.2b. Here, single HDT molecules are contacted between two gold or platinum electrodes, respectively. When applying an electric field, electrons move from the metal into an orbital state of the first atom, through the molecule and onto the other electrode. Whenever the voltage is high enough, electrons can excite a vibrational mode of the molecule. This equals to a second current path and the conductivity increases in some cases only by the order of 1 ‰, which is not detectable with a source-meter. However, clear peaks are observed in the second derivative of the IV-curve that is measured via the third harmonic current at frequency $3f_1$.

The experimental results presented later in sec. 4.4 are mainly motivated by both subgroups of the second motivation, so phenomena existing under dc conditions with (i) small signal amplitude and (ii) notable nonlinearities are investigated. This appears to be a new approach, as no similar results for ac measurements of dc properties on ferroelectric domain walls were found within the literature so far. Nevertheless, lock-in amplifier based dielectric spectroscopy, which will be introduced later, should be able to work under the first motivation, too. This is shortly discussed at the end of sec. 4.4.

3 Experimental details and instrumental developments

3.1 Temperature-dependent dc conductivity setup

The experimental setup for temperature-dependent dc conductivity measurements and the related parameter space is described. Experimental methods and chosen parameters are motivated.

Since the population of trap states within the band gap of insulators is heavily influenced by thermal activation, temperature-dependent investigations of numerous quantities - in particular the resistance - are the keys to understand their nanoscopic electronic transport behavior. It is therefore natural, to initiate also temperature-dependent conductivity investigations for conductive domain walls. This extends the experiments by Schröder [51] into two different directions. On the one hand, the conductivity-enhancement procedure developed by Godau *et al.* [15] enables order-of-magnitude larger domain wall conductivities, having potential to show fundamentally different properties. On the other hand, the performed $I(U,T)$ measurements add a further dimension to the one dimensional $I(T)|_{U=const.}$ experiments performed so far by Thiessen [16].
For the temperature-dependent experiments, an *Oxford Instruments Optistat DN* liquid nitrogen bath cryostat was used, as schematically depicted in fig. 3.1a. The temperature was measured by two independent PT100 platinum resistance sensors, one positioned at the heat exchanger and one directly next to the LNO sample. All functionalities of the cryostat, including gas flow regulation, heating control, and reading the temperature sensor at the heat exchanger, are covered by an *Oxford ITC 503* temperature controller, while the second temperature sensor next to the sample was read out by a *Keithley 196* Digital Multimeter. The current measurements themselves were performed in case of LNO domain-wall conductivity with a *Keithley 6517B* Electrometer in two-point geometry. Since the reference experiments with an industrial Schottky diode required measurements with small voltages, a *Keithley 2450* Sourcemeter was applied in the four-wire configuration for that case. To properly transmit electric signals, the applied sample rod (fig. 3.1b) is equipped with wires shielded up to the probe head. Further signals can be provided via

additional cables (not shielded within the vacuum part), which were, i.e., partially used for the second temperature sensor.

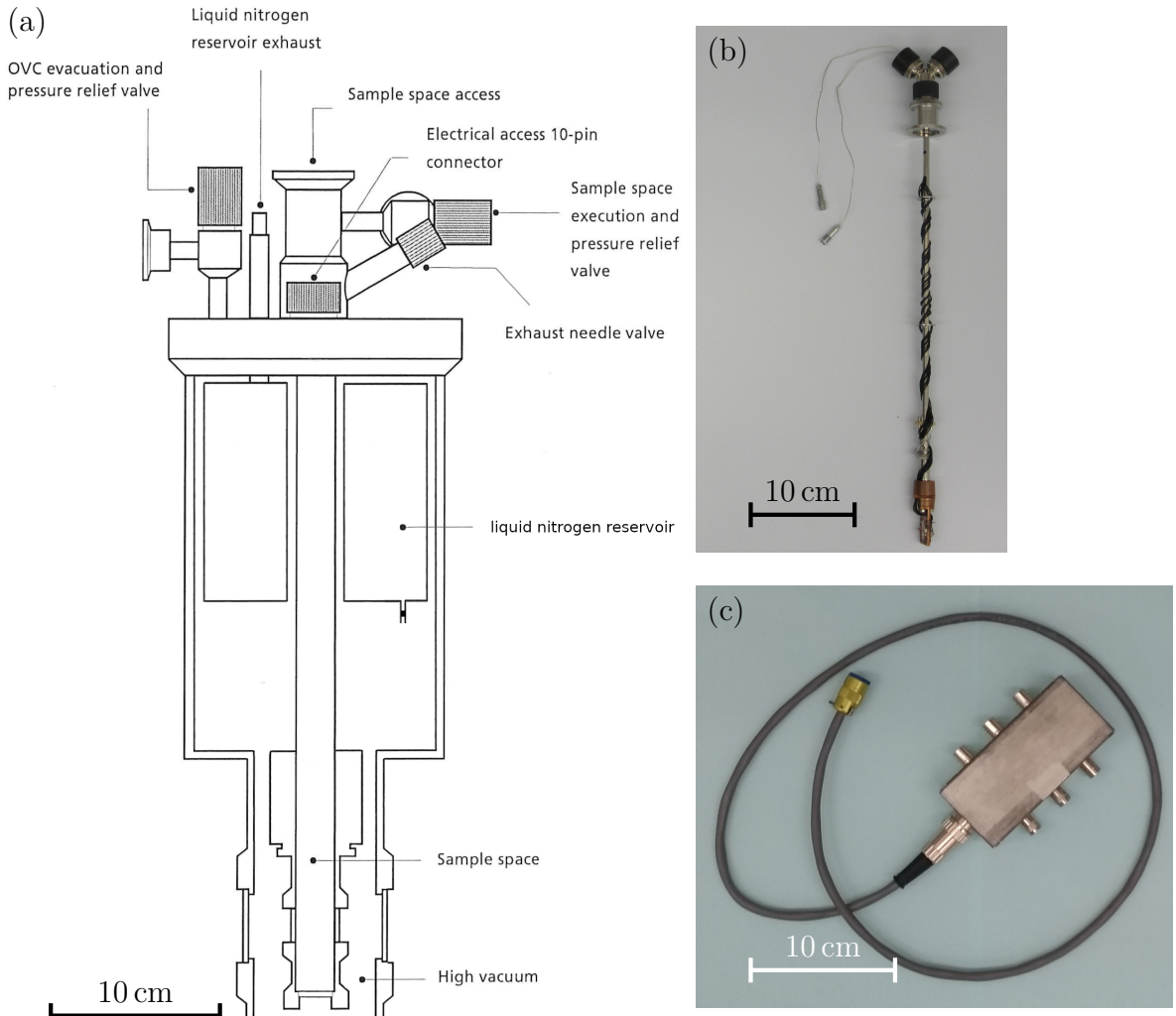

Figure 3.1: Experimental setup used for temperature-dependent dc conductivity investigations. **(a)** Cross section of the utilized *Oxford Instruments, Optistat DN* cryostat. Figure reprinted from ref. [52]. **(b)** Sample rod with fully shielded cables (gray, visible with their LEMO connectors outside the vacuum part) down to the probe head suitable for low-current measurements. The PT100 temperature sensor at the probe head is connected in four-wire arrangement via black cables wriggled around the sample rod. **(c)** New home-built access box, merging the connectors for the probe head PT100 temperature sensor and further cables to the probe head's (black cables in panel (b)). It gets connected to the cryostat via the golden plug to the electrical access 10-pin connector shown in panel (a).

Several technical improvements on the cryostat have been implemented within the project to ensure a fully shielded signal transmission and reduce electric noise. As the most important contribution, a new signal access module was built for the cryostat used here,

shown in fig. 3.1c, which combines access to additional signal cables on the sample rod as well as the wiring for the temperature sensor on the sample holder. Furthermore, fig. 3.1b depicts a photograph of the sample rod, which was upgraded by installing temperature resistant cables to realize future measurements with sample temperatures up to 500 K.
Compared to the previous experiments by Thiessen [16], the temperature setpoint was changed step-wise and the resistance measurements were performed only after reaching thermal equilibrium. While changing the temperature, both electrodes where short-circuited via the electrometer to allow equalization of pyroelectrically generated charges. The temperature fluctuations during the measurements were proven to be less than 0.01 K. Pyroelectric effects therefore can be neglected for all the temperature-dependent dc conductivity measurements conducted later.
During a full $I(U,T)$ measurement as it will be presented in sec. 4.3, a refill of the liquid nitrogen reservoir was required every 8 h, while the whole measurement took in total between 16 and 24 h. All instruments mentioned above were controlled during this time via a home-built framework-supported software written in *python3*. The software takes modern aspects of object-oriented software development [53, 54] into account, to ensure a modular and long-term stable operation.

3.2 Macroscopic dielectric spectroscopy

An overview of the different applied experimental setups to measure alternating currents is given. A detailed characterization of their performance is initiated that is continued in the appendices.

3.2.1 Experimental setup classes and common features

The most fundamental property while determining dielectric properties of a solid material is the electro-magnetic wave frequency f, which ranges from a few mHz up to 10^{15} Hz for optical electromagnetic waves, covering about 20 orders of magnitude. This huge range requires to split the measurements into different sections using several experimental techniques. A more detailed introduction to the technical realizations over the full frequency range is given by Krohns [47]. The following considerations in this section are limited to the frequency range accessible with common analog electronic circuits between 10^{-1} and 10^{6} Hz. This is also the frequency range where first simple ferroelectric nanoelectronic devices are expected to work.
One main challenge for all setups was to minimize electromagnetic noise caused by the environment of the setup. To this end, samples were mounted inside a home-built tinplate box equipped with four BNC connectors to enable four-wire configuration measurements. A noise level analysis was performed with different wiring schemes between the connector

shieldings and a soldered contact on the sample box. The minimum current noise level was reached for the case of the connector shieldings being connected to each other and connected with the sample box, so there is only one uniform ground potential and the resulting ground loop seems to be of minor influence (see also fig. 3.2 in the following section).

name	4284A	Alpha Analyzer	ZVL
manufacturer	*Hewlett Packard*	*Novocontrol*	*Rohde & Schwarz*
type	LCR-meter	impedance measurement system	vector network analyzer
frequency range	20 Hz - 1 MHz	3 µHz - 40 MHz	9 kHz - 3 GHz
amplitude range	5 mV - 20 V	100 µV - 3 V	−50 dBm - 0 dBm
offset voltage	±40 V	±40 V	0

Table 3.1: Parameters of commercial instruments for dielectric spectroscopy applied within this thesis. The parameter space of the used lock-in amplifiers is discussed in app. A.2.

Most commonly, dielectric spectroscopy is realized with commercial instruments designed for this application. Several devices have been used within this thesis and their parameter spaces are summarized in tab. 3.1. It has to be noted that this class of devices is restricted to first harmonic current measurements and can not detect higher-harmonic current contributions (HHCC) as this will be reported in sec. 4.4. During the measurements with the *HP 4284A* LCR-meter and the *Alpha Analyzer*, the samples were connected in full four-wire configuration via the above described box as this is common in LCR-measurements [47]. By principle, the measurements with the *Rohde & Schwarz ZVL* network analyzer were performed in a two-wire configuration. The frequency range of the *ZVL* turned out to be at too high frequencies for the investigated domain walls, so the instrument was only applied for the device comparison performed at a test circuit discussed in app. A.1.

A second type of realization is given by manually composing a measurement system out of a signal generator, a current-voltage (IV) converter and a lock-in amplifier (LIA). Three different LIAs were used for the setup characterization: *Stanford Research Systems SR830* and *SR860*, as well as *Zurich Instruments UHFLI*, respectively. Furthermore, a *Femto DLPCA-200* IV-converter, and an *Agilent 33250A* signal generator were involved in different combinations. The parameters of the mentioned components are discussed in app. A.2.

All experimental setups were designed to be fully remotely controllable via a main computer connected to the internet. This allowed flexible and fast-to-realize experimental procedures with standardized protocols. On the other hand, it minimized the actual work to be done in the laboratory, a significant advantage since the experimental period was

superimposed by different states of the COVID-19 pandemic with partially limited access to the labs [55].

3.2.2 Lock-in amplifier-based dielectric spectroscopy

The fundamental experimental setup for lock-in amplifier (LIA) based dielectric spectroscopy is shown in fig. 3.2. An active current-voltage (IV)-conversion is assumed for all following considerations and experiments. The sample was enclosed in a metal box as described in the previous section. All components were connected by BNC cables to ensure proper shielding. For simplicity, the reference potential was the same as the ground potential, and no increase of noise levels was observed due to this decision.

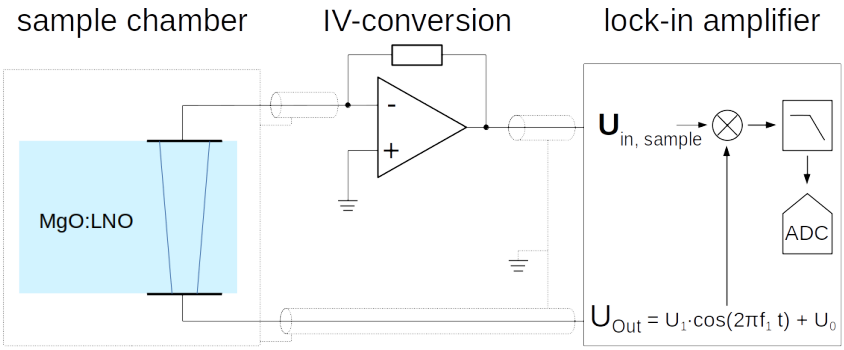

Figure 3.2: Fundamental experimental setup for lock-in amplifier-based dielectric spectroscopy. Instead of the internal signal generator implemented in modern LIAs, a separate external signal generator can be used. The requirements on the individual components are discussed in app. A.

After the in-depth characterization of the available devices, which is presented in app. A, two LIA-based experimental setups were assembled using devices summarized in tab. 3.2. As first setup, the *simple LIA-based dielectric spectroscopy setup* was arranged. Since the additional preamplifier is operated with a constant amplification of 10, all relevant parameters only need to be communicated from the main computer to a single device, the *Zurich Instruments UHFLI* lock-in amplifier. In addition, the phase synchronization between the internal signal generator and the LIA is automatically done internally. The main drawback is thereby the minimum frequency limit of about 1 kHz that follows from

name	simple LIA-based setup	broadband LIA-based setup
signal generator	*ZI UHFLI* LIA interal generator + *ITHACO 4302* (pre-)amplifier	*Agilent A33250A*
IV-converter	*Femto DLPCA-200*	*Femto DLPCA-200*
lock-in amplifier	*ZI UHFLI*	*SR 830*

Table 3.2: Experimental devices used in the LIA-based dielectric spectroscopy setups for the higher-harmonic current contribution measurements.

the setup characterization (app. A.2) for measurements with dc offset voltage. Therefore, a second experimental setup, the *broadband LIA-based setup* was composed with a lower frequency limit of 1 Hz. Thereby, the trigger output of the signal generator is used as the LIA reference signal and the main computer had to communicate with two instruments. Since the IV-converter and the LIA are within one device for the broadband LIA-based dielectric spectroscopy setup, the current noise limit is lower than for the simple LIA-based setup and in absolute numbers lower than 10^{-11} A.

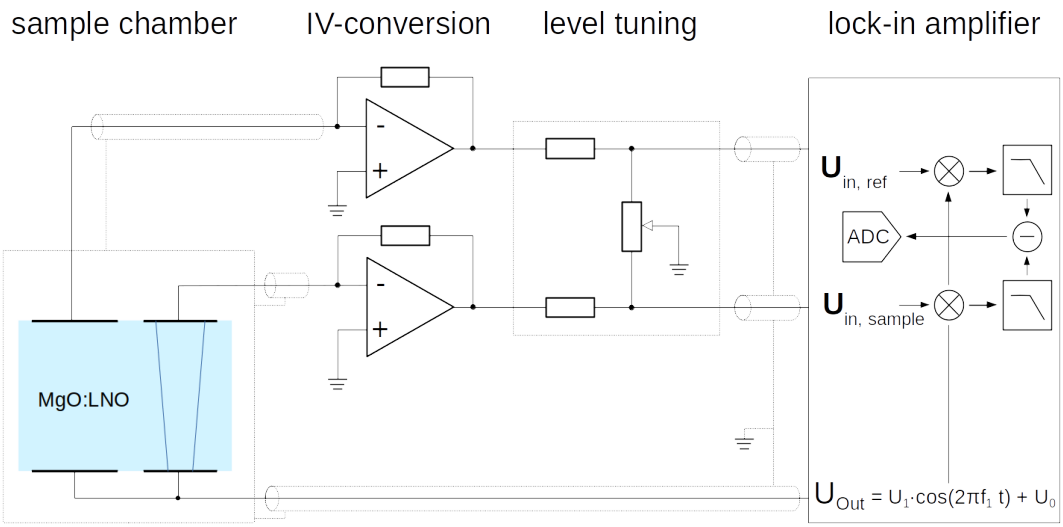

Figure 3.3: Principle setup for differential lock-in amplifier based dielectric spectroscopy, involving, compared to the basic setup in fig. 3.2, a second IV-converter and a level-tuning circuit to compensate the different sizes of the contact electrodes.

To distinguish the electronic properties of bulk material and domain walls more clearly, the two experimental setups were also operated in a differential version that is shown in fig. 3.3. Compared to the simple version of fig. 3.2, it contains a further current-voltage converter and a level-tuning circuit. The IV-conversion was realized by a second *Femto DLPCA 200* amplifier. Exchanging the two *Femto* devices revealed no significant change, so they were assumed to have equal properties. The home-built level-tuning circuit was placed in a further tinplate box. It was necessary to compensate for the different sizes of the involved electrode pairs, which were deposited with non-uniform shadow masks. By using a 25-turn precision potentiometer in the level-tuning circuit, the signals could be equalized down to 1 ‰. In practice, the level-tuning was accomplished by equalizing the first harmonic imaginary current components at low voltage amplitude and without constant offset voltage.

In addition to the characteristics of the experimental setup, the achievable precision in lock-in amplifier based dielectric spectroscopy measurements depends on the sample properties, first of all the order of magnitude of the absolute impedance value, which is directly related to the current amplitudes to be measured. Moreover, the precision depends also on

the ratio of resistance R and reactance X, which is defined by the impedance phase angle ϕ_Z. They are combined to the complex impedance $\mathbf{Z}$ by $\mathbf{Z} = R + \mathbf{i}X = |\mathbf{Z}| \exp(\mathbf{i}\ \phi_Z)$. Therefore, a subsequence goal was to characterize one LIA-based dielectric spectroscopy setup as a function of the (complex) sample impedance, which is described in detail in app. B.

4 Material-specific results and discussion

4.1 Samples and measurements during preparation

The preparatory procedures of domain poling and domain wall conductivity enhancement are introduced. Based on second harmonic generation microscopy, the domain wall geometry of the involved samples is presented.

Within the presented experiments, four different samples have been in focus. All of them were based on 5 mol-%-MgO doped $LiNbO_3$ single crystals in optical quality, sliced in 200 µm-thick wafers perpendicular to the crystallographic z-direction (z-cut) and $5 \times 6\,\mathrm{mm}^2$ size in x- and y-direction. Into each sample, a single domain was written by laser-enhanced poling using a liquid cell, explained in more detail by Haußmann [21]. This was followed by a conductivity enhancement procedure, described by Godau *et al.* [15].
Typical poling and conductivity enhancement results are shown in fig. 4.1. Domains were nucleated and grown within a liquid cell via a defined voltage pulse (a). Thereby, the positive pole (anode) is applied to the z+ side, while the negative pole (cathode) is applied to the z- side. This orientation is defined for the whole thesis as the forward or positive current direction. Depending on the poling pulse, the domain reaches a certain size, which can be determined in-situ via a polarization sensitive optical microscope (b). After evaporation of chromium electrodes of 10 nm thickness and approximately $1\,\mathrm{mm}^2$ lateral area on both sides, contacted with silver paste, a typically extremely low dc conductivity is observed, as shown in fig. 4.1c. The IV-curve is point-symmetric except of a positive current I_{offset} of about 0.10 pA, which is an artifact introduced by the electrometer. The current apart from the offset can be mainly attributed to the charging process of the plate capacitor, formed by the evaporated electrodes. Assuming a voltage sweep with constant ramp rate dU/dt, the charging current can be calculated by employing the well-known relations for the parallel plate capacitor's capacitance C:

$$C = \varepsilon_0 \varepsilon_r \frac{A}{d} = \frac{\partial Q}{\partial U} = \frac{dQ/dt}{dU/dt} = \frac{I_{charge}}{dU/dt}. \tag{4.1}$$

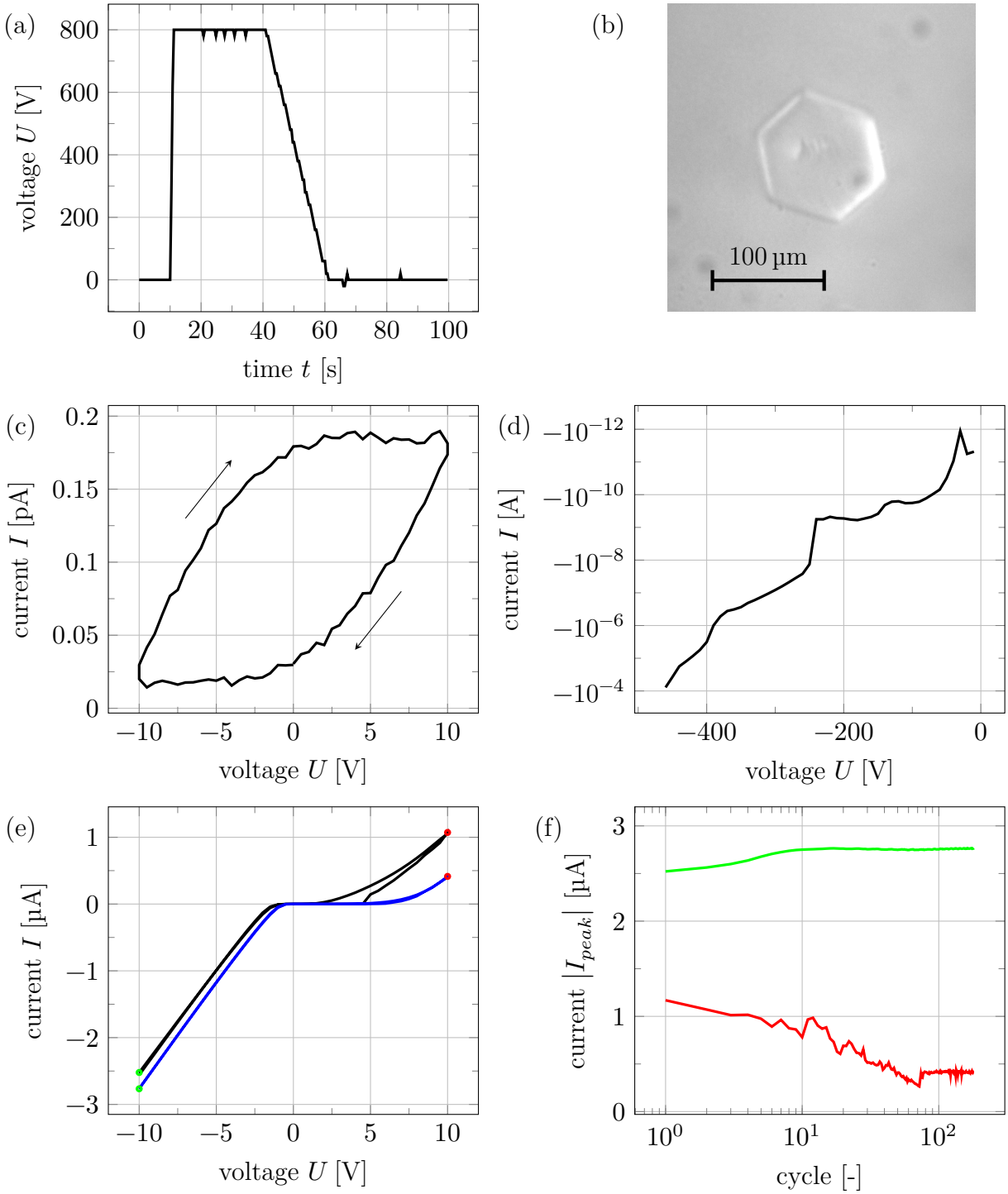

Figure 4.1: Poling and conductivity-enhancement of an exemplary LNO domain wall (sample *mz15*) according to the preparation procedure introduced by Godau *et al.* [15]: **(a)** A voltage pulse is applied to the liquid cell to nucleate a single domain. **(b)** The nucleated domain as imaged by the polarization sensitive optical microscope after poling. **(c)** IV-curve of the contacted domain wall before enhancement. The current amplifier within the electrometer introduces a constant offset I_{offset} shifting the absolute values. **(d)** Application of a large voltage opposite to the poling direction to enhance the domain wall conductivity. **(e)** IV-curves of the domain wall directly after the enhancement procedure (black) and 8.2 h later (blue). **(f)** "Peak currents" of every measured IV-curve cycle (indicated in (e) as ▫, ▫) during the relaxation. The totally covered time is 8.2 h.

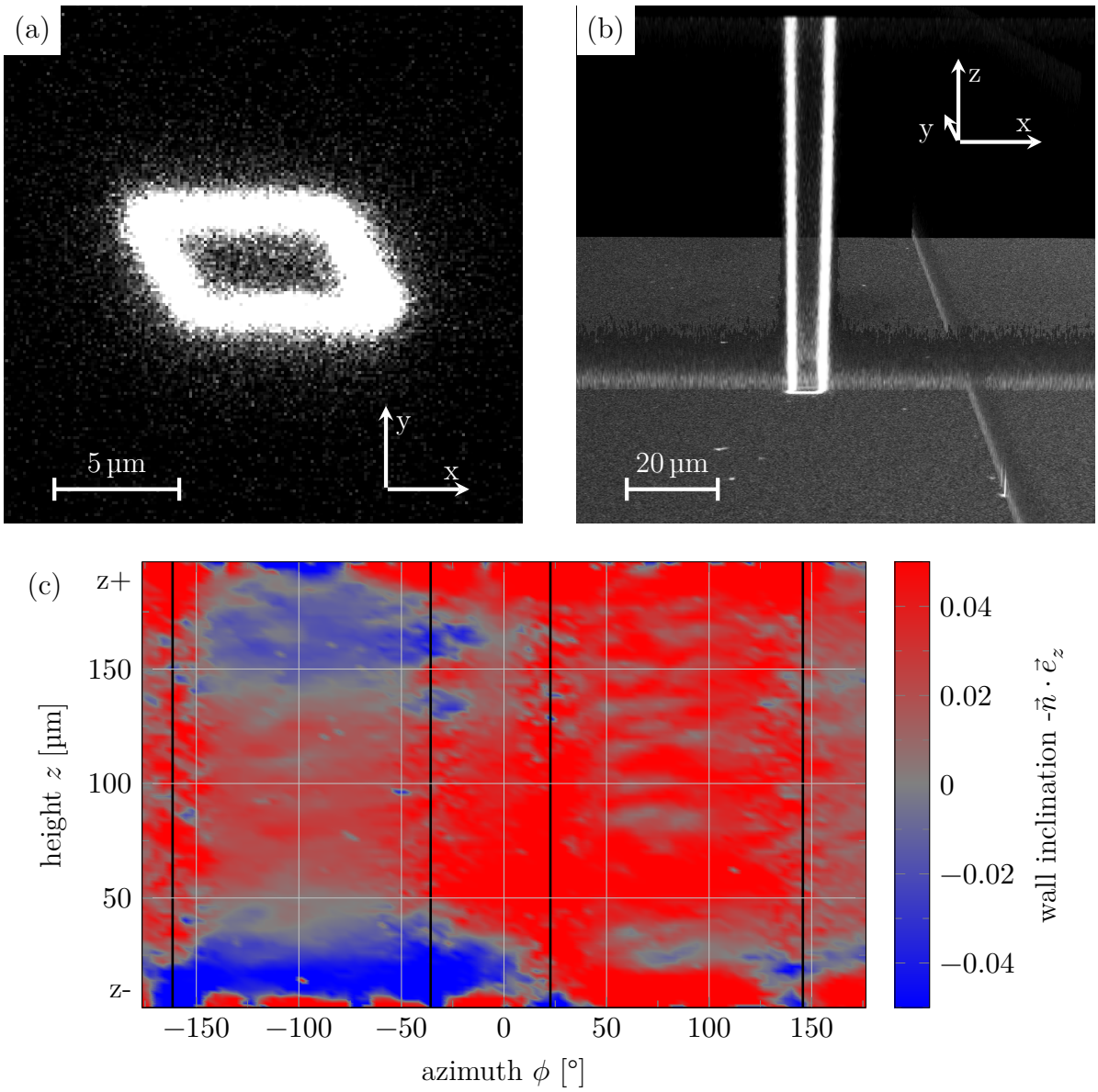

Figure 4.2: Domain geometry in sample *sl02* after conductivity enhancement, measured with second harmonic generation microscopy. **(a)** Cross section in the xy-plane at 100 µm depth. The length in x-direction is 4.0 µm and 7.5 µm in y-direction. **(b)** Slice in xz-plane, revealing the slightly tilted domain walls. On the right bottom part, a truncated dust particle is visible as an example, which generates second harmonic signal contrast only close to the surface and can be clearly distinguished from a ferroelectric domain. **(c)** Domain wall inclination angle map in cylinder coordinates, extracted from the 3D SHG data. Head-to-head domain walls appear in red color, while blue corresponds to tail-to-tail walls. $\phi = 0$ coincides with the positive x-axis in panel (a). The black lines indicate the corner positions.

By inserting typical values of $\varepsilon_r = 33$ [45], $A = 1\,\mathrm{mm}^2$, $d = 200\,\mu\mathrm{m}$, and $dU/dt = 0.25\,\mathrm{V/s}$, a charging current $I_{charge} = 0.365\,\mathrm{pA}$ can be calculated, which is even larger than the observed currents around I_{offset}. This is reasonable, since the voltage sweep is

practically done in steps of 0.1 V and the charging current decays between the voltage change and the current measurement.
In a next step, a negative voltage ramp with approximately 3 V/s ramp rate is applied to permanently enhance the domain wall conductivity by increasing the domain wall inclination relative to the crystallographic z-axis, shown in fig. 4.1d. Then, a dc conductivity two to five orders of magnitude larger can be measured (e). After the enhancement procedure, the dc conductivity curve relaxes over several hours into its final shape by domain wall stabilization (f).
The first two samples *sl01* and *sl02* that are investigated her were prepared by Ahmed Samir Lofty, and their room temperature dc conductivity was analyzed within his Master's thesis [31]. They correspond to sample 1 and 2 in chapter 4.2 of ref. [31] where the temporal stability of domain wall conductivity in LNO is discussed. According to the classification of domain wall stability levels, introduced in ref. [31], the two samples belong to the "category A", having long-term stable, highly conductive ferroelectric domain walls.
The final domain wall geometry was investigated via second harmonic generation microscopy (SHG), which is described in more detail by Kämpfe *et al.* [56]. As illustration, the domain wall geometry of sample *sl02* is shown in fig. 4.2. In contradiction to the typical hexagonal domain shape in LNO, the domain has a parallelogram-like shape in the xy-plane. This may arise whenever one pair of sides in the hexagon is much smaller than the remaining two, being in this case condensed in the top left and bottom right corner. With a maximum orthogonal distance between parallel opposite sides of 7.5 µm, the domain is relatively small. In fig. 4.2b, the wall inclination with respect to the z-axis with the normal vectors pointing towards the z- side (see also fig. 1.1b) is visible, indicating a head-to-head wall characteristic. This is further specified by the domain wall inclination map, shown in fig. 4.2c. It reveals also parts with negative inclination angle, but they do not form a continuous current path. According to the experimental results by Xiao *et al.* [26], it can be assumed that the observed electrical conductivity is fully carried by electrons.
The other two samples under considerations, *mz13c* and *mz15*, were freshly prepared for this project. They exhibited a stable domain wall conductivity over several months, so they belong to category A as well. For sample *mz15*, a hexagonal domain with an orthogonal edge distance of 110 µm was observed, shown in fig. 4.1b.
A completely different domain structure was found in sample *mz13c*. Due to multiple application of high voltages in forward and backward direction as outlined for the conductivity enhancement procedure, a huge number of domains was generated covering around 90 % of the effective chromium electrode size of 1.58 mm^2 as described by Kirbus *et al.* [57]. The corresponding SHG microscope image is shown in fig. 4.3. As there

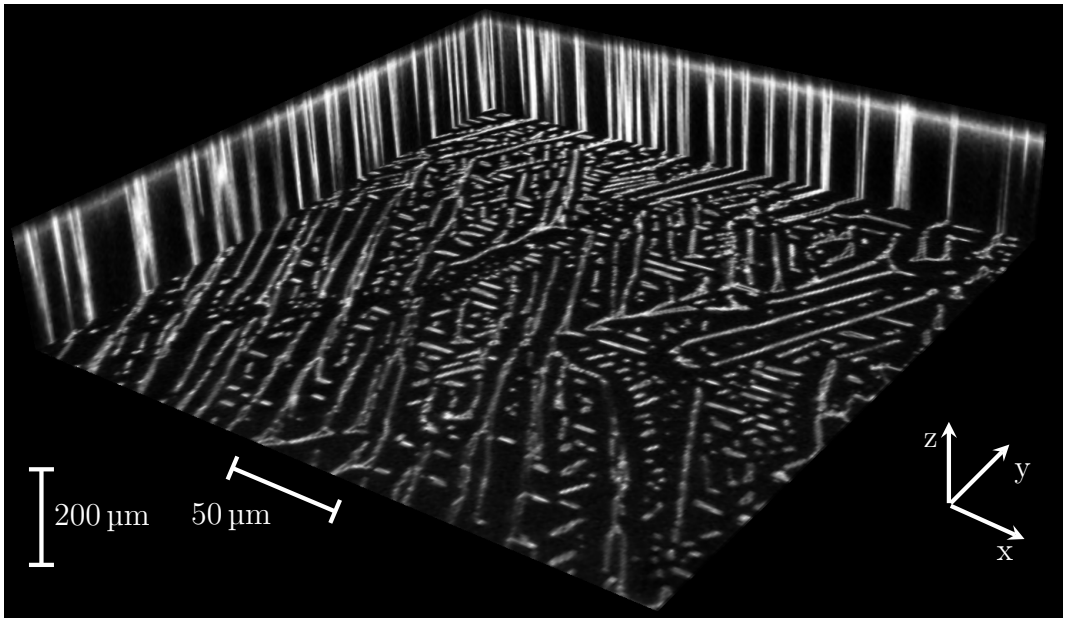

Figure 4.3: Orthogonal slices of the domain wall structure in sample *mz13c* after conductivity enhancement investigated with second harmonic generation microscopy. During the enhancement procedure, a transition towards many small domains as discussed by Kirbus *et al.* [57] occurred. The tilted scale bar defines the length scale in x- and y-direction, while in z-direction the full crystal thickness of 200 µm is shown.

are many thoroughly penetrating domains, it is not easily possible to determine the contributing current paths. Nevertheless, the domain configuration exhibits an interesting dc characteristic curve and was therefore suitable for some fundamental measurements concerning higher-harmonic current generation.

A further phenomenon has been found within the samples *mz13c* and *mz15*, in connection with the experiments on higher-harmonic current generation on LNO domain walls as presented later in sec. 4.4. During those measurements, ac electric voltages of the order of several volts and frequencies up to 100 kHz were applied to the samples for a longer time period (in case of the so-called frequency-offset map shown later on in fig. 4.17 for nearly 14 h). After this procedure, a huge number of small spike domains could be observed outside the area that was contacted on both sides by the chromium electrodes, as depicted in fig. 4.4. This effect is unexpected, since the applied fields are orders of magnitude lower than the coercive field, which corresponds, in this geometry, to an applied voltage of 1.52 kV [21]. Therefore the relation of high frequency electric fields and domain nucleation in bulk material should be further investigated in the future, taking advantage from existing experiences in thin film LNO poling [58].

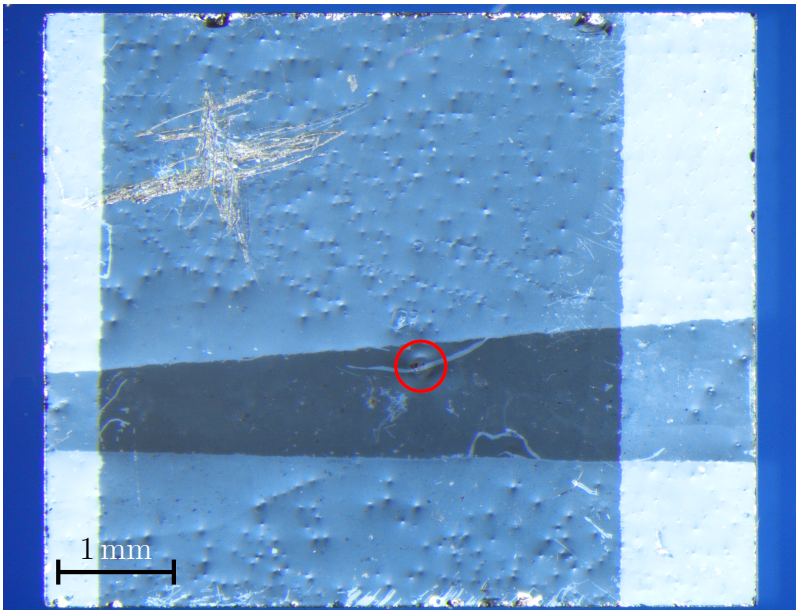

Figure 4.4: Polarization sensitive microscopy image of sample *mz15* after multi-day measurements with the broadband lock-in amplifier-based dielectric spectroscopy setup. A huge number of spike domains are seen to nucleate outside the area of interest that is formed by the stripe-like top and the rectangular-shaped bottom electrode. The red circle indicates the actually investigated domain within the electric measurements. The scratch in the top electrode emerged while removing the silver paste after the electric measurements.

4.2 Room temperature dc conductance

The room temperature dc conductance curves are fitted to the proposed equivalent circuit model. Intrinsic parameters of the domain walls such as the effective donor density are extracted from the fit parameters.

After their stabilization, the domain walls exhibited non-ohmic IV-curves, which remained stable over several months. According to the equivalent circuit model, the observed conductance is determined by (a) the intrinsic domain wall conduction and (b) the Schottky injection barrier between domain wall and the contact metal electrodes. Consequently, the IV-curves were modeled by the equivalent circuit as shown in fig. 4.5.

The IV-curves for all investigated samples are shown in fig. 4.6. For all samples, a diode-like characteristic is observed at lower voltages and an ohmic-like characteristic for higher voltages each in forward and backward direction. Due to different weighting of those two parts, a crossing of the IV-curves for different samples at $U \neq 0$ is not excluded and is actually observed.

The model consists of six parameters, the resistance R, the saturation current I_s, and the characteristic voltage U_c, each in forward (positive) and in backward (negative) direction. Since the characteristic IV-curves were defined by more than 40 points, the agreement of

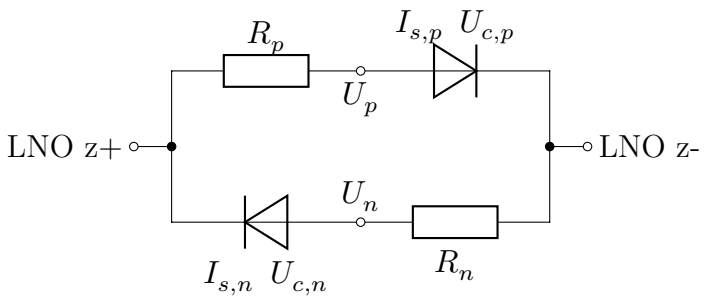

Figure 4.5: Equivalent circuit used to model the observed room temperature IV-curves. The resistors represent the intrinsic domain wall conductivity, while diodes stand for the the Schottky barriers between LNO domain wall and the evaporated chromium contact electrode, respectively. Relevant parameters of the involved circuit elements are the resistance R, the saturation current I_s, and the characteristic diode voltage U_c, each in positive (forward) and negative (backward) direction.

model and experimental data is by far not granted. Before applying the fitting routine, parameters were manually adjusted using a small graphical user interface close to their final values, to ensure convergence. To take account for the wide potential range of the model parameters, the decadic logarithm of the parameters values was optimized instead of the parameter's themselves. The optimization was performed with a trust region reflective algorithm [59] with least-squares cost function, implemented in the *python3* library *scipy* [60].

Since diodes are nonlinear circuit elements, the current through the equivalent circuit can not be expressed in a closed form expression for a fixed voltage. It was therefore necessary to determine the potentials U_p and U_n by applying Kirchhoff's current law [61] on these knots and calculate the current in the two paths via Ohm's law for the resistors. The potentials are given as follows, where the terms inside the absolute value function $(I_{diode} - I_{resistor})$ become zero for the optimally chosen U:

$$\begin{aligned} U_p &= \underset{U\in(U_{z-},U_{z+})}{\arg\min} \left| \underbrace{I_{s,p}\left[\exp\left(\frac{U-U_{z-}}{U_{c,p}}\right)-1\right]}_{I_{diode,p}} - \underbrace{\frac{U_{z+}-U}{R_p}}_{I_{resistor,p}} \right| \\ U_n &= \underset{U\in(U_{z-},U_{z+})}{\arg\min} \left| \underbrace{I_{s,n}\left[\exp\left(\frac{U-U_{z+}}{U_{c,n}}\right)-1\right]}_{I_{diode,n}} - \underbrace{\frac{U_{z-}-U}{R_n}}_{I_{resistor,n}} \right|. \end{aligned} \tag{4.2}$$

The parameter optimization was accomplished for all four samples involved. The results are summarized in tab. 4.1. According to their coefficient of determination R^2, all curves fit well to the proposed model, which is visually confirmed, e.g., in fig. 1.1a. Several parameters are of the same order of magnitude for all samples, with the exception of sample *mz13c* that exhibited a different domain structure as described in sec. 4.1. This

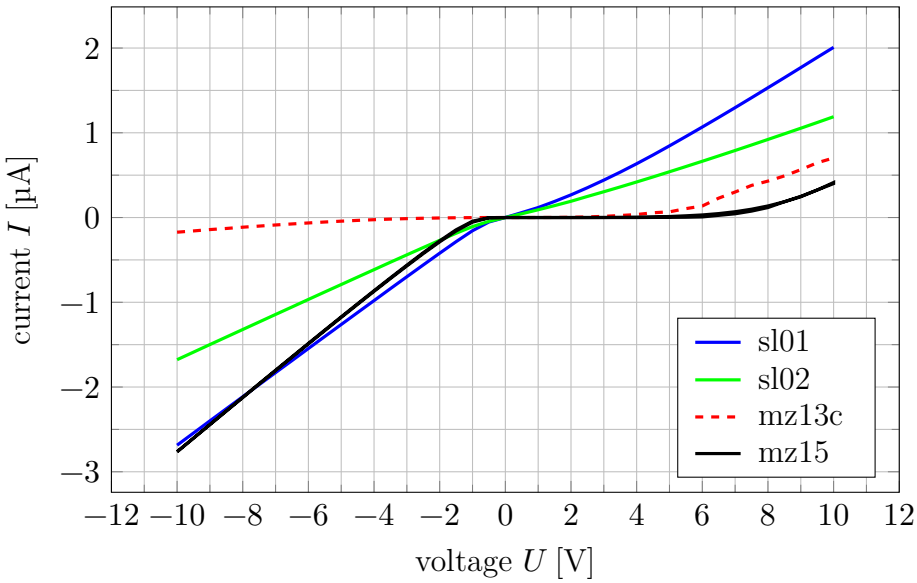

Figure 4.6: Room temperature IV-curves of all investigated samples after domain wall relaxation. For sample *mz13c*, the current is visualized ten times larger then actually measured. The voltage was changed step-wise with $\Delta U = 0.5\,\mathrm{V}$, $\Delta t = 2\,\mathrm{s}$. Positive and negative branch were measured separately with $\operatorname{sgn}\frac{dU}{dt} = \operatorname{sgn} U$.

holds especially for the serial resistance and the characteristic voltage in forward as well as in backward direction. The narrow variation ranges indicate nanoscopic similarities of the involved current paths.

First, the forward and backward series resistances R_p and R_n are observed to be on the order of several MΩ. Despite their similar values, it is not easily possible to relate the series resistance to a single domain wall property, since many parameters influence the resistance. As discussed in sec. 2.1, this includes most importantly the inclination angle with respect to the z-axis, but also the wall thickness and the domain diameter. Furthermore, all included quantities are not constant over the full domain wall sheet (fig. 4.2c).

Second, the saturation currents I_s, which are influenced by the properties of the Schottky barrier, its height, width, and cross section perpendicular to the current flow, exhibit a wide spreading over four orders of magnitude, indicating significant differences on the current injection from the metal into the domain wall. Conductive atomic force microscopy (cAFM) measurements by Godau *et al.* [15] have proven that the current injection is not homogeneous over the full hexagon, allowing for large-scale variations of the effective current path cross section. Since the overall cross section of the domain walls is small compared to industrially available diodes, it is plausible that all measured saturation currents are lower than typical values of industrially available diodes, which are of the order of 50 µA. Nevertheless, samples *sl01* and *sl02* demonstrate in forward direction the large range of possible domain wall conductivity tuning.

sample	R_p [MΩ]	$I_{s,p}$ [pA]	U_p [V]
mz13c	54.03 ± 0.11	21.56 ± 0.10	0.7565 ± 0.0005
mz15	2.838 ± 0.005	12.8 ± 0.7	0.857 ± 0.004
sl01	3.68 ± 0.12	$(1.23 \pm 0.34) \cdot 10^5$	0.91 ± 0.16
sl02	7.156 ± 0.034	$(9.83 \pm 0.14) \cdot 10^4$	0.601 ± 0.005

sample	R_n [MΩ]	$I_{s,n}$ [pA]	U_n [V]	R^2
mz13c	271.4 ± 0.4	113.5 ± 0.7	1.0560 ± 0.0010	0.926
mz15	$3.069\,87 \pm 0.000\,38$	211.4 ± 2.0	$0.163\,37 \pm 0.000\,20$	0.951
sl01	3.437 ± 0.008	430 ± 290	0.136 ± 0.022	0.990
sl02	5.511 ± 0.010	100 ± 90	0.134 ± 0.012	0.980

Table 4.1: Parameters obtained by fitting the room temperature IV-curves (fig. 4.6) of the LNO samples to the equivalent circuit model shown in fig. 4.5. Due to the complexity of the model an implicit fitting involving equ. 4.2 was required. R^2 represents the coefficient of determination.

Third, the characteristic voltage U_c is the most interesting quantity regarding the physical interpretation. As discussed in sec. 2.3, U_c is related to the thermal voltage U_T by $U_c = nU_T = nk_BT/q$. Since k_BT/q is approximately 25 mV at room temperature, the measured values correspond to a large ideality factor $n \gg 1$. As discussed in sec. 2.3, this phenomenon can be observed in metal-semiconductor junctions for the case of larger doping levels and current transport via field emission. Here, it corresponds to a large number of free charge carriers within the domain wall.

According to equation 2.6, the ideality factor can be used to estimate an effective doping concentration N_d. In forward direction, the mean characteristic voltage of the three single domain samples $\overline{U_c} = 0.79\,\mathrm{V}$ corresponds to $n = 31$ and $\frac{N_d}{m_r\varepsilon_r} = 4.6 \cdot 10^{19}/\mathrm{cm}^3$. In backward direction, $\overline{U_c} = 144\,\mathrm{mV}$, following $n = 5.7$ and $\frac{N_d}{m_r\varepsilon_r} = 1.5 \cdot 10^{18}/\mathrm{cm}^3$ is calculated. Furthermore, the relative effective mass and relative permittivity are given by $m_r = m^\star/m_0 = 0.05$ [25] and $\varepsilon_r = 33$ [45], so $m_r\varepsilon_r \approx 1.7$ and the given values directly indicate the order of magnitude of the effective donor density N_d itself.

Theoretical calculations of Eliseev *et al.* [25] using a Landau-Ginzburg-Devonshire approach, estimated an electron density of 10^{20} to $10^{21}/\mathrm{cm}^3$ at the center of the domain wall and an exponential decrease apart from that. This is compatible with the experimental results, since the metal-domain wall Schottky barrier is an average over the full domain width. Since the characteristic voltages in forward and backward direction differ significantly by a factor of 5.5, the geometric asymmetry between the z+ and z- side is clearly observable in this room temperature dc conductance, while the reasons for this observation are an open question.

4.3 Temperature-dependent dc conductance

The dc IV-characteristics were investigated for two samples as a function of the temperature. A simple thermally-activated hopping transport is observed for larger voltages, and additional effects occur at low voltages due to the Schottky-like conductivity. The results are compared with measurements under the same conditions on an industrial Schottky diode.

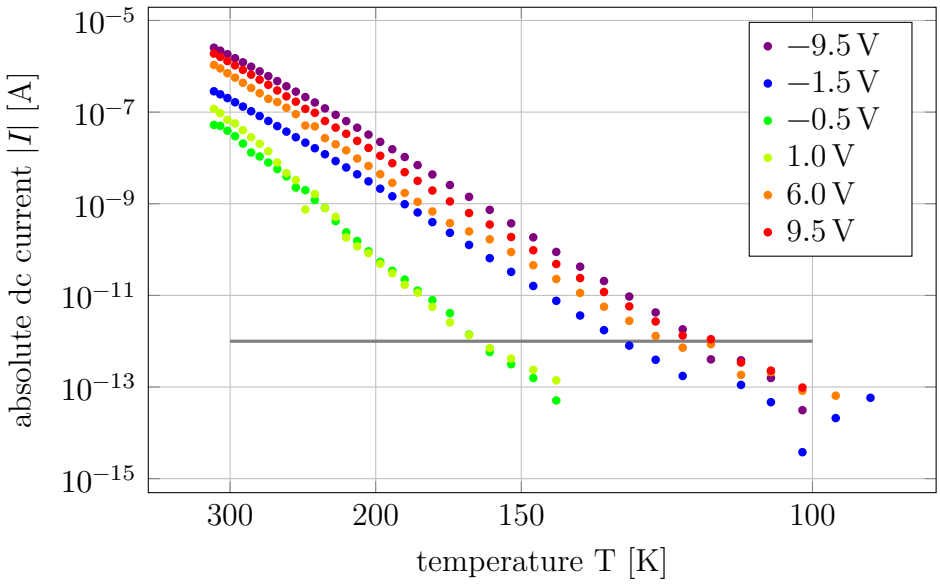

Figure 4.7: Temperature-dependent dc current of the macroscopically contacted domain wall in sample *sl01* for different voltages U applied to the outer electrodes. The experimental procedure is described in sec. 3.1. For the further analysis, only data points with absolute current values above a 10^{-12} A threshold were considered (above gray line).

As described in sec. 3.1, the dc conductance of the conductivity-enhanced LNO domain walls was investigated as a function of voltage and temperature in samples *sl01* and *sl02*. The raw data – electric current as a function of voltage and temperature – are shown in fig. 4.7. Data points were acquired for 40 different temperature logerithmically distributed between 92 and 320 K, while for each temperature an IV-curve was acquired between ± 10 V in steps of $\Delta U = 0.5$ V with $dU/dt = 0.5$ V/s. The data points are plotted as $(\log_{10} I)(1/T)$, also known as Arrhenius plot. In this representation, the I(T)-dependence is transformed into a straight line for the case of simple thermally-activated hopping (equ. 2.1, $\beta = 1, \alpha = 0$).

Figure 4.7 reveals a clear hopping transport behavior as observed in previous experiments [16]. The current increases strongly with temperature, and the activation energy E_a is nearly constant over the full temperature range between 100 K and 320 K. This is different to the results on as-grown domains by Thiessen [16], who observed only piece-wise constant activation energies and several orders of magnitude lower currents due

the supposedly less inclined domain walls. The domain wall conductivity enhancement procedure is therefore a more efficient method to increase the domain wall conductivity as compared to the super-bandgap illumination studied in the same thesis, which drastically changed the conductance-temperature dependence, then even exhibiting a local current maximum between 200 and 300 K. A smooth conductance-temperature dependency is important in terms of constructing nanoelectronic devices, as the temperature needs to be compensated in most cases by further circuitry.

As the I(T)-dependence was recorded for different voltages, the activation energy can be investigated as a function of the dc voltage. Since this evaluation technique is not widely established and has not been found in detail in literature, the temperature-dependent dc conductance of an industrial Schottky diode was measured as well between 175 K and 290 K under the same conditions as a reference test. More specifically, a metal-to-silicon diode of type *BAT 48* manufactured by *STMicroelectronics* in a cylindrical SMD version (SOD-80 package) was used.

The activation energy as a function of the dc voltage U is shown for that reference diode in fig. 4.8. In contrast to the discussed theories, a discontinuity is observed at $U = 0$. According to the derivation in equ. 2.8, the increase of the activation energy E_a for low electric fields can be modeled by:

$$E_a(U) = E_0 - A \cdot \frac{U/U_c}{1 - \exp(-U/U_c)}. \tag{4.3}$$

Here, E_0 is a constant offset, A a scaling factor and U_c represents the characteristic voltage, which is the most relevant quantity for this investigation. Despite the observed discontinuity, the model could be applied to the reference diode as shown in fig. 4.8. The largest differences between the measured data and the adapted curve are observed close to the discontinuity. This is not unexpected, since the model in equ. 4.3 constitutes a low order approximation of the real phenomenon.

Together with the results of the LNO samples, the fit parameters are summarized in tab. 4.2. According to the derivation of the fit equation (equ. 4.3), $E_0 = (621 \pm 4)$ meV is

sample	*BAT 48*	*sl01* forward	*sl01* backward	*sl02* forward	*sl02* backward
E_0 [meV]	621 ± 4	222.5 ± 1.5	199.24 ± 0.09	257.8 ± 1.3	253 ± 17
$-A$ [meV]	-11 ± 28	97.5 ± 2.8	19.3 ± 1.2	132 ± 5	38 ± 66
U_c [10^{-1} V]	0.231 ± 0.004	14.6 ± 0.9	9.5 ± 0.5	13.4 ± 0.9	0.4 ± 1.0
R^2 [-]	0.985	0.994	0.990	0.991	0.993

Table 4.2: Fit parameters of voltage dependent activation energy $E_a(U)$ according to equ. 4.3. For the fitting of of the forward branches, the substitution $U \to -U$ was applied. The red lines in fig. 4.9 represent further the voltage range used for each of the fits.

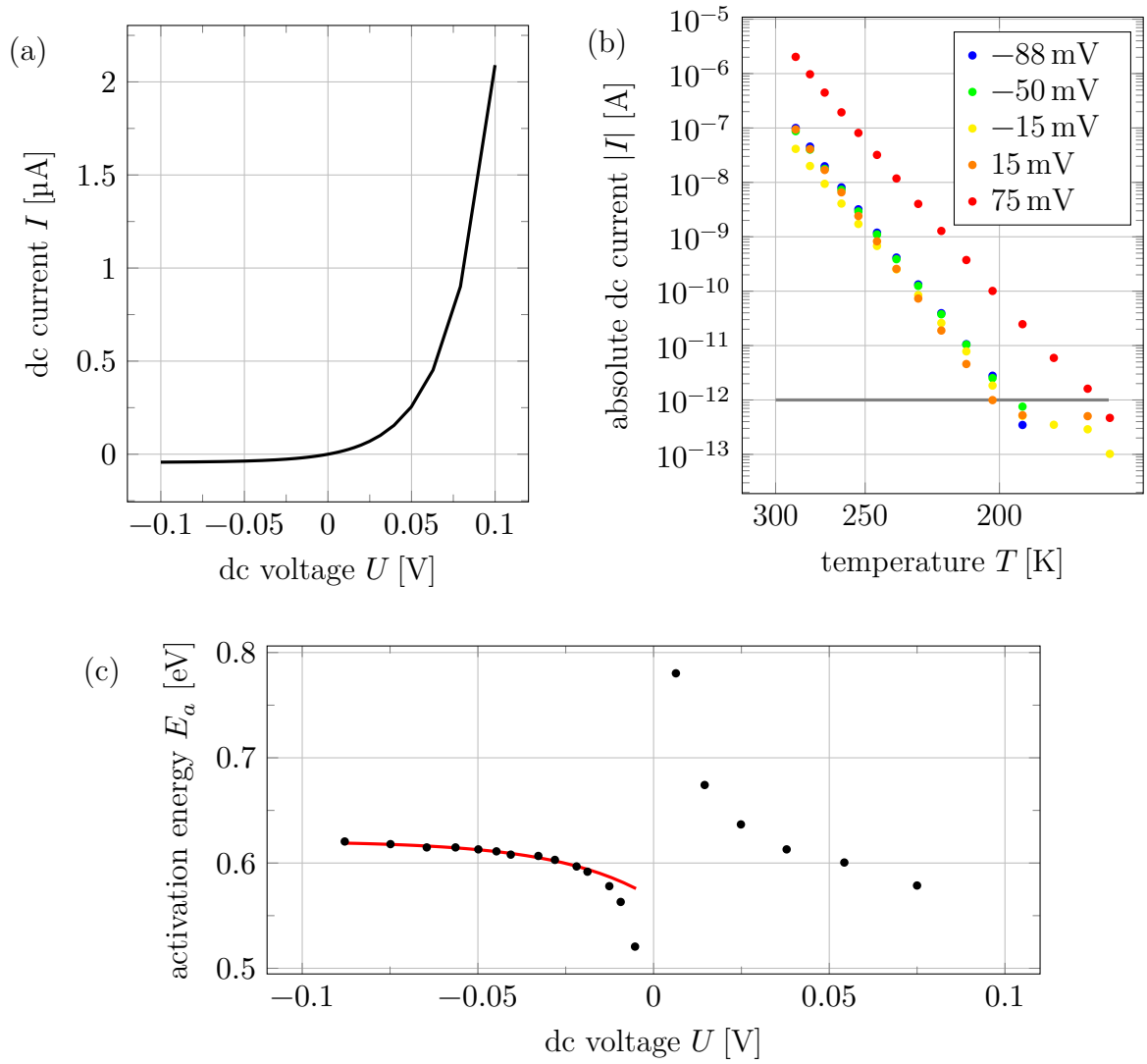

Figure 4.8: Temperature-dependent dc conductance of an industrial *BAT 48* Schottky diode. **(a)** IV-characteristic at room temperature, $T = 287\,\mathrm{K}$. **(b)** Current versus temperature for different voltages in Arrhenius configuration, exhibiting a good agreement with the Shockley equation (equ. 2.3). **(c)** Activation energy E_a as a function of the dc voltage, exhibiting a discontinuity around $U = 0$.

an approximation of the Schottky barrier height for the reference diode and lies within the expected range. By using the results of Grundmann [62], it indicates a low work function of the applied (and so far unknown) metal, which forms together with the silicon substrate the Schottky contact. By assuming a typical ideality factor of $n = 1.1$, the observed characteristic voltage $U_c = nk_BT/q = (23.1 \pm 0.4)\,\mathrm{meV}$ corresponds to a temperature of $(244 \pm 4)\,\mathrm{K} = (-29 \pm 4)\,^\circ\mathrm{C}$, which is well inside the range of applied temperatures and therefore a reasonable value. Furthermore, it is remarkable that the estimated uncertainties of the parameter A, which have no physical meaning so far, exceed in some cases the determined parameter value. Since the measurements are well described by the

resulting fit, the uncertainties seem to be overestimated or they indicate a correlation of these parameters.

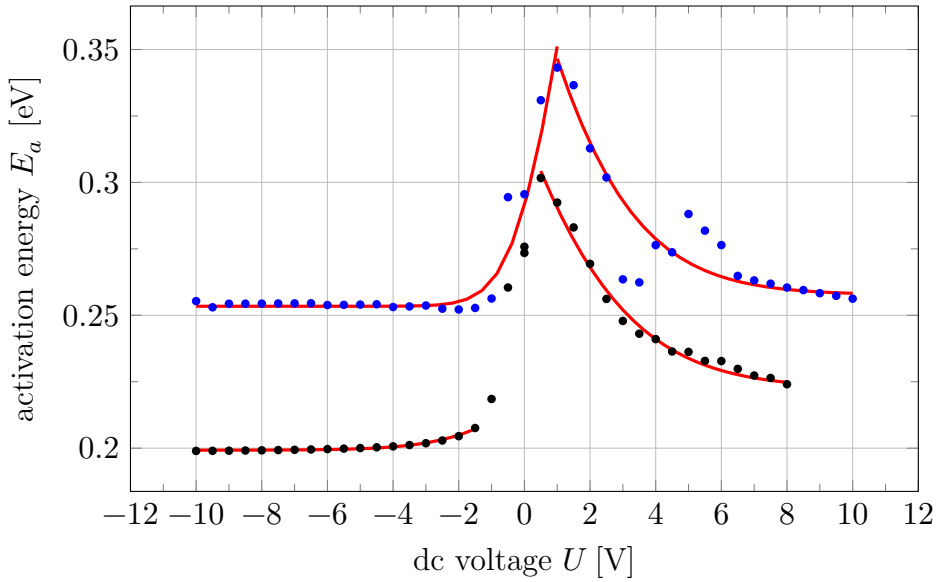

Figure 4.9: Activation energy E_a of the domain wall samples *sl01* (black) and *sl02* (blue) according to equ. 2.1 as a function of the dc voltage, assuming $\beta = 1$ and $\alpha = 0$. Red lines represent the fits according to equ. 4.3.

After having investigated the reference diode, the results on the LNO walls shown in fig. 4.9 can be interpreted as follows. Both samples exhibit a constant activation energy in case of $U < -5\,\mathrm{V}$ and tend towards a constant value for $U \gg 5$. According to the equivalent circuit model (fig. 4.5), the constant activation energy between 0.2 and 0.25 eV is connected to the intrinsic conductivity of the domain wall, while the peak around $U = 0$ is related to the metal-LNO interface Schottky barrier. It is therefore mandatory to analyze the two regimes separately.

At low electric fields, a positive peak of the activation energy is observed for both samples (fig. 4.9). According to the discussion in sec. 2.3, this is the expected result within the model proposed by Tietze *et al.* [44]. Furthermore, the width of the peak should be positively correlated to the characteristic voltage U_c. This explains nicely the asymmetry of the peak on a qualitative level, since the characteristic voltage in forward direction (right side of the peak) is, according to the room temperature IV-curves, significantly larger then in backward direction (left side).

The fit parameters for the LNO domain walls reveal significantly increased values for the characteristic voltage on the domain wall-metal junction as compared to the thermal voltage U_T. This is similar to the observations on the room temperature dc conductance in sec. 4.2, despite the fact that the absolute values in forward direction are even larger than observed at room temperature. In backward direction, the data point step size of 0.5 V is relatively large when compared to U and especially U_c, so the parameters

could be roughly estimated only. Since the extraction of U_c from the voltage-dependent activation energy characteristics is an unconventional evaluation method, it is likely that the results obtained by this technique are further distorted by so far unspecified effects, causing an apparent increase of the characteristic voltage.

The second quantity of interest is the constant activation energy E_0 at larger voltages U, building the bridge towards the intrinsic conductivity of the domain wall. Both observed values are within the range of previous experimental results between 150 meV and 250 meV [16]. Nevertheless, a remarkable offset in the activation energy is observed between the the two samples. This is a hint to nanoscopic differences, most probably introduced during the manual poling procedure, which may be reduced by a fully automatized poling procedure, which is under construction so far.

The mentioned range of activation energies covers the expected energies of free electron polarons, which are therefore supposed to be the major origin of conductivity within the LNO domain walls. According to Faust *et al.* [23], electron polarons are also responsible for the weak LNO bulk conductivity. Bulk and domain wall conductivity therefore probably only differ in their order of magnitude in the charge density.

To give further grounds and inputs to the hypothesis that in fact electron polarons are responsible for the LNO domain wall conductivity, single $I(T)$ curves at constant voltage were investigated with respect to their compatibility to equ. 2.1. Since the parameters α and β are, in practice, highly correlated, it was not possible to fit both parameters simultaneously. Therefore, one parameter was fixed to a common value mentioned in sec. 2.2, while the other parameter was fitted.

parameter	unit	$\alpha = 0$	$\alpha = 1$	$\alpha = 3/2$	$\beta = 1$	$\beta = 1/2$	$\beta = 1/4$
α	-	0	1	1.5	2.17	18.29	50.54
$\Delta\alpha$	-	-	-	-	0.17	0.12	0.16
β	-	1.147	1.072	1.038	1	0.5	0.25
$\Delta\beta$	-	0.015	0.013	0,012	-	-	-
T_0	K	808	1020	1149	1332	$151.3 \cdot 10^3$	$305.8 \cdot 10^8$
ΔT_0	K	25	32	36	14	$1.1 \cdot 10^3$	$3.2 \cdot 10^8$
$k_B T_0$	eV	0.0696	0.08786	0.099	0.1148	13.03	$2.6 \cdot 10^6$
$\tilde{I}_0$	$\mathrm{A} \cdot \mathrm{K}^\alpha$	0.00233	2.73	98	$11.6 \cdot 10^3$	$1.00 \cdot 10^{62}$	$8.12 \cdot 10^{219}$
$\Delta\tilde{I}_0$	$\mathrm{A} \cdot \mathrm{K}^\alpha$	0.00016	0.20	7	$5.5 \cdot 10^3$	$3.71 \cdot 10^{61}$	$5.44 \cdot 10^{219}$
R^2	-	0.999	0.999	0.999	0.999	0.999	0.999

Table 4.3: Parameters of $I(T)$-curve fitting for sample *sl01* with $U = 10\,\mathrm{V}$ according to equ. 2.1. The fixed values of α and β represent different models for the intrinsic conductivity of an LNO domain wall.

The fit parameters are listed in tab. 4.3. All curves represent the measured data according to their coefficient of determination R^2 nearly perfect, so a deeper analysis of the different curves is required. It further proves the high correlation of α and β that prevents the

distinction of their influences.
As most obvious observation, the cases of fixed β with $\beta = \frac{1}{2}$ and $\beta = \frac{1}{4}$ can be rejected, since the values of α and T_0 are orders of magnitudes away from all predictions of any model discussed in literature. In addition, all approaches with fixed α converged with β being close to one, despite their estimated uncertainties on β are most probably underestimated. Thermally activated hopping with $\beta = 1$ is therefore the most likely conductivity mechanism explaining the observed domain wall conductivities. It indicates an equal energy of the polaron hopping sites, while there is no conclusion about their real space distribution. No indications are found for variable-range hopping as introduced by Mott [36] or Efros and Shklovskii [37].
After having determined the larger conduction mechanism group, the determination of α would allow for a detailed distinction of the different mechanisms. This is prevented by the fact, that β influences the conductivity σ exponentially, while α interferes quite weakly via a power law dependence, only. Consequently, all curve fittings with fixed α converge and exhibit $\beta \approx 1$. In case of the expected value for small free polarons $\alpha = \frac{3}{2}$, β converges indeed with the smallest difference to 1.0 among all fixed-α fits, but it can not be proven as being statistically evident.

4.4 Higher-harmonic current generation

The non-ohmic domain wall conductivity, which originates from the metal-semiconductor junction, is analyzed based on the generation of higher-harmonic current contributions in low-frequency alternating-current (ac) electric fields. As the junction is expected to be of Schottky-type, the observed characteristics are compared to the higher-harmonic current contributions of an industrial Schottky diode.

The generation of higher-harmonic current contributions (HHCCs) in low-frequency electric fields by diodes was investigated on a fundamental level by Gambhir *et al.* [63]. Despite they investigated a pn-junction in an industrial silicon diode, the results are valid for metal-semiconductor junctions analogously, too. Since within this project the current contributions shall be investigated quantitatively, the properties of the HHCCs - especially their amplitude and phase - needed to be derived theoretically first, which is shown in detail in app. C. The final result, given in equ. C.18, predicts the HHCCs of a Schottky diode based on its intrinsic properties, the saturation current I_s, the characteristic voltage U_c, the amplitude of the alternating electric field U_1, and also optionally a constant offset voltage U_0:

$$|\mathbf{I}_m| = I_s \cdot \mathrm{I}_m \left(\frac{U_1}{U_c}\right) \exp\left(\frac{U_0}{U_c}\right), \tag{4.4}$$

with I_m being the modified Bessel function of first kind and of mth order.
All measurements of amplitude and offset dependencies of the following sections were performed with the simple differential lock-in amplifier (LIA)-based dielectric spectroscopy setup (sec. 3.2.2). Thereby a unified procedure was performed to take data points measuring HHCCs: Before starting each measurement, differential compensation was performed by adjusting the potentiometer (sec. 3.2.2), and the transimpedance was chosen according to the expected current amplitude. If not mentioned otherwise, it was adjusted to 10^6 V/A. For each data point, firstly the parameters for the signal generator and LIA were automatically set by the computer, including frequency f, amplitude U_1, offset voltage U_0, time constant τ, sensitivity, and input coupling type. Then, a pause of 5τ was introduced to enable a stabilization of the output signals. Real- and imaginary part of the current were then measured 8 times with a delay of 0.5τ between two data points. The mean value of these raw data points was chosen as the "measured" data point and the standard deviation as the statistical error that will be shown in all diagrams later on.

4.4.1 Reference Schottky diode

As already practiced within the temperature-dependent dc conductivity measurements (sec. 4.3), a *BAT 48* Schottky diode was employed as a reference device. The excitation-amplitude dependency of the HHCCs for that device is now shown in fig. 4.10 and reveals a good agreement between the experimental data and the predicted modified Bessel function dependencies. As discussed in app. B, the setup can indeed detect HHCCs down to three orders of magnitude below the first-harmonic contribution, defining a *relative* resolution limit. In addition, a constant noise limit of 10^{-10} A is observed, most probably due to the finite time constant and limited IV-conversion precision within the lock-in amplifier, defining an *absolute* resolution limit. By fitting the modified Bessel function dependency to all components $m = 1$ to $m = 8$ at once, the fit lines in fig. 4.10 are determined and the characteristic parameters of the diode are extracted to be $I_s = (1.3 \pm 0.6) \cdot 10^{-7}$ A and $U_c = nU_T = (25.5 \pm 3.8)$ mV . As predicted by equ. C.10b, the phase angles start at 0 rad for the first order, and are separated with respect to each other by $\pi/2$ in anti-clockwise direction.
A similarly satisfying agreement is found for the offset voltage dependency, shown in fig. 4.11. The curves are well-described by exponential functions, as it is predicted by equ. 4.4. At least, the first three components run very parallel to each other, corresponding to very similar $U_c = nU_T = (26.24 \pm 0.02)$ meV. By taking into account the room temperature of 293 K, this value corresponds to an ideality factor of $n = 1.04$, which is well within the expected range. For the fourth harmonic order $m = 4$, the slope deviates significantly from that of the first three harmonic orders. A possible explanation is the low absolute current value, falling for negative offset voltages below the absolute

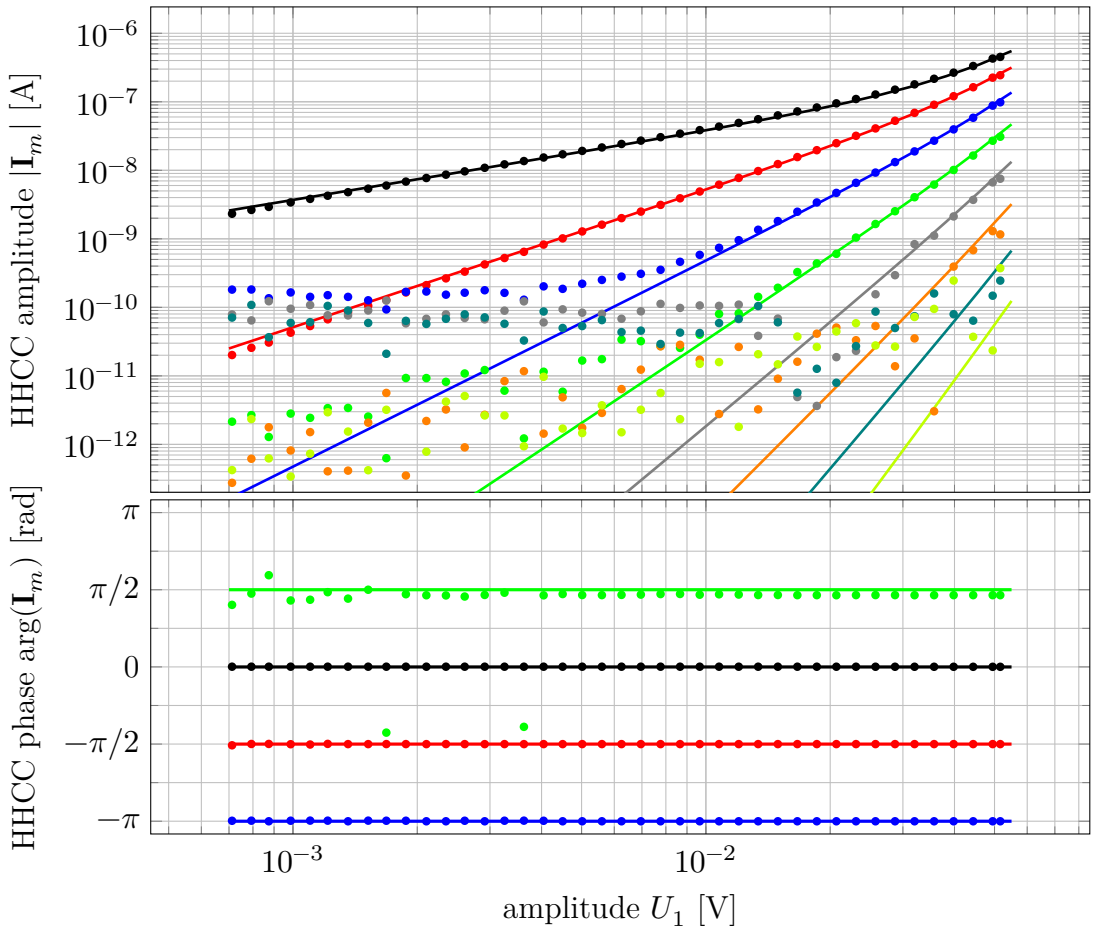

Figure 4.10: Bode plot of the excitation-amplitude dependency of the HHCCs of an industrial Schottky diode (*BAT 48*) at $f_1 = 86\,\mathrm{Hz}$ and $U_0 = 0$. The first eight harmonic orders are shown with their amplitude (upper panel) and the first four harmonic orders with their phase angles (lower panel). The theoretical predictions (solid lines) are fits according to equ. 4.4. For this and all following diagrams on HHCCs, a unified color mapping is applied:
$m = 1$: —, $m = 2$: —, $m = 3$: —, $m = 4$: —,
$m = 5$: —, $m = 6$: —, $m = 7$: —, $m = 8$: —.

resolution limit. In conclusion, both experiments carried out on the reference diode showed a very good agreement with the calculations in app. C and proved the capabilities of the assembled experimental setup for HHCCs measurements in general.

4.4.2 Multi domain wall structure

After these reference measurements, the HHCCs were analyzed on the samples *mz13c* and *mz15*, exhibiting a completely different behavior. This can be addressed to the different dc characteristic curves, discussed in sec. 4.1. Especially due to the high series resistance R_n in negative direction in sample *mz13c*, the nonlinear contributions are expected to be dominated by the forward-diode behavior. It was therefore convenient to compare the

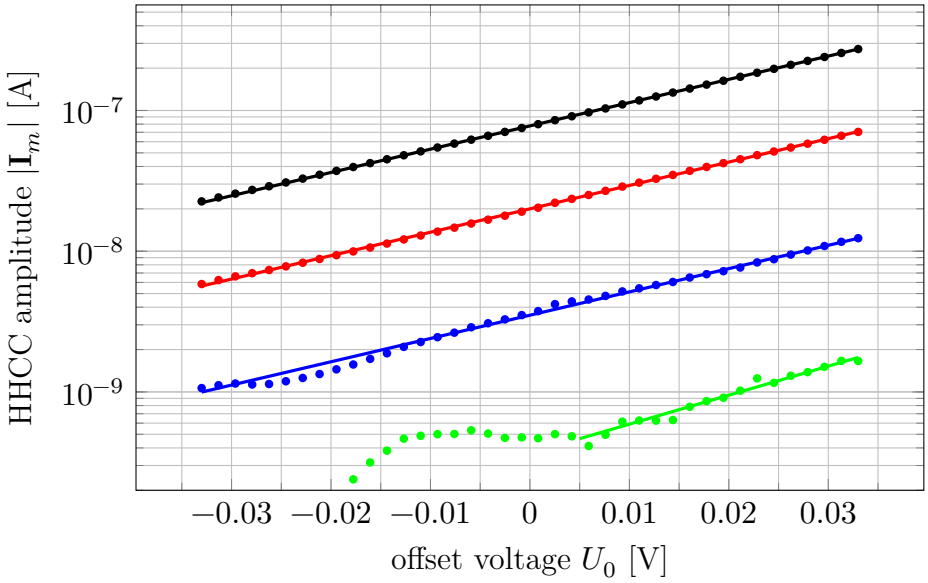

Figure 4.11: Absolute values of the first four HHCCs of a *BAT 48* Schottky diode as a function of the offset U_0, measured at an excitation voltage with $f_1 = 270\,\mathrm{Hz}$ and $U_1 = 20\,\mathrm{mV}$. The solid lines are exponential fits according to equ. 4.4.

results with the expectations for a single Schottky diode. This is different to sample *mz15*, where both diodes contributed by same order of magnitude, and therefore a more complex characteristic was observed that will be discussed later. For HHCC measurements on LNO domain walls, the setup was used in the differential version, with a second pair of electrodes evaporated onto the single domain bulk material as reference.

Starting with the easier case of sample *mz13c*, the amplitude dependence of the HHCCs is shown in fig. 4.12. Four harmonic orders were detected, as long as they were above the absolute resolution limit of the current measurement setup. To increase the amplitudes of the harmonic orders, a positive constant offset voltage was applied. According to equation 4.4, an additional offset voltage only increases the saturation current I_s by a factor of $\exp(U_0/U_c)$ without influencing the characteristic voltage $U_c = nU_T$. When fitting the first three orders simultaneously according to equation 4.4, the best parameter set is $I_s \exp(U_0/U_c) = (2.37 \pm 0.17) \cdot 10^{-7}\,\mathrm{A}$ and $U_c = (nU_T) = (3.61 \pm 1.60)\,\mathrm{V}$. In mathematical terms this is a fit of a function of two variables, since each measurement point is a triple of a harmonic order m, an offset voltage U_0, and an the absolute current measured for those parameter values. The corresponding curves of an ideal Schottky diode are plotted into fig. 4.12 as solid lines as well.

Both the saturation current and the characteristic voltage are much larger than observed in previous experiments discussed in sec. 4.2. As the large uncertainty and the imperfect fits suggest, the quantitative values are of low confidence. Nevertheless, the measured datapoints agree on a qualitative level with the single Schottky diode model. The phase

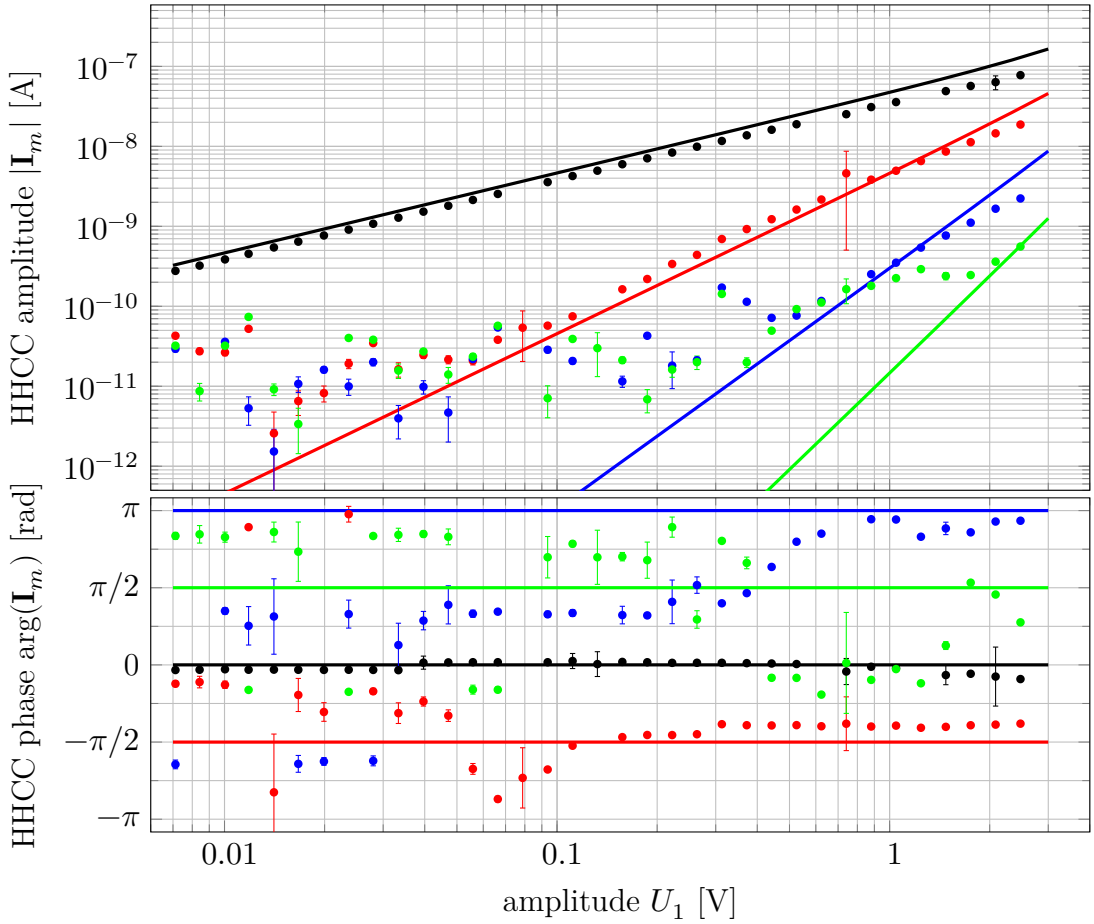

Figure 4.12: Amplitude dependence of HHCCs of the LNO domain walls in sample *mz13c* for $f_1 = 2\,\mathrm{kHz}$ and $U_0 = 6\,\mathrm{V}$. Stable amplitudes and phase angles are obtained for the first four harmonic orders. By fitting the first three orders according to equ. 4.4, the solid lines were obtained as best approximation to the Schottky diode model with $I_s \exp(U_0/U_c) = (2.37 \pm 0.17) \cdot 10^{-7}\,\mathrm{A}$ and $U_c = (nU_T) = (3.61 \pm 1.60)\,\mathrm{V}$.

angles fulfill their theoretical relation of anti-clockwise rotation according to equ. C.10b with minor deviations, as long as their amplitude is detectable. As a further observation, the first three harmonics are smaller than expected in case of $U_1 > 1\,\mathrm{V}$. A possible reason is the stronger influence of the series resistance, which will be discussed in more detail based on the offset-voltage dependence below.

The HHCCs of sample *mz13c* are shown in fig. 4.13 in dependence on the offset voltage U_0. As expected from the fit of the dc characteristics in tab. 4.1, the response is dominated by the forward diode. This manifests in an exponential increase of first, second and third harmonic amplitude around $U_0 = 0$. Further agreement is observed for positive offset voltages, where the phase angles nearly fulfill the theoretical prediction. Due to the influence of the series resistance, the fundamental frequency contribution is expected to reach a constant amplitude in case of larger voltages U_0, while all higher-harmonics are expected to exhibit a local maximum and decrease in amplitude for larger voltages due to

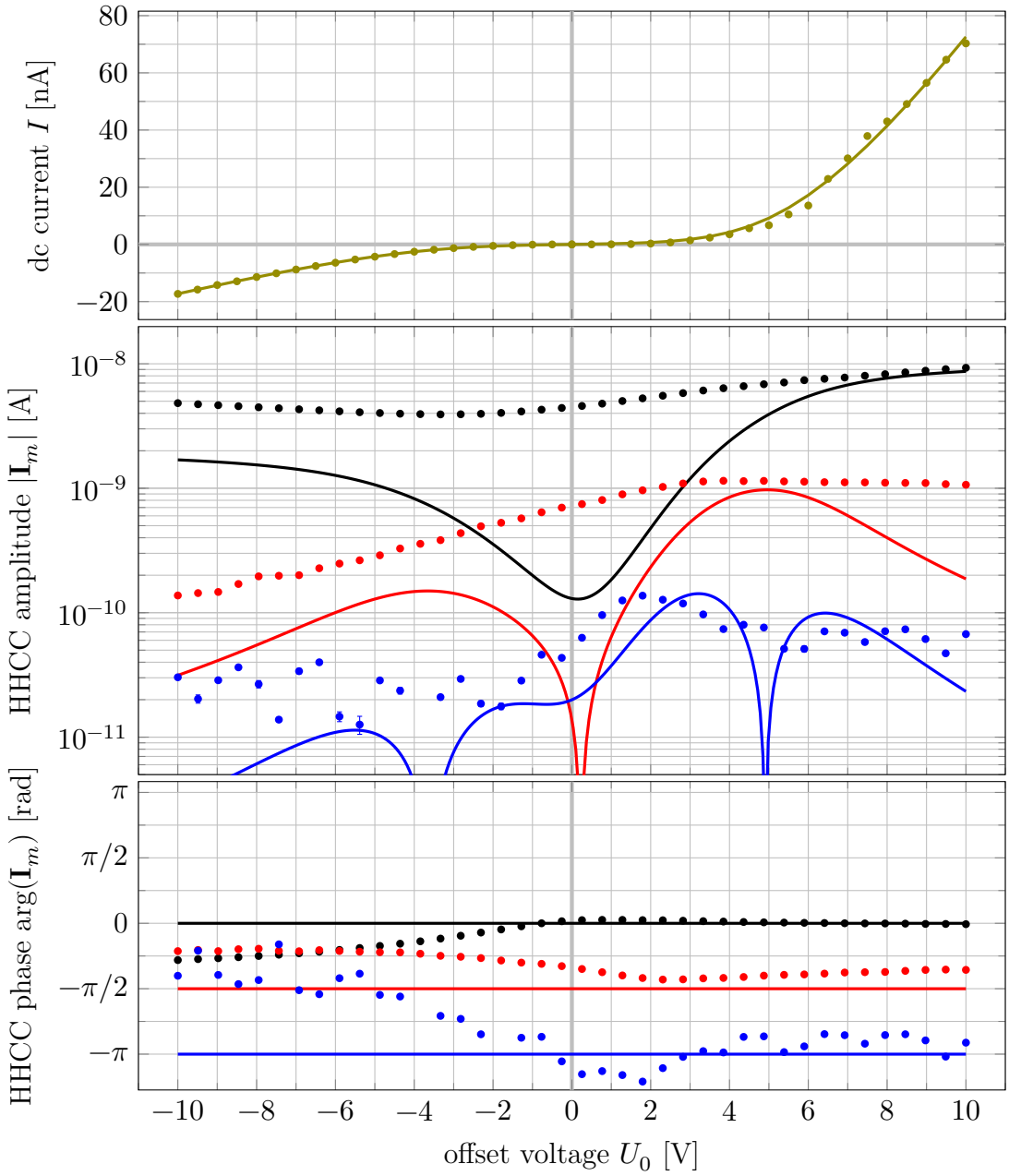

Figure 4.13: HHCCs of sample *mz13c* with respect to the offset voltage U_0 with $U_1 = 1.6\,\mathrm{V}$ and $f_1 = 2\,\mathrm{kHz}$. Upper panel: Replication of the dc characteristic curve and the fit according to the equivalent circuit model (sec. 4.2) with a dominant nonlinear contribution in forward direction. Middle and lower panel: Amplitude and phase of the first, second, and third HHCC. The solid lines represent the numerically calculated predictions (equ. C.4) based on the fitted dc characteristic curve shown in the upper panel.

the mostly linear IV-curve. These expectations are fulfilled for the first three harmonics at least on a qualitative level.

By using the fit parameters of the dc characteristic curve (fig. 4.13, top panel), the expected harmonic contributions can be calculated by numerical solution of the relevant

integrals in equation C.4 with the more complex characteristic curve of the equivalent circuit model. The results are visualized in fig. 4.13, middle panel, by the solid lines. As a general observation, the first and second harmonic contribution exhibit smaller slopes and consequently smaller absolute variations in amplitude than expected. This can probably be addressed to the chosen frequency, where conductivity is still observed but the low-frequency approximation is not fulfilled. The deviations are especially significant for negative offset voltages, where the first and second harmonic response change their phase angle by about 50° (fig. 4.13, bottom panel), while the third harmonic is below the absolute noise limit. Also the root of the second order contribution around $U_0 = 0$ which appears in the logarithmic scaling as a singularity, is not obtained within the measured data.

4.4.3 Single domain wall structure

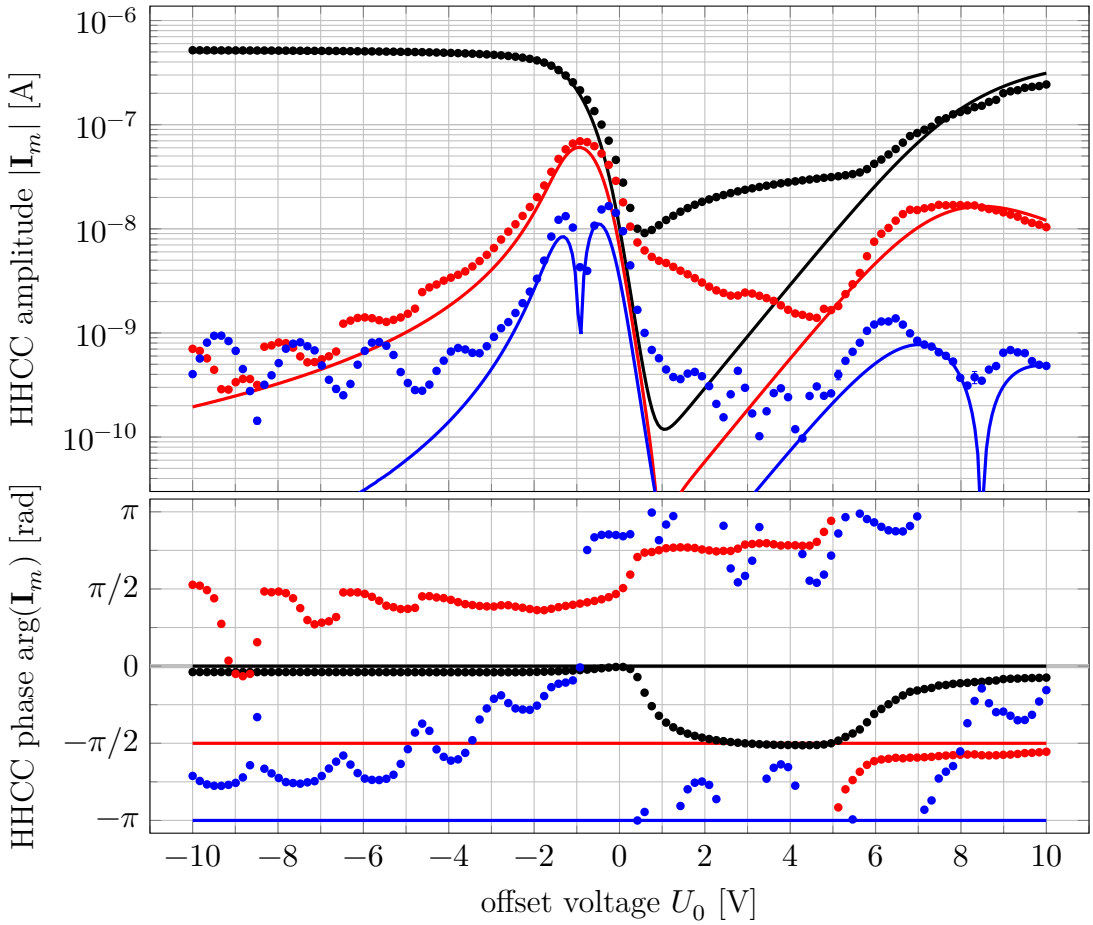

Figure 4.14: Higher-harmonic current generation on sample *mz15* with respect to the offset voltage U_0. The solid lines in the amplitude panel represent the expected values obtained from the fitted dc characteristic (tab. 4.1). $f_1 = 1.5\,\mathrm{kHz}$, $U_1 = 0.71\,\mathrm{V}$, $A_T = 10^5\,\mathrm{V/A}$.

In contrast to sample *mz13c*, nonlinear contributions were observed in the forward and

the backward current path in sample *mz15*. Since only one electrode was deposited on the top and the bottom side of this sample, respectively, a second piece of LNO from exactly the same wafer with evaporated electrodes was used as the differential reference. The full-range offset dependence is shown in fig. 4.14. In contrast to sample *mz13c*, all theoretically expected features concerning roots and local maxima are observed experimentally. This exemplary result is supported by the clear separation of the positive and negative side features, which is caused by the significantly different characteristic voltages in forward and backward direction: $U_{c,p} \gg U_{c,n}$ (tab. 4.1). As already observed in fig. 4.13, in regions of small expected signals, e.g. for $U_0 = 2\,\mathrm{V}$ to $6\,\mathrm{V}$, the current contribution amplitudes remain larger than expected, and stay above the absolute noise limit. Instead, continuous curves with orders of magnitude larger amplitudes are observed, which is probably caused by imperfect differential compensation. This means that the observed signal would originate from the reference pair of electrodes, which is supported by significant phase changes occurring in these regions.

The pronounced nonlinear dc characteristic curve (fig. 4.6) of the backwards oriented diode around $U_0 = -1\,\mathrm{V}$ motivates a more detailed analysis of this region. An enlargement of fig. 4.14 for the range $U_0 = 3\,\mathrm{V}$ to $1\,\mathrm{V}$ is shown in fig. 4.15. For the first three harmonic orders, the curves are equal to fig. 4.14. In addition to the first three orders, the fourth to sixth harmonic orders were measurable within this region. The amplitude curves correctly reproduce the expected local maxima and roots. A detailed derivation of the theoretical background is given in app. C. The roots are observed due to negative coefficients a_k that would occur in equ. C.9 when evaluating the equivalent circuit model analytically, which was realized numerically instead. In contrast to real-valued functions, the increasing number of roots with increasing harmonic order is expected. Thereby, each root of the amplitude should be connected with a phase shift of π (180°), which is clearly observed for all harmonic orders.

Despite the increased number of features, the phases still should fulfill their characteristic relation predicted in equ. C.9, with the exception of phase jumps of π. The validity of this relation (in this case with clockwise rotation) can be seen best at $U_0 = 0$, where the first, second, and sixth order fulfill this relation closely, while the remaining orders are less than 45° shifted off their ideal values. As expected, all roots observed in the amplitude plot are accompanied by a π phase shift in agreement with theory. The phase relations can be seen very well in the Nyquist diagram of this limited offset voltage range, shown in fig. 4.16. The phase shift differences between the harmonic orders are thereby encoded in the observation that the local maxima (end points of the long diagonal of every parallelogram-like curve) are alternatingly located in the bottom left and top right corner for the even orders (—, —, —) and in the top left and bottom right corner for the odd orders (—, —, —). Due to the logarithmic scale, the curves do not pass the

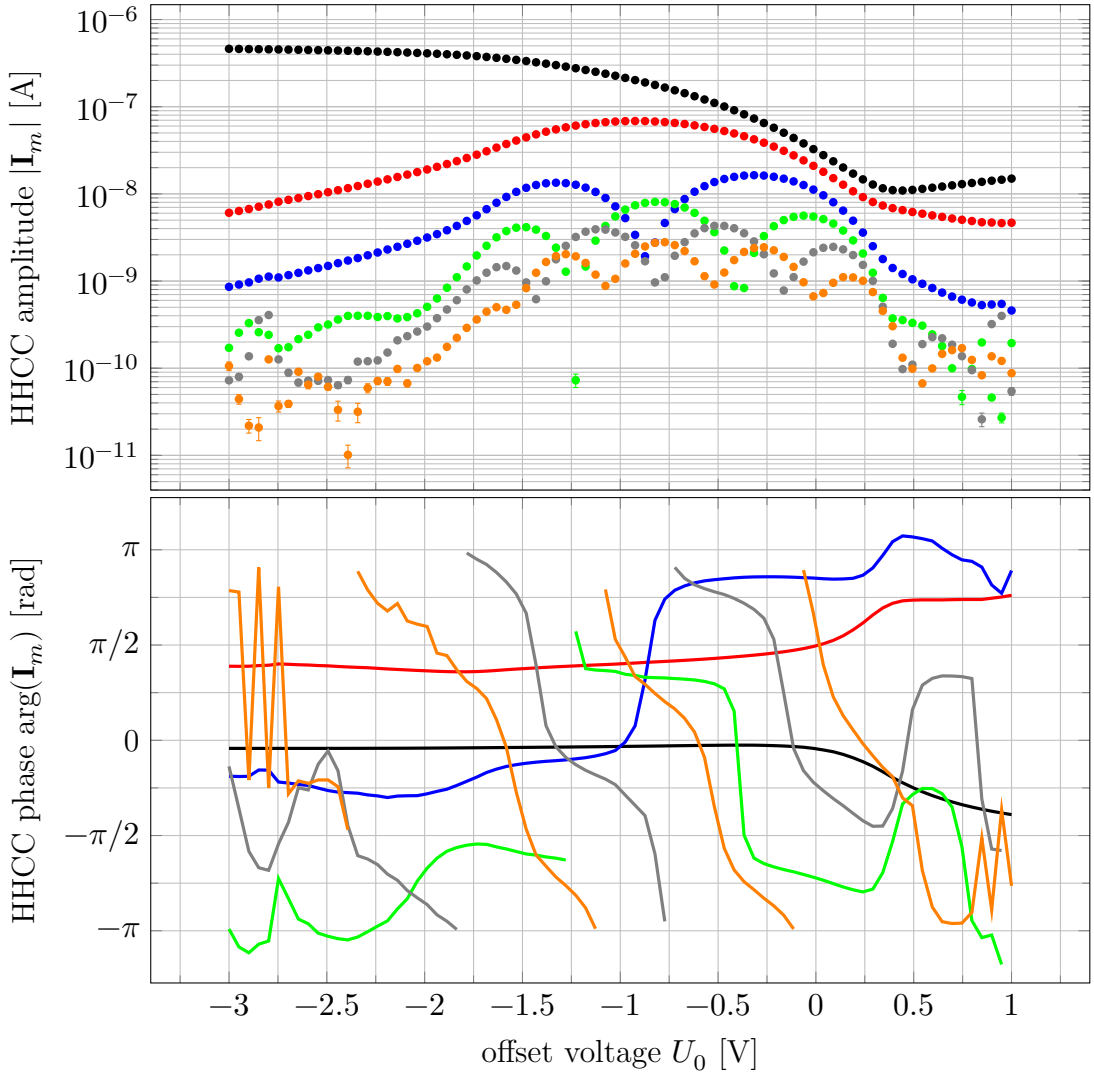

Figure 4.15: Enlarged extract from fig. 4.14 around the nonlinear response in backward current direction. Due to the exceptional non-ohmic dc characteristic (fig. 4.6), nonlinear currents are observed up to the sixth order.

origin and the local minima are instead deformed into the short diagonals of the observed parallelogram-like curves.

Together with amplitude U_1 and offset voltage U_0, the frequency f is the third important quantity to be varied. A prototypical measurement, taken on sample *mz15* is shown in fig. 4.17. The data were acquired with the differential version of the broadband lock-in-based dielectric spectroscopy setup, as described in sec. 3.2.2. Features above 3 kHz, the upper frequency limit of this setup according to app. A, are therefore likely influenced by the experimental setup and can not be ascribed to the sample.

A first test of consistency for this measurement is the comparison of the first and the second harmonic order at $f_1 = 1.5\,\mathrm{kHz}$ with the curves shown in fig. 4.14. Since all characteristic features and amplitude ratios are reproduced correctly and both curves

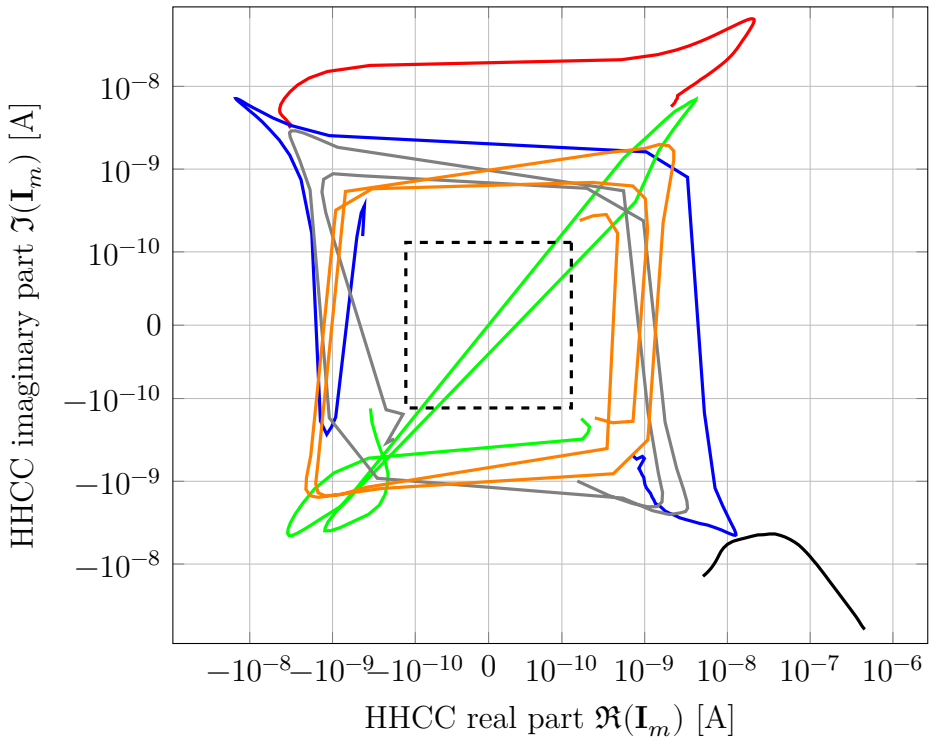

Figure 4.16: Nyquist diagram of the HHCCs shown in fig. 4.15 with varied offset voltage along the lines. For higher orders parallelogram-like curves are observed, where the end points of the longer diagonal indicate the positions of the local maxima. Points within the dashed rectangle at $1.3 \cdot 10^{-10}$ A are below the absolute resolution limit and were therefore omitted.

differ only in their absolute value due to the different excitation amplitude, the consistency of the two measurements is given. As observed in previously presented investigations (sec. 4.2 and fig. 4.14), the conductivity is qualitatively different for positive and negative offset voltages.

In case of $U_0 < 0$ and $U_0 > 6\,\mathrm{V}$, the current is more stable and nearly independent on frequency up to the limit of the experimental setup at $f_1 = 3\,\mathrm{kHz}$. This is in agreement with previous experiments on super-bandgap-light illuminated, but not conductivity-enhanced LNO domain walls by Schröder *et al.* [29]. A much higher precision as compared to those results is achieved here, due to the higher intrinsic conductivity of the enhanced domain walls, in connection with the differential measurement technique. For positive offset voltages $U_0 > 0$, the local minimum in amplitude around $U_0 = 1\,\mathrm{V}$ is much more pronounced at very low frequencies. This agrees with the presumption related to fig. 4.14 of capacitive influences introduced by the imperfect differential compensation that should decrease at lower frequencies.

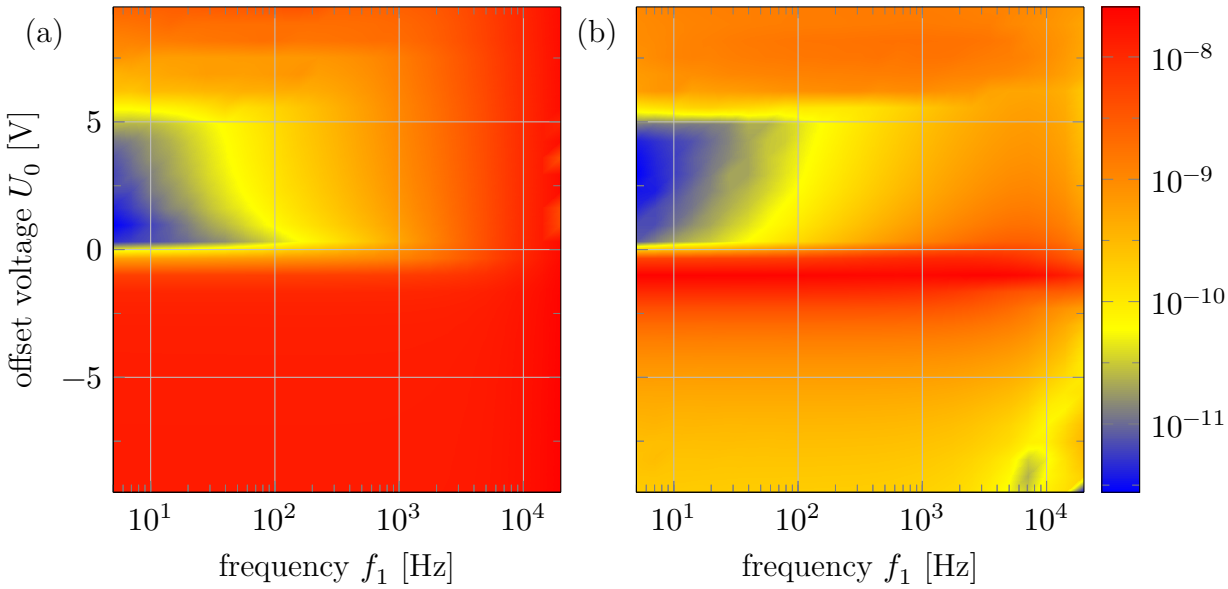

Figure 4.17: First (a) and second (b) HHCC amplitude $|\mathbf{I}_m|$ [A], as a function of fundamental frequency f_1 and offset voltage U_0 for sample *mz15*. While the currents are independent on frequency for $U_0 < 0$ and $U_0 > 6\,\mathrm{V}$, an increase is observed in the intermediate region. $U_1 = 354\,\mathrm{mV}$.

4.5 Discussion

In the following the experimental achievements of sec. 4.2 to 4.4 are evaluated concerning their accuracy, novelty, knowledge gain, and set into context to previous works.

A first main focus of the conducted experiments was to determine the type of non-ohmic conductivity observed in LNO domain walls. Next to the Schottky emission, which turned out to be the relevant mechanism here, Poole-Frenkel emission, or space-charge limited current (SCLC) are commonly observed origins of non-ohmic conductivity. Since previous publications found a semiconductor-like conduction within the domain wall and the samples are contacted by metal electrodes, it was natural to focus on the Schottky type that is typical for metal-semiconductor junctions.

The presumption of a Schottky-type non-ohmic IV-curve motivated an equivalent circuit model for the dc domain wall conductance, which is sketched in figs. 1.1a and 4.5. The equivalent circuit model allowed of explaining all experimental results, comprising room temperature dc conductance, temperature-dependent dc conductance, and ac conductance including a higher-harmonic current contributions (HHCCs) analysis, as different outcomes of the same model.

A second main focus was therefore to determine the model parameters ($R_{p/n}$, $I_{s,p/n}$, $U_{c,p/n}$) from the experimental data. It has to be mentioned that the equivalent circuit only takes into account the domain wall properties and neglects the surrounding bulk,

which was important for the ac conductivity investigations and thereby experimentally realized by differential measurements with mono-domain bulk LNO as reference material. Within the room temperature dc conductivity measurements, a good agreement with the equivalent circuit model was observed and the model parameters could be determined with high precision. Similar values were obtained for the three single domain samples, indicating an appropriate reproducibility of the acquired data. As most important observation, significantly increased values of the ideality factor $n = U_c/(k_B T)$ were observed. According to the theory of metal-semiconductor junctions, this occurs in case of a large doping concentration and leads to the most exciting finding of this thesis: Strong indications were found for a high free charge carrier density due to a high effective donor density of $10^{19}/\mathrm{cm}^3$ within the "domain wall semiconductor".

The intrinsic domain wall charge carrier density of ferroelectric domain wall is a fundamental conduction property and therefore currently intensively studied. Prototypical measurements based on the Hall effect have been demonstrated by Campbell *et al.* [64] on $YMnO_3$ and similar investigations are presently conducted for LNO.

Within the presented experiments, a significant difference between the forward and backward characteristic voltage $U_{c,p/n}$ was observed, indicating in terms of the equivalent circuit model a different charge carrier density on the z+ and z- side. To explain this fact with the charge carrier accumulation on an inclined domain wall, a higher inclination angle should be observed (i.e., in fig. 4.2c) close to the z+ side compared to the z- side that could not be proven clearly so far. It is thereby not appropriate to average over the circular junction area in any case, since the current transport is concentrated on defined current paths [15].

The temperature-dependent dc conductivity measurements down to 90 K were not suited to determine the equivalent circuit model parameters as precisely as the room temperature version. Nevertheless, a qualitative agreement was observed in the dc voltage dependence of the hopping activation energy, which can be predicted based on the theory of Schottky contacts as well. Instead, this method provided insights on the physics of the intrinsic hopping transport within in the domain wall. Taking the broad variety of general thermally activated hopping transport mechanisms as starting point, the actual transport process could be refined to be a simple activated hopping with equal-energy hopping sites. Variable-range hopping approaches as introduced by Mott [36] and Efros and Shklovskii [37] could be excluded. The equal-energy hopping sites are further an important prerequisite for the dipole-tunneling proposed by Xiao *et al.* [26] to model the domain wall conductivity on an atomic level.

Coming back to the first main focus of determining the character of the non-ohmic conductivity, this goal has been accomplished by ac conductivity measurements including a HHCCs analysis. Since the HHCCs strongly depend on the nonlinearity of the dc

IV-characteristic, they are a robust indicator to distinguish conduction models that predict a functional relationship of the latter. By using the derived theoretical framework (app. C), the HHCC amplitudes for a Schottky contact were predicted to increase like a the modified Bessel function with increasing ac voltage on the one hand, and to increase exponentially with respect to the non-oscillating offset voltage on the other hand. Both predictions were qualitatively fulfilled for the multi-domain sample. Further agreement was observed for a single-domain sample by calculating the HHCCs numerically based on the fitted IV-characteristics according to the equivalent circuit model with two Shottky contacts.

An obvious next attempt was to determine the equivalent circuit model parameters by fitting the HHCCs data. This turned out to be not applicable, since the fit parameters suffered from a high uncertainty (sec. 4.4.2). It is therefore concluded that the room temperature dc conductivity measurements are most precise method to determine the equivalent circuit parameters. However, the ac conductivity measurements are a helpful tool to identify the underlying conduction mechanism and to find a sufficient equivalent circuit.

All experimental techniques obtained a good agreement with the proposed equivalent circuit model, being a strong evidence for the Schottky-type non-ohmic conductivity. A further step should be to bring this together with equivalent circuit models for $LiNbO_3$ in literature and construct kind of a universal equivalent circuit. The first model was proposed by Schröder *et al.* [29] to explain the ac conductivity of super-bandgap-light illuminated as-grown domains using a Cole-Cole relation. Secondly, there is the resistor model introduced by Wolba *et al.* [65], relating local domain wall conductivity and inclination angle. Both models were composed from linear circuit elements (resistor, capacitor, constant phase element CPE) only, where the Schottky diodes with their non-ohmic conductivity introduce a fundamentally new aspect into the topic of equivalent circuit modeling. It is expected that the combination of these models predicts new effects to be investigated due to an interaction of components of so far separated models, e.g., the formation of new RC-circuits.

5 Summary and Outlook

Four different lithium niobate domain wall samples were investigated with respect to their nonlinear conductivity contributions, thereof three with a single-poled domain and one multi-poled domain sample. This has been realized by dc and ac conductivity measurements and the results were compared with a proposed equivalent circuit model composed of two diodes and two resistors, c.f. figs. 1.1b and 4.5.

Concerning the ac investigations new experimental setups were designed and fundamentally characterized (apps. A and B). Thereby the detection of higher-harmonic current contributions was a main focus with the aim to detect also non-ohmic conductivity of small size. The achieved level of minimal conductivity required by the sample to be investigated is clearly below the range of highly conducting LNO domain walls, so the latter can be analyzed in detail.

As a first step, room temperature dc conductivity measurements were performed (sec. 4.2). They revealed a good agreement of the observed current-voltage (IV)-curves with the proposed model. Despite the sample preparation was only roughly standardized and done by different persons, similar electric properties of the domain walls have been observed. As expected from the domain wall geometry, a multi-domain sample with several hundred domains exhibited a clearly different characteristic.

For the single-grown head-to-head domain walls, a Schottky-like conduction is observed for low electric fields that is ascribed to the contact electrode-domain wall junction. A strongly increased ideality factor $n \gg 2$ compared to common semiconductors was found, which can be explained by a high charge carrier density inside the domain wall within the thermionic emission theory for metal-semiconductor junctions. The ideality factor was also determined by the following described experimental techniques, and each of them gave a similar consistent picture on this quantity. Nevertheless, the best values of smallest uncertainty were obtained from the room temperature dc conductance measurements. In addition to the rectifying Schottky contacts, the existence and influence of ohmic metal-semiconductor junctions on LNO domain walls is so far unknown and might be subject to future research.

The temperature-dependent dc conductivity measurements (sec. 4.3) confirmed the Schottky-diode-like conduction for low electric fields with an enhanced ideality factor, indicating a high charge carrier density inside the domain wall. For the intrinsic domain

wall conductivity, a thermally activated transport was observed, which can be specified not from the experimental data but with literature results as free small electron polarons. In agreement with previous investigations, a hopping activation energy E_a of 222 meV and 258 meV was found for two different samples and variable-range hopping as introduced by Mott [36] or Efros and Shklovskii [37] could be excluded.

Within the analysis of the temperature and voltage-dependent dc conductivity, the data set was first sliced along the voltage, then the activation energy was determined for any $I_{dc}(T)$-curve, and finally the activation energy was considered as a function of the voltage. The later within the project developed equivalent circuit model enables kind of an orthogonal approach by slicing as first along the temperature, determining for each IV-curve the model parameters ($R_{p/n}$, $I_{s,p/n}$, $U_{c,p/n}$) and considering them as a function of the temperature. This could increase the confidence on the presented results, as the discussed current transport models predict the temperature dependence of the equivalent circuit model parameters as well.

Within the part of ac conductivity measurements, the evolution of higher-harmonic currents due to the non-ohmic IV-curves was investigated under variable ac amplitude and frequency, as well as dc offset voltage (sec. 4.4). On the one hand, the obtained data well agreed with analytical predictions derived from the Taylor expansion of the IV-curve (app. C), concretely expecting a modified Bessel function of first kind dependence of the higher-harmonic current contributions on the ac amplitude and an exponential dependence on the constant offset voltage. On the other hand the higher-harmonic current contributions generated within the equivalent circuit model were evaluated numerically in case of more convoluted higher-harmonic signals, which agreed with the experimental data as well. This was supported by the differential experimental setup scheme to suppress explicitly the influence of the single domain bulk material.

Further experimental improvements are especially requested with respect to the frequency-dependent detection of higher-harmonic contributions, covering so far only two orders of magnitude in frequency between 10^1 and 10^3 Hz. Several publications recently revealed fascinating phenomena on ferroelectrics in the upper kilohertz regime, e.g., identifying internal interface layers, which could be investigated with an improved setup [45, 48]. A convenient way to realize would be the application of IV-converters with a required bandwidth of several MHz.

A further step to go is the nanoscopic replication of the presented macroscopic results using atomic force microscopy. This includes dc conductivity measurements with full IV-curve acquisition on each surface point as well as ac measurements with variable frequency, amplitude, offset voltage, and temperature. To handle the arising multi-dimensional datasets, new evaluation methods such as machine learning demonstrated by Holstad *et al.* [66] should be applied.

The theoretical framework derived in app. C opens the possibility to calculate the higher-harmonic current contribution amplitudes for arbitrary conduction mechanisms, which predict a functional current-voltage relation and compare the calculations with corresponding experimental (also nanscopic) results. An example of such an analysis, which could be improved by this technique, is given by Chen *et al.* [67] on $BiFeO_3$, which also gives an overview on further possible conduction mechanisms in ferroelectrics.
As a general conclusion, the LNO domain walls with enhanced conductivity according to the procedure introduced by Godau *et al.* [15] are a valuable step towards building electronic circuits out of ferroelectric domain walls. Several electronic application relevant properties, e.g., the temperature-dependent resistance, have been demonstrated to be more stable then in as-grown domain walls as shown by Thiessen [16] and motivate further investigations on the ac conductivity of $LiNbO_3$ domain walls for their potential application in nanoelectronics.

A Experimental devices for LIA-based dielectric spectroscopy

The used experimental setups presented in sec. 3.2 are the result of an in-depth analysis of different current measurement principles and specific experimental realizations, which is developed in the following sections.

A.1 Comparison of current measurement principles

The most challenging task in the realized ac experiments is the direct detection of low currents within a bandwidth of several hundred kilohertz. A summary of different possible current measurement principles is given by Keysight Technologies [68]. In the following, the current detection precision of different implementations from the two setup groups described in sec. 3.2.1 (commercial instruments, lock-in amplifiers (LIA)), is compared by their performance with a test device. Thereby, the LIA group will be divided later in two subgroups (of active and passive IV-conversion).

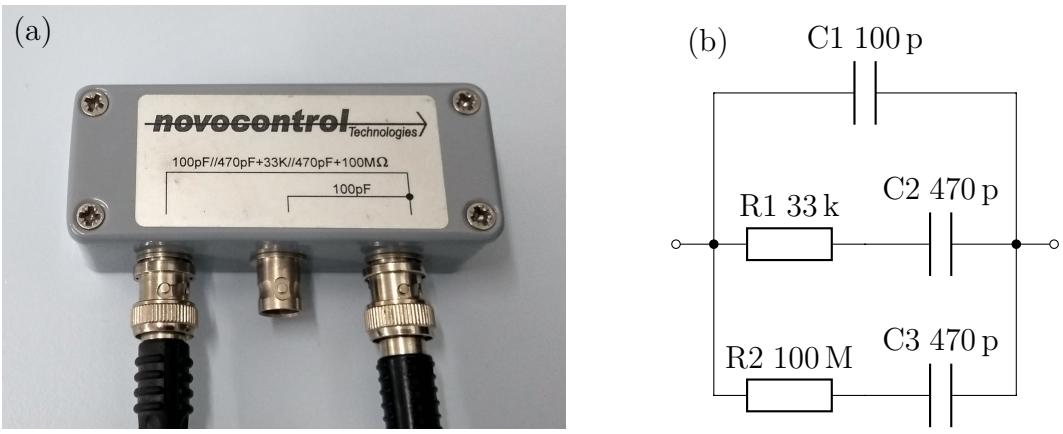

Figure A.1: **(a)** Photography, and **(b)** equivalent circuit of the test device used in order to compare the different current-voltage converters.

A photography of the test circuit manufactured by *Novocontrol Technologies* is shown in fig. A.1a. The relevant circuit elements are completely shielded by a metal box and therefore protected from external electric noise. Further, the equivalent circuit, realized

with commercial circuit elements is shown in fig. A.1b. They mimic a similar characteristic as typical samples in dielectric spectroscopy exhibit below a frequency of 1 MHz. On the one hand, there is the plate-capacitor-like behavior of the contact electrodes. On the other hand, this frequency regime covers typically the cutoff frequencies of RC circuits, formed by internal or external surface capacities and the intrinsic electric resistance. An experimental example of these phenomena is shown and discussed for ferroelectric $YMnO_3$ by Ruff *et al.* [48]. The test circuit contains two of these RC elements with cutoff frequencies $f_{cutoff} = 1/(2\pi RC)$ at 3.39 Hz and 10.3 kHz.

The experimentally observed data for impedance absolute value $|\mathbf{Z}|$ and dielectric loss angle δ_Z as a function of frequency are shown for the different experimental setups in fig. A.2. Several characteristics can be identified, which will be discussed in the following. A first group of similarly behaving setups is formed by the commercial instruments made for dielectric spectroscopy, covering the *Novocontrol Alpha Impedance Measurement System*, the *HP 4284A* LCR-meter, and the *Rohde & Schwarz, ZVL* vector network analyzer. As expected, they resolve amplitude and phase correctly over the full frequency range from 10^{-1} to 10^6 Hz. All setups within this group are restricted to first-harmonic measurements, so excitation voltage and measured current have the same frequency.

A second category are the LIAs with preceding active current-voltage (IV)-converters. These are the *Stanford Research Systems SR830* and *SR860* lock-in amplifiers with internal IV-converters and the *Zurich Instruments UHFLI* lock-in amplifier, combined with a *Femto DLPCA-200* transimpedance amplifier. All three setups determine the current amplitude and phase correctly, as far as the frequency is clearly below the cutoff frequency, which is 70 kHz (and therefore notably lower than the maximum detection frequency of 102 kHz) for the *SR 830* and 400 kHz for the *SR 860* as well as the *DLPCA-200* amplifier in case of the chosen transimpedance A_T of 10^5 V/A. Despite the equal cutoff-frequencies, the $|\mathbf{Z}|$-vs.-f curves of the latter two are not equal, since the amplitude-frequency characteristic is not fully determined by the cutoff frequency only. In general, the deviation in the phase signal becomes significant already at $f_{cutoff}/10$, where as the amplitude is still measured correctly. Above $f_{cutoff}/4$, both quantities differ relevantly from the expected value.

The third category uses the input resistance and the capacity of the *UHFLI* lock-in amplifier as a shunt circuit and leaves out an active current-voltage-conversion. As the characteristic with high input impedance reveals, this setup can be applied successfully, as long as the frequency is far below the eigenfrequency formed by input resistance and capacity, which is here $f_{0,lock-in} = 1/(2\pi R_{shunt} C_{shunt}) = 3.9$ kHz (— curve in fig. A.2). The characteristic of the same setup with a 50 Ω input resistance and zero shunt capacitor reproduces the trend correctly up to 300 kHz, but differs in the phase signal above that frequency. This can be seen as a hint of a so far undetermined input

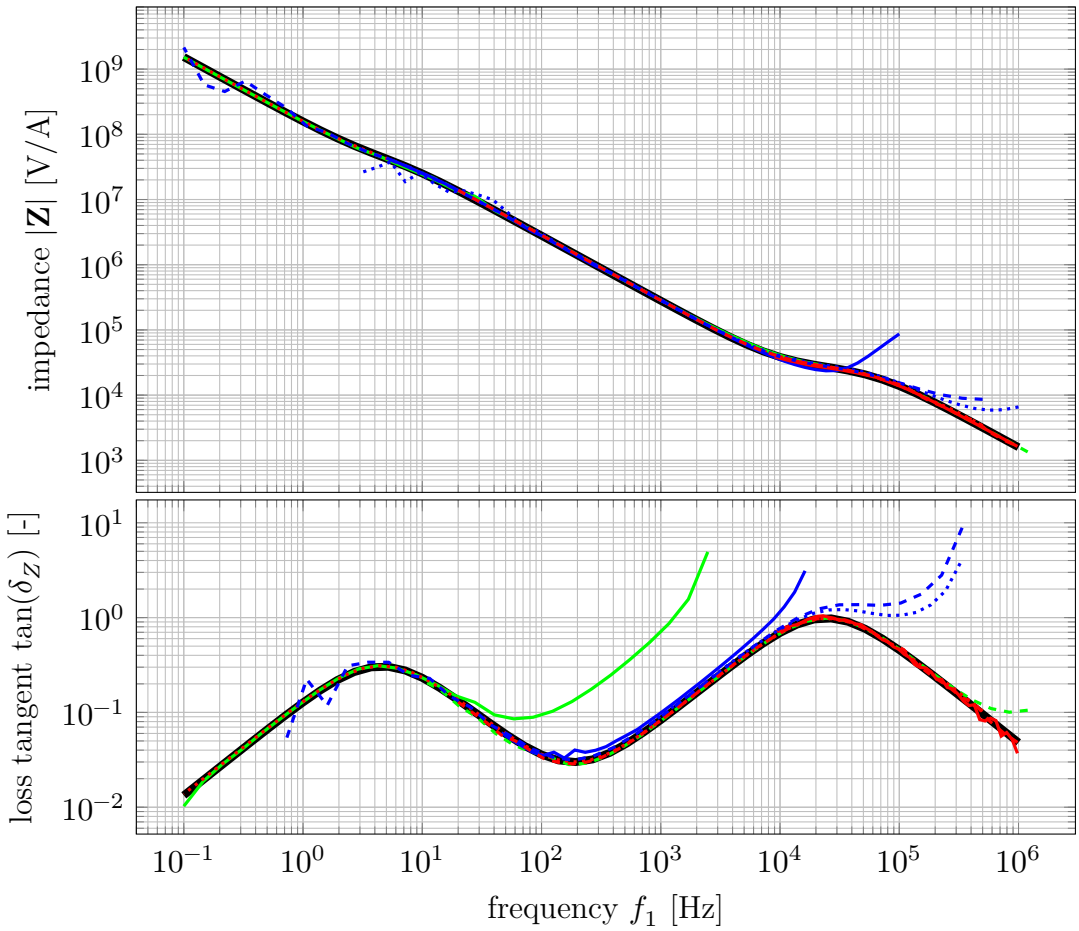

Figure A.2: Test circuit measurements with different dielectric spectroscopy setups revealing their applicable frequency range:
▬: calculation based on the circuit diagram shown in fig. A.1b using common rules for parallel and series composition of linear circuit elements
commercial instruments:
—: *ZVL* network analyzer, output power: 0.1 dBm
- - -: *HP 4284A* LCR-meter, $U_1 = 1\,\mathrm{V}$, acquisition time: long
·····: *Novocontrol Alpha Analyzer*, $U_1 = 1\,\mathrm{V}$
LIA with active IV-conversion:
—: *SR830*, $\tau = \lceil 100/f \rceil$, $A_T = 10^6\,\mathrm{V/A}$, $U_1 = 1\,\mathrm{V}$
- - -: *SR860*, $\tau = \lceil 100/f \rceil$, $A_T = 10^6\,\mathrm{V/A}$, $U_1 = 5\,\mathrm{mV}$
·····: *UHFLI + DLPCA-200*, $A_T = 10^5\,\mathrm{V/A}$, $U_1 = 0.71\,\mathrm{mV}$
LIA with passive IV-conversion:
—: *UHFLI*, $R_{shunt} = 0.984\,\mathrm{M\Omega}$, $C_{shunt} = 41.9\,\mathrm{p\Omega}$, $U_1 = 35.4\,\mathrm{mV}$
- - -: *UHFLI*, $R_{shunt} = 50\,\Omega$, $C_{shunt} = 0$, $U_1 = 354\,\mathrm{mV}$

capacity, forming another RC circuit with cutoff frequency of some MHz and determining the upper frequency validity limit of the passive IV-conversion approach.

The test circuit measurements revealed that first-harmonic investigations should be performed, as expected, with instruments specifically designed for this application. Lock-in amplifiers with external current-voltage conversion also provide reliable results, as long as their upper frequency limit and the discussed effects are taken into account. The shunt-

circuit method was only roughly investigated, since its applicability depends crucially on the ratio of sample and shunt impedance. Most lock-in amplifiers provide only two (50 Ω and high impedance) input modes, giving two measurement ranges. Nevertheless, the method achieved good results at frequencies above 10 kHz, which it is difficult to measure with the broadband current amplifiers under consideration.
According to the test circuit measurements, a LIA-based dielectric spectroscopy setup using an active IV-converter should be able to measure fundamental frequency and HHCC within a certain parameter space. So, the following section highlights the requirements on the individual components within such a setup in order to maximize the parameter space for overtone measurements.

A.2 Components of lock-in amplifier-based dielectric spectroscopy

Naturally, the starting point in dielectric spectroscopy is the signal generator, providing a voltage $U_{out} = U_1 \cos(2\pi f_1 t) + U_0$. The following issues had to be taken into account:

- The **frequency range** or bandwidth had to be chosen according to the demand of the conducted experiment. In the present case this criterion had only minor relevance, since the frequency range was mostly limited by IV-conversion and lock-in amplifier devices.

- The **signal amplitude** U_1 had to be chosen properly according to the dominance of non-ohmic conductivity. A wide amplitude range enables to study the signal amplitude dependency of the HHCCs.

- The **offset voltage** U_0 determines the higher-harmonic generation with a superimposed dc electric field. Due to the previous results by Godau *et al.* [15] and

voltage source	U_1 [V]	U_0 [V]	nom. THD [dB]	meas. THD [dB]
ZI UHFLI	$2 \cdot 10^{-5}$ - 1	± 1	-70	-67
(*ZI UHFLI* + *ITHACO 4302*)	$2 \cdot 10^{-4}$ - 10	± 10	-70 / < -86	-63
Agilent 33250A	$8 \cdot 10^{-4}$ - 7	± 10	-60	-69
Stanford Res. 830	$4 \cdot 10^{-3}$ - 5	0	< -70	-82
Stanf. Res. DS340	0.04 - 7.07	± 10	< -70	-74

Table A.1: Characteristic features of tested signal generators for higher-harmonics generation experiments. The nominal total harmonic distortion (THD) was extracted from the corresponding instrument datasheets. The measured harmonic distortion was acquired with $U_0 = 0.5$ V by measuring the second and third order signals with a *SR830* lock-in amplifier.

Thiessen [16], offset voltages up to $\pm 10\,\mathrm{V}$ were chosen in the present experiments.

- The **(total) harmonic distortion** will be discussed below in more detail.
- The **remote control availability** allows automatized and standardized experiments as described in sec. 3.

Different potential signal generators were investigated, which are compared in tab. A.1. Based on this comparison, the internal signal generators of the two LIAs without external amplifier were already excluded due to the inadequate offset voltage range. Since the internal generators are nevertheless promising candidates with respect to reducing the number of involved instruments, the preamplifier *ITHACO 4302* was investigated to be used together with the *Zurich Instruments UHFLI* LIA.

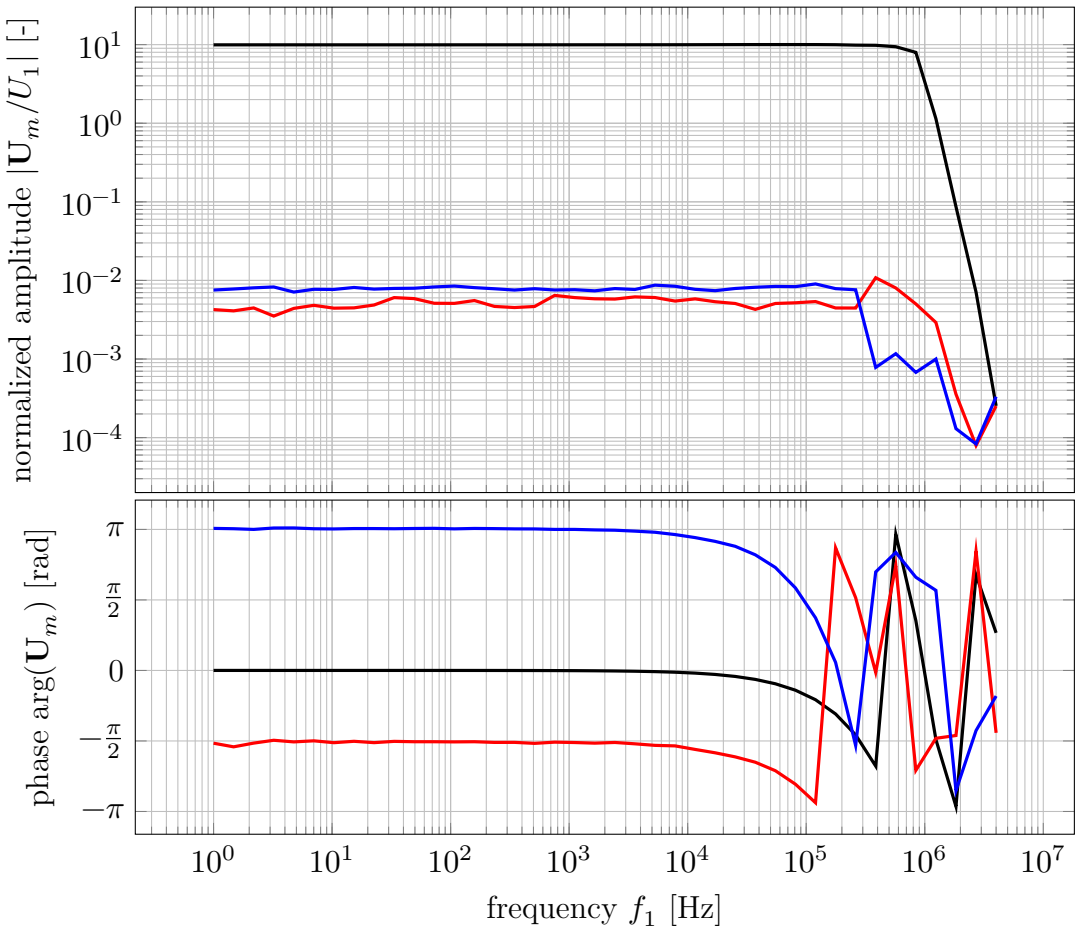

Figure A.3: Amplification characteristic of the *ITHACO 4302* (pre-)amplifier with amplification $A = 10$, measured with the *Zurich Instruments UHFLI* LIA. Depicted are the absolute amplification (upper panel) and phase shift (lower panel) of the first (black), the second (red) and the third (blue) harmonic order using the pre-defined color coding. $U_1 = 50\,\mathrm{mV}$.

The amplifier characteristic was recorded with a LIA and is shown in fig. A.3. As specified by the manufacturer, the amplification is constant up to the cutoff frequency of 1 MHz.

Beyond that, the slope of the first-harmonic contribution is about (36.5 ± 1.6) dB/Octave, and therefore is much steeper than the specified value of 24 dB/Octave. A possible reason might be the preamplifier operating at maximum possible bandwidth. Below the cutoff frequency, the amplification is nearly constant as it is known for the involved Butterworth filter [69]. Nevertheless, also the phase stability is of crucial importance for the proposed experiments. As it can be seen from the lower panel of fig. A.3, the phase can be assumed to be constant up to 4 kHz. Above this frequency, a numerical correction of the measured values is required to collect reliable data, which was not accomplished in this experimental series.

A further influence to be aware of is the existence of higher-harmonic contributions within the signal of the generator. This can turn into a significant systematic error, since the measured HHCC signals are a composition of higher-harmonic contributions generated from the fundamental wave and the linear response of higher-harmonic components of the input signal. Based on the data shown in fig. A.3, a total harmonic distortion (THD) of −63 dB was achieved at frequencies below 1 kHz. As shown in tab. A.1, this could be increased by using an *Agilent 33250A* signal generator up to −69 dB, which is done in the broadband LIA-based setup. Signal generators of even much higher signal clearance are available today especially since they are required to characterize commercial audio devices. A commercially available system of this type is the *Audio Precision APx555* with a total harmonic distortion of −120 dB. Even better results are achieved in experimental environments, e.g., by Groner [70] with −140 dB.

The second component of a LIA-based setup is the current-voltage conversion (see fig. 3.2), which was realized in both finally used setups by a *Femto DLPCA-200* transimpedance amplifier. In most cases, a transimpedance of 10^6 V/A was used. This value is a clear compromise between increasing input noise with increasing amplification and achieving a sufficiently high signal with respect to the input voltage range of the lock-in amplifier. The principles of IV-conversion and their peculiarities are summarized by Keysight Technologies [68].

The last component to be mentioned is the lock-in amplifier. One fundamental parameter to be chosen was the time constant or integration time $\tau = 1/f_{cutoff}$. The signal stability with respect to τ was therefore investigated on a $LiNbO_3$ domain wall and the results are shown in fig. A.4. The horizontal axis represents the number of oscillation periods of the fundamental frequency forming the averaging period, while the vertical axis represents the relative statistical fluctuations of the current components $\Delta I_m/I_m$ with frequencies f_1, $f_2 = 2f_1$, and $f_3 = 3f_1$. Thereby, $10^0 = 1$ means, that the absolute value of the measurement and the statistical fluctuations are of same magnitude and the data-point should be handled with special care. As a rule of thumb, fluctuations below 10^{-1} should be achieved to observe at least rough trends.

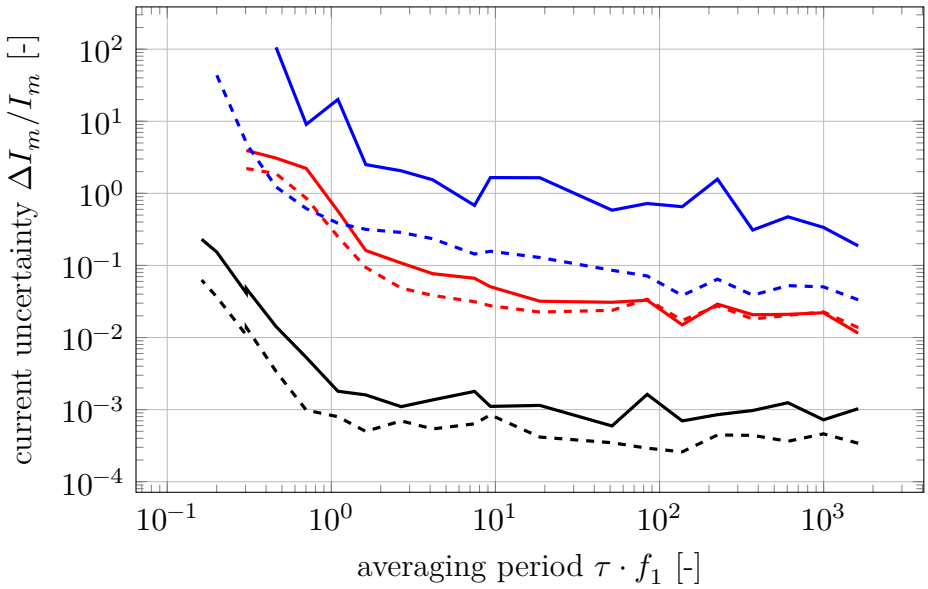

Figure A.4: Statistical uncertainty of real $\Delta\Re(\mathbf{I}_m)/\Re(\mathbf{I}_m)$ (solid line) and imaginary part $\Delta\Im(\mathbf{I}_m)/\Im(\mathbf{I}_m)$ (dashed line) of higher-harmonic current contributions on the LNO sample *mz13c* with respect to the time constant τ of the lock-in amplifier of the first three harmonic orders. The statistical uncertainties were estimated from the standard deviation of 20 identical measurements of each quantity. The experiment was performed with the simple LIA-based setup for higher-harmonic generation at $f_1 = 2\,\mathrm{kHz}$, $U_0 = 6\,\mathrm{V}$, $U_1 = 0.4\,\mathrm{V}$, and third-order low-pass filtering.

As expected, the maximum precision, which is obtained at large time constants for all three harmonics, decreases with the harmonic order, since the absolute value of the measurement decreases as well. With the same argument, the imaginary parts can be measured more precisely, as they dominate the sample response in this case. All curves exhibit a steady value above a certain time constant τ' and a characteristic increase below τ'. For the first order current, the linear response, this transition is situated at $\tau' f_1$ being of the order of one, which indicates a low noise level around the first harmonic signal. The roughly straight line observed below the threshold indicates a power-law-like increase of the statistical fluctuations and in principle allows statements on the signal peak shape in the Fourier space. In second and third order, according to the figure, an averaging over more than 100 oscillation periods was necessary to reach a nearly asymptotic behavior of the precision. As a compromise between measurement time and achievable precision, in most experiments $\tau' f_1 \approx 81$ in connection with a third-order low pass-characteristic was chosen.

LIA-based setups exhibit an intrinsic upper cutoff frequency due to the finite bandwidth of the involved circuit elements. In addition, it is necessary to insert a high-pass filter into the detection path for measurements with constant offset voltage to filter out the constant-current contributions, the so-called ac input coupling of the LIA. This inserts a

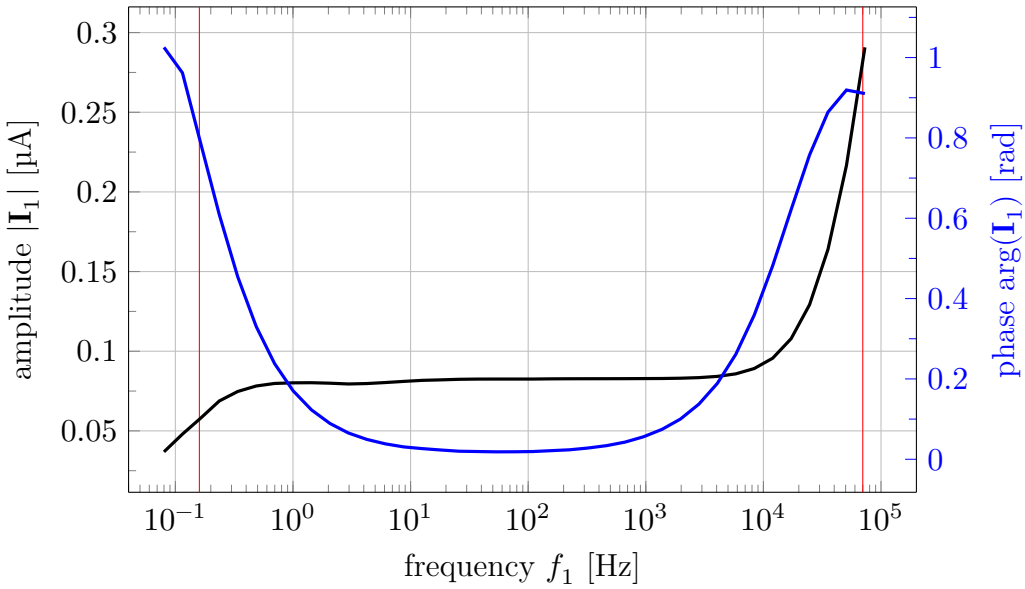

Figure A.5: Amplitude and phase of the first harmonic current for a *BAT 48* Schottky diode, measured with the broadband dielectric spectroscopy setup. It reveals the frequency range for trustworthy amplitude and phase measurements, centered around 100 Hz. The red lines indicate the low cutoff frequency due to the ac input coupling and the high cutoff frequency due to the IV-converter bandwidth. $U_1 = 42\,\mathrm{mV}$, $U_0 = 0$.

lower cutoff frequency and narrows the available frequency range. The simple LIA-based setup using the *ZI UHFLI* LIA was seriously affected by this phenomenon, since the intrinsic low-pass filter of the *UHFLI* has a cutoff frequency of 80 Hz.

To overcome this problem and to enable also frequency-dependent measurements, a second LIA-based setup, the broadband LIA-based setup was introduced as described in sec. 3.2.2. The frequency performance of this setup is shown in fig. A.5. It reveals a trustworthy frequency range between 1 and $3 \cdot 10^3$ Hz for amplitude measurements and between 10^1 and 10^3 Hz for phase measurements. The *BAT 48* Schottky diode was chosen as a test circuit element, since these diodes exhibit a frequency-independent characteristic up to more than 100 MHz and it is granted that all observed effects can be addressed to the measurement setup.

As a general conclusion, the above described broadband LIA-based dielectric spectroscopy setup is a clear improvement compared to the simple LIA-based setup and should be used preferably for future measurements. The only observed drawback of the broadband setup was the higher complexity of the procedures to control the setup, which was however eliminated by the software developed within this project.

B Precision of a LIA-based dielectric spectroscopy setup

Within the following section, the measurement precision of the simple dielectric spectroscopy setup based on the *ZI UHFLI* lock-in amplifier (LIA) and the *Femto DLPCA-200* current-voltage converter with a transimpedance $A_T = 10^6\,\mathrm{V/A}$ as described in sec. 3.2.2 will be analyzed with respect to the sample impedance. To keep the experiment simple, the extension for differential measurements as well as the low-pass filter for ac input coupling of the LIA were omitted (see also sec. 3.2.2). The samples will be treated as a parallel connection, indicated by the index p, of a resistance R_p and a capacity C_p. This decomposition is achievable, if $\Re(\mathbf{Z}) > 0$ and $\Im(\mathbf{Z}) < 0$, which is especially valid for all experimental samples evaluated in this work. The sample impedance is then given by:

$$\mathbf{Z}_{sample}(R_p, C_p, \omega) = \frac{R_p \cdot \frac{1}{\mathrm{j}\omega C_p}}{R_p + \frac{1}{\mathrm{j}\omega C_p}} \tag{B.1}$$

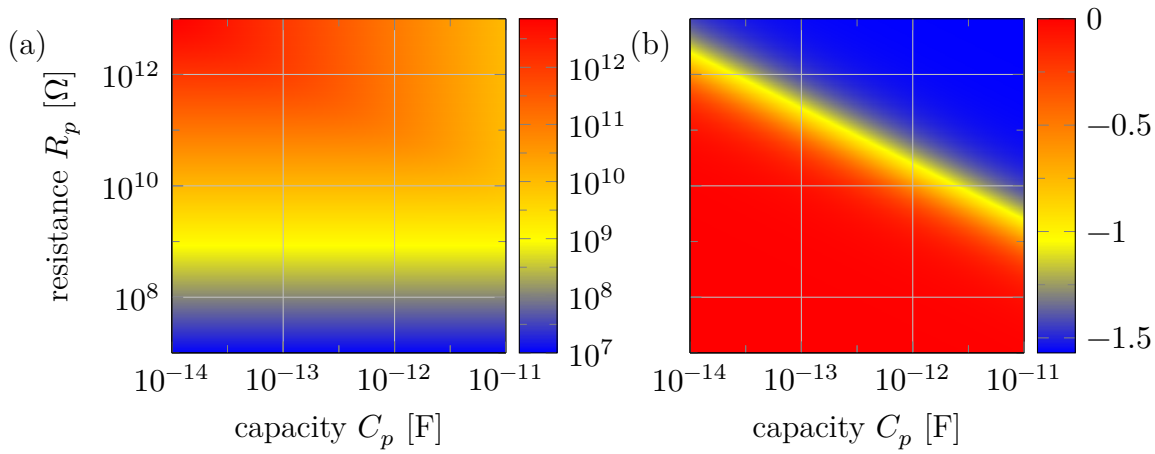

Figure B.1: Absolute value $|\mathbf{Z}|$ [V/A] (a) and phase angle $\arg(\mathbf{Z})$ [rad] (b) of the impedance model given by equation B.1 with $f = \frac{\omega}{2\pi} = 10\,\mathrm{Hz}$.

Absolute value and phase angle of the impedance model are exemplarily shown in fig. B.1 for typical values of R_p and C_p in transition metal oxide samples. As it can be seen from the phase graph, the phase is close to 0 or $-\pi/2 \approx -1.57$ for most samples. It

indicates that the impedance $\mathbf{Z}$ is dominated by either the real or imaginary part, which requires a precise *absolute* phase measurement. This fact will become important later on, as the main proficiency of common setups involving lock-in amplifiers are *relative* phase measurements. Also the yellow transition region between resistively and capacitively dominated samples will become important again later in this analysis.
By determining the impedance of circuit elements with known properties experimentally, the transformation (also termed map) T can be investigated, which relates intrinsic and measured impedance values and therefore characterizes both systematic and statistical uncertainties introduced by the experimental setup. The form of T takes into account that the (circular) frequency can be varied in principle, but the association of intrinsic and measured impedance values is only meaningful for a fixed frequency:

$$T : \mathbb{R} \to (\mathbb{C} \to \mathbb{C}), \omega \mapsto \underbrace{(\mathbf{Z}_{intrinsic} \mapsto \mathbf{Z}_{measured})}_{:=T_\omega} . \tag{B.2}$$

For the experimental realization, industrial surface mount device (SMD) circuit elements with impedances of a similar order of magnitude as the later investigated samples were applied. It turned out that the best conducting domain walls were much more conductive than the investigated test circuit elements, so the signals shown in sec. 4.4 are in most cases clearly above the limits calculated in the following. The circuit elements and their characteristic properties, e.g., the intrinsic resistance R_p and capacitance C_p are listed in tab. B.1. A *Keithley 6517B* electrometer was applied to determine the parallel resistance, while the parallel capacitance was measured with the *Hewlett Packard 4284A* LCR-meter. For any element, $\mathbf{Z}_{measured}$ was determined with the setup considered for 10 Hz, 300 Hz, and 10 kHz.

name	R_p [GΩ]	C_p [pF]	size [imperial code]
R-100M	0.101	0.19	1206
R-1G	0.995	0.19	1206
R-10G	10.33	0.17	1206
R-50G	33.03	0.20	1206
R-500G	557.4	0.15	2512
C-0p1	$> 10^4$	0.27	0603
C-0p3	$> 10^4$	0.49	0603
C-1p2	$> 10^4$	1.32	0805
C-4p7	$> 10^4$	5.01	0805
C-15p	$> 10^4$	15.10	1206

Table B.1: List of circuit elements used to quantify the impedance measurement deviations in lock-in amplifier-based dielectric spectroscopy for high-impedance samples. The imperial code defines tabulated standard sizes for one-port SMD circuit elements [71].

As long as the transformation T_ω between $\mathbf{Z}_{intrinsic}$ and $\mathbf{Z}_{measured}$ is assumed to be

accomplished by linear circuit elements (resistor, capacitor, inductance), T_ω can be represented in the general form as given in equation B.3 [72], also known in mathematics as Möbius transformation, exhibiting several helpful and well-known properties, such as being bijective, so any intrinsic impedance value is associated to exactly one measured value and vice versa.

$$\mathbf{Z}_{measured} = T_\omega[\mathbf{Z}_{intrinsic}] = \frac{\mathbf{a}_\omega \cdot \mathbf{Z}_{intrinsic} + \mathbf{b}_\omega}{\mathbf{c}_\omega \cdot \mathbf{Z}_{intrinsic} + \mathbf{d}_\omega} \quad \text{with} \quad \mathbf{a}_\omega \mathbf{d}_\omega - \mathbf{b}_\omega \mathbf{c}_\omega = 1 \tag{B.3}$$

With this, the complex parameters ($\mathbf{a}_\omega \pm \Delta\mathbf{a}_\omega$), $\mathbf{b}_\omega$, and $\mathbf{c}_\omega$ analogously can be determined from the experimental data ($\mathbf{d}_\omega$ results from the normalization condition). The parameters are summarized in tab. B.2. In case of an ideal setup, the parameters would be expected to suppose the values $\mathbf{a}_\omega = 1$, $\mathbf{b}_\omega = 0$, $\mathbf{c}_\omega = 0$, and, due to the normalization, $\mathbf{d}_\omega = 1$. According to the overview in tab. B.2, this is quite well fulfilled, and for all components of $\mathbf{b}_\omega$ and $\mathbf{c}_\omega$ the uncertainties are of the same order of magnitude or larger then the obtained values. It is concluded that no systematic deviations between intrinsic and measured impedance values were found. In mathematical terms, this means that the map T_ω is compatible to be the unitary transformation ($\mathbb{1} : \mathbb{C} \to \mathbb{C}, \mathbf{Z} \mapsto \mathbf{Z}$).

parameter	unit	10 Hz	300 Hz	10 kHz
$\Re(\mathbf{a}_\omega)$	-	1.000	0.9993	1.004
$\Delta\Re(\mathbf{a}_\omega)$	-	0.005	0.0022	0.009
$\Im(\mathbf{a}_\omega)$	-	0.00036	0.0007	-0.019
$\Delta\Im(\mathbf{a}_\omega)$	-	0.00865	0.0062	0.012
$\Re(\mathbf{b}_\omega)$	Ω	$1.3 \cdot 10^6$	-1521	$-4.0 \cdot 10^4$
$\Delta\Re(\mathbf{b}_\omega)$	Ω	$4.2 \cdot 10^6$	$2.17 \cdot 10^6$	$6.6 \cdot 10^4$
$\Im(\mathbf{b}_\omega)$	Ω	$1.5 \cdot 10^5$	$4.1 \cdot 10^5$	$2.5 \cdot 10^4$
$\Delta\Im(\mathbf{b}_\omega)$	Ω	$344.6 \cdot 10^5$	$2.9 \cdot 10^5$	$19.9 \cdot 10^4$
$\Re(\mathbf{c}_\omega)$	Ω^{-1}	$-1.3 \cdot 10^{-13}$	$-0.05 \cdot 10^{-11}$	$-5.8 \cdot 10^{-10}$
$\Delta\Re(\mathbf{c}_\omega)$	Ω^{-1}	$2.0 \cdot 10^{-13}$	$2.13 \cdot 10^{-11}$	$2.9 \cdot 10^{-10}$
$\Im(\mathbf{c}_\omega)$	Ω^{-1}	$-1.3 \cdot 10^{-12}$	$-1.3 \cdot 10^{-11}$	$0.9 \cdot 10^{-10}$
$\Delta\Im(\mathbf{c}_\omega)$	Ω^{-1}	$0.5 \cdot 10^{-12}$	$1.0 \cdot 10^{-11}$	$1.8 \cdot 10^{-10}$

Table B.2: Fit parameters determined by fitting the experimentally measured impedance of the circuit elements listed in tab. B.1 according to the definition in equation B.3 for different frequencies $f = \omega/2\pi$.

Now, the influence of the uncertainties for typical impedance values will be investigated, since it characterizes the statistical fluctuations introduced by the setup. For this purpose, the map $\tilde{T}_\omega$ with the following definition is introduced:

$$\tilde{T}_\omega : \mathbb{R}^2 \to \mathbb{C}, (R_p, C_p) \mapsto \Delta\mathbf{Z} = \Delta T_\omega^{-1} \left[T_\omega[\underbrace{\mathbf{Z}_{sample}(R_p, C_p, \omega)}_{\widehat{=}\mathbf{Z}_{intrinsic}}] \right]. \tag{B.4}$$

Thereby ΔT_ω^{-1} denotes the uncertainty obtained by Gaussian error propagation due to the uncertain parameters of the inverse transformation derived from T_ω. The inner value $T_\omega[\mathbf{Z}_{sample}]$ is thereby assumed to be precise, having no uncertainty. Despite its abstract definition, the map $\tilde{T}_\omega$ has an intuitive meaning. As a first step, a circular frequency ω has to be fixed and samples of intrinsic impedance composed of R_p and C_p are assumed (equ. B.1). To each of these samples, the map transforms the intrinsic impedance to its measured value ($T_\omega[\mathbf{Z}]$) first, and then calculates the uncertainty when the measured value is back-transformed to its intrinsic value ($\Delta T_\omega^{-1}[...]$). The calculation of this map includes dealing with complex error propagation, which was done following the results of Hall [73]. Since $\Delta\mathbf{Z}$ is still a complex quantity, it is worth to study the derived real value quantities, i.e. $|\Delta\mathbf{Z}|/|\mathbf{Z}|$, $\arg(\Delta\mathbf{Z})$, $\Re(\Delta\mathbf{Z})/\Re(\mathbf{Z})$, and $\Im(\Delta\mathbf{Z})/\Im(\mathbf{Z})$.

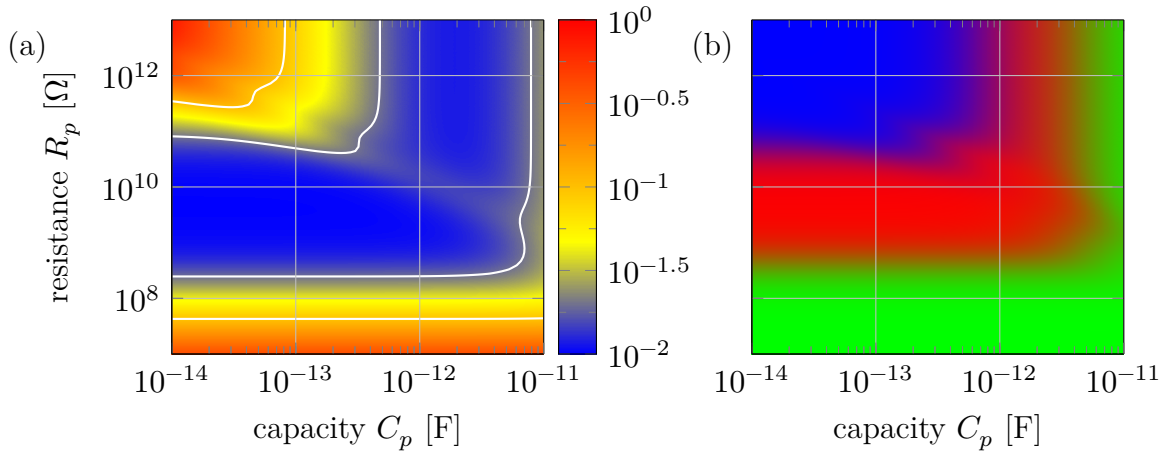

Figure B.2: Relative uncertainty of the absolute impedance $|\Delta\mathbf{Z}|/|\mathbf{Z}|$ for the simple LIA-based dielectric spectroscopy setup. $f = \frac{\omega}{2\pi} = 10\,\text{Hz}$, $U_1 = 7.1\,\text{mV}$, $U_0 = 0$. **(a)** Size of the relative uncertainty over the sample parameter space calculated by applying equation B.4. The white contour lines indicate relative precisions of 10 % and 2 %. **(b)** Dominant Möbius parameter responsible for the observed uncertainty shown in panel (a). The RGB color is composed based on the relative influence of each parameter for a certain pair (R_p, C_p): $\mathbf{a}_\omega$ - proportion of red, $\mathbf{b}_\omega$ - green, $\mathbf{c}_\omega$ - blue.

A first example is given in fig. B.2a, which visualizes the expected relative uncertainty of the impedance absolute value. The differently colored regions can be understood more easily by taking into account the relative contributions of the Möbius transformation parameters $\mathbf{a}_\omega$, $\mathbf{b}_\omega$, and $\mathbf{c}_\omega$, and their uncertainties, which are shown in fig. B.2b. For example, a blue coloring in this graph means that $|\Delta\mathbf{Z}|$ is dominated by the contributions originating from $\Delta\mathbf{b}$.

Two main areas in the R_p-C_p-plane are identified to be critical for impedance absolute value measurements. Firstly, the upper left corner in the picture, corresponding to high R_p and low C_p needs to be considered. The two tendencies together result in ultra small absolute current values, which can be measured only with low precision. In terms of the parameters, the transformation is dominated in this region by the ratio $\mathbf{a}_\omega/\mathbf{c}_\omega$. Since $\mathbf{c}_\omega$ is of small absolute value (in an ideal setup equal to zero), it features a high relative uncertainty and the total uncertainty of $|\mathbf{Z}|$ becomes dominated by $\Delta\mathbf{c}_\omega$.
Secondly, the area at the bottom and the area at the right edge are discussed. Here, the absolute impedance values are quite small, as shown in fig. B.1a. In terms of the contributions, this means that the proportion of $\mathbf{a}_\omega \cdot \mathbf{Z}$ becomes small compared to $\mathbf{b}_\omega$, and the uncertainty is dominated by $\Delta\mathbf{b}_\omega$, as seen in fig. B.2b. This effect is intensified by the phenomenon that only a few test circuit elements correspond to these regions and therefore the parameter $\mathbf{b}_\omega$ is only roughly determined.
A further feature to be noticed is the light grayish strip of increased uncertainty within the blue area in fig. B.2a, connecting the two formerly mentioned areas. Its position corresponds to the transition region between resistively and capacitively dominated samples, shown in fig. B.1b as a yellow strip. It can be explained by the summation of uncertainties originated by $\Re(\Delta\mathbf{a}_\omega)$ and $\Im(\Delta\mathbf{a}_\omega)$, both of them contributing along this line. Consequently, the area with $\Delta\mathbf{a}_\omega$ being the main contributor of uncertainty is elongated along this line as observed in fig. B.2b.
The studies of uncertainties can be extended by evaluating $\Delta\mathbf{Z}$ in polar and Cartesian coordinates and taking the frequency dependence into account, which is depicted in figs. B.3 and B.4. As most obvious tendency, the apex of the upper left red area shifts with increasing frequency towards smaller parallel resistance, which originates from the equivalent shift of the separation line of resistive and capacitive samples (fig. B.1b) due to a decreasing reactance. The uncertainties in absolute value and phase show the smallest values at 300 Hz, which is likely due to increased $1/f$-noise at lower frequencies and the increasing influence of the phase shift of the current amplifier at higher frequencies. Concerning real and imaginary part shown in fig. B.4, they can be measured precisely only if they dominate the impedance, and consequently the areas of possible precise measurements are clearly separated by the above mentioned transition line. All effects discussed above for the absolute impedance uncertainty can be found in the Cartesian coordinate evaluation as well (fig. B.4).
Overall, a strong frequency dependence of the achievable precision for a "constant sample", i.e. R_p and C_p being constant as a function of frequency, is observed. This is an important restriction concerning measurements with variable frequency, which is the most common quantity be to swept in dielectric spectroscopy investigations. On the other hand, lock-in amplifiers are more commonly used in experiments with constant frequency, emphasizing

the unconventional character of LIA-based dielectric spectroscopy.
In conclusion, only the area of large uncertainty identified in the upper left corner for large resistance and small capacitance has to be excluded to avoid artifacts introduced by the experimental setup. The observed uncertainties in the bottom and right edge areas for small resistance or large capacitance are caused by the small number of test circuits within these regions, leading to a low-accuracy determination of the corresponding Möbius parameters in these regions. Nevertheless, the uncertainties would be directly estimated from the statistical fluctuations in a real experiment in these regions, which are expected to be much lower than the estimation based on the inaccurately determined parameters.

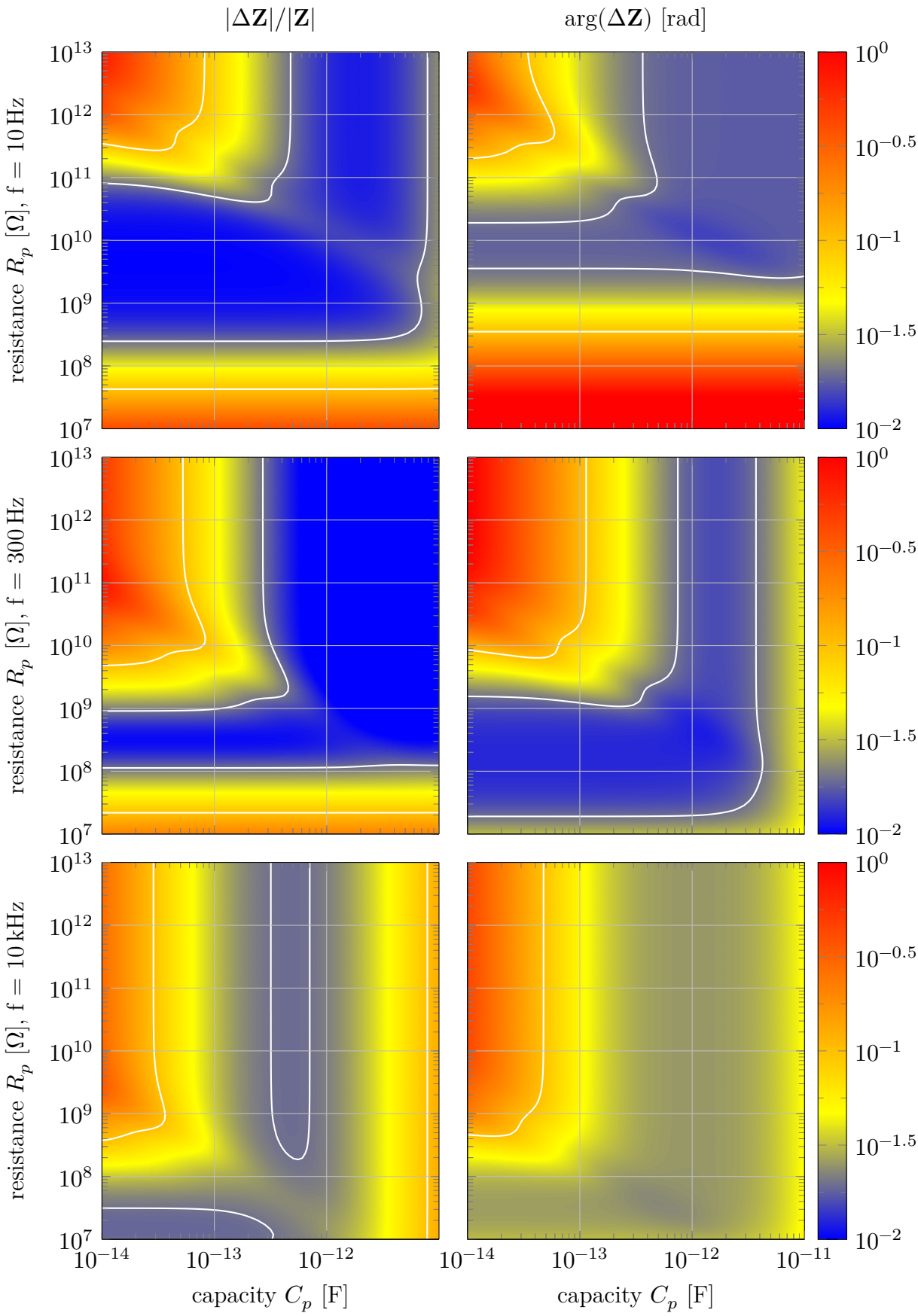

Figure B.3: Achievable precision for high-impedance samples with the simple LIA-based dielectric spectroscopy setup (fig. 3.2, tab. 3.2), calculated by equ. B.4 in polar coordinates for frequencies $f = \frac{\omega}{2\pi} = 10\,\text{Hz}$, $300\,\text{Hz}$, and $10\,\text{kHz}$. The white contour lines indicate the levels 0.1 and 0.02.

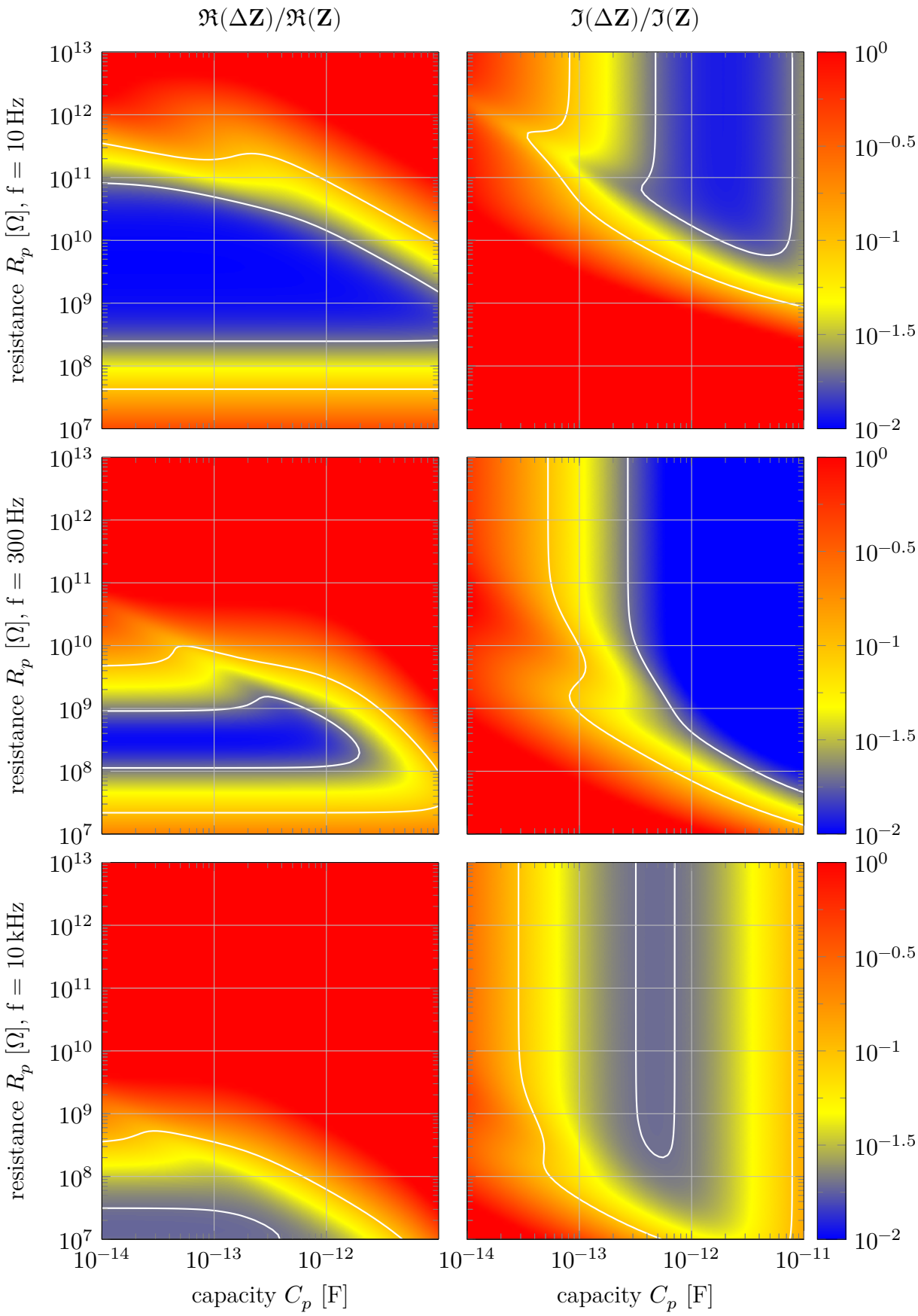

Figure B.4: Continuation of fig. B.3, visualizing the achievable precision, evaluated in Cartesian coordinates.

C Higher-harmonic current generation in nonlinear circuit elements at low frequencies

The Fourier expansion of the electric current is calculated for a one-port circuit element with an analytic (Taylor-expandable) IV-curve in case of a sinusoidal ac voltage excitation. Based on this result, the influence of a constant dc offset voltage and of a non-sinusoidal excitation is discussed, using also numerical calculations to take more complex scenarios into account.

C.1 Preliminary considerations

We assume an electric one-port, which is fully determined by its dc characteristic IV-curve. This means that the current I and the applied voltage U fulfill their relation $I(U)$ for every moment in time. This is especially the case in a real system, when the frequency of U is chosen to be low enough, so that capacitive and inductive contributions are negligible. The condition can be formally expressed as $\Re(\mathbf{Z}) \gg \Im(\mathbf{Z})$ and $\partial\Re(\mathbf{Z})/\partial f \ll \Re(\mathbf{Z})/f$, where $\Re(\mathbf{Z})$ and $\Im(\mathbf{Z})$ are the real and imaginary part of the circuit element impedance, respectively. Depending on the device under inspection, the valid frequency range for this condition can differ by orders of magnitude. For a 500 GΩ resistor, the upper frequency limit, until which these assumptions are valid, was found to be of the order of 1 Hz, while for the Schottky diode applied in sec. 4.4, the condition was still valid at 100 kHz.
In the following, we assume a harmonic excitation with circular frequency ω. Furthermore, we assume that the dc characteristic curve $I(U)$ can be expanded in a Taylor series with respect to the applied voltage:

$$I(U) = \sum_{k=0}^{\infty} a_k U^k. \tag{C.1}$$

Here, the Taylor coefficients a_k are introduced. Due to periodicity of the voltage in time, also the current can be expanded as a sum of harmonic contributions, as given in equ. C.2, which is known as the Fourier expansion. The goal of the following derivation is to

determine the complex quantities $\mathbf{I}_m$. Especially due to the nonlinear dc IV-characteristic curve, also the components for $m > 1$ contribute to the sum.

$$I(t) = I_0 + \sum_{m=1}^{\infty} |\mathbf{I}_m| \sin(m\omega t + \arg(\mathbf{I}_m)) \tag{C.2}$$

If the IV-characteristic is expanded around $U = 0$, the coefficient a_0 is zero for almost all cases ($U = 0 \rightarrow I = 0$). An exception, which can be handled as well in some cases, is a circuit element with an intrinsic voltage source, e.g., due to relevant photovoltaic effects. In the following derivation, we additionally include the case of a constant offset voltage U_0 with $U = U_0 + U_1 \sin(\omega t)$. Mathematically, we can trace this back to the case of a purely sinusoidal excitation ($U = U_1 \sin(\omega t)$) by defining $\tilde{U} = U - U_0$ and calculate the series expansion in powers of $\tilde{U}$. Then, the new Fourier coefficients $\tilde{a}_k$ are determined by comparison of coefficients with respect to U by:

$$\sum_{k=1}^{\infty} a_k U^k = \sum_{k=0}^{\infty} \tilde{a}_k \underbrace{(U - U_0)}_{=\tilde{U}}{}^k. \tag{C.3}$$

Subsequently, we may write the characteristic IV-curve as a series expansion of $\tilde{U}$ with $\tilde{a}_0 \neq 0$. The case of a constant offset voltage is therefore covered, if we allow $a_0 \neq 0$ and we can assume in the following $U(t) = U_1 \sin(\omega t)$. Since the derivation deals with nonlinear contributions, the complex ac calculation formalism can not be applied and complex numbers are only used to represent the complex harmonic current contributions $\mathbf{I}_m$.

C.2 Fourier expansion of the electric current

The general formulas for $\mathbf{I}_m$ are given below in equ. C.4 and follow directly from the theory of Fourier transformations [74, p. 138]. These equations also motivate to use a lock-in amplifier (LIA) for the practical realization of higher-harmonic current measurements, since this is exactly the signal processing done by a LIA. Since we know the frequency of the reference voltage, it is sufficient to integrate over a single fundamental frequency period, which corresponds to choosing $\tau = \frac{2\pi}{\omega}$.

$$\begin{aligned} \Re(\mathbf{I}_m) &= \frac{1}{\tau} \int_0^{\tau} \sin(m\omega t) I(t) dt, \\ \Im(\mathbf{I}_m) &= \frac{1}{\tau} \int_0^{\tau} \cos(m\omega t) I(t) dt. \end{aligned} \tag{C.4}$$

In the following, we focus on the integral of the real part, since the result for the imaginary part can be calculated analogously. As an intermediate step, we investigate the following

integral:

$$\begin{aligned}\int \sin(mx)\sin^k(x)dx &\underset{[75,\text{ eq. }1.320]}{=} \int \sin(mx)\frac{1}{2^k}\sum_{l=0}^{k}\binom{k}{l}\cos((k-2l)(x-\pi/2))dx \\ &= \frac{1}{2^k}\sum_{l=0}^{k}\binom{k}{l}\int \sin(mx)\cos((k-2l)(x-\pi/2))dx \\ &\underset{[76,\text{ eq. }4.3.33]}{=} \frac{1}{2^k}\sum_{l=0}^{k}\binom{k}{l}\int \frac{1}{2}[\sin((m-k+2l)x+(k-2l)\pi/2) \\ &\quad + \sin((m+k-2l)x-(k-2l)\pi/2)]dx.\end{aligned} \tag{C.5}$$

As expected, the frequency spectrum is composed of oscillations with an integer multiple of the fundamental frequency only. Since we integrate over a full period later, the integral vanishes whenever the prefactor of x (the latter will be replaced later by ωt) in the last line is unequal zero [76, eq. 4.3.140]. Therefore, only two cases will contribute to the final result:

$$\begin{aligned}&\text{(I)} \quad m-k+2l=0 \Leftrightarrow k=2l+m, \\ &\text{(II)} \quad m+k-2l=0 \Leftrightarrow k=2l-m.\end{aligned} \tag{C.6}$$

We can now solve the integrals from equ. C.4 using the Taylor expansion in equ. C.1:

$$\begin{aligned}\Re(\mathbf{I}_m) &= \frac{1}{2\pi/\omega}\int_0^{2\pi/\omega}\sin(m\omega t)\sum_{k=0}^{\infty}a_k U^k(t)dt \\ &= \frac{1}{2\pi/\omega}\sum_{k=0}^{\infty}a_k U_1^k\int_0^{2\pi/\omega}\sin(m\omega t)\sin^k(\omega t)dt \\ &\underset{\text{equ. C.5}}{=} \underset{\text{(I)}}{+}\frac{1}{2\pi/\omega}\sum_{l=0}^{\infty}a_{2l+m}\left(\frac{U_1}{2}\right)^{2l+m}\binom{2l+m}{l}\int_0^{2\pi/\omega}\frac{1}{2}\sin\left(-m\frac{\pi}{2}\right)dt \\ &\quad \underset{\text{(II)}}{+}\frac{1}{2\pi/\omega}\sum_{l=m}^{\infty}a_{2l-m}\left(\frac{U_1}{2}\right)^{2l-m}\binom{2l-m}{l}\int_0^{2\pi/\omega}\frac{1}{2}\sin\left(-m\frac{\pi}{2}\right)dt.\end{aligned} \tag{C.7}$$

By using the index transformation $l' = l-m$ on the second sum, we see that contributions (I) and (II) are equal and can be condensed. In addition, we can accomplish the - now trivial - integrations. This results in:

$$\Re(\mathbf{I}_m) = \sin\left(-m\frac{\pi}{2}\right)\sum_{l=0}^{\infty}a_{2l+m}\left(\frac{U_1}{2}\right)^{2l+m}\binom{2l+m}{l}. \tag{C.8}$$

The result of the imaginary part is analogous, except the sine is replaced by the cosine function. Combining real and imaginary part leads to the final result, representing amplitude and phase of all components $m \in \mathbb{N}_0$ of the higher-harmonic current contributions:

$$\mathbf{I}_m = \sum_{l=0}^{\infty} a_{2l+m} \left(\frac{U_1}{2}\right)^{2l+m} \binom{2l+m}{l} \cdot \left[\cos\left(m\frac{\pi}{2}\right) - \mathbf{i}\sin\left(m\frac{\pi}{2}\right)\right]. \tag{C.9}$$

In some cases, the further assumption of $\forall k \in \mathbb{N} : a_k \geq 0$ is valid. The assumption is notably violated, if a one-port circuit element that fulfills the assumption in one orientation is measured in opposite orientation, e.g., in case of a diode, reverse biasing is defined to be the positive direction. This can be proven similar to equ. C.3, ending up with $\tilde{a}_{k,reversed} = (-1)^k a_k$ and $\forall k \in \mathbb{N}, 2 \nmid k : \tilde{a}_{k,reversed} \leq 0$. Whenever the assumption is valid, the result can be simplified to:

$$|\mathbf{I}_m| = \sum_{l=0}^{\infty} a_{2l+m} \left(\frac{U_1}{2}\right)^{2l+m} \binom{2l+m}{l}, \tag{C.10a}$$

$$\arg(\mathbf{I}_m) = -\frac{\pi}{2}(m-1). \tag{C.10b}$$

As expected, the amplitudes depend on the coefficients a_k. Especially, any order m is influenced by an infinite number of coefficients (a_m, a_{m+2}, a_{m+4}, ...). On the other hand, the phase is completely independent on the IV-curve.
If the dc characteristic is only weakly nonlinear, formally defined as $\forall k \in \mathbb{N} : a_k \gg a_{k+1}U_1$, the higher-harmonic currents are closely related to the higher derivatives of the dc characteristic IV-curve:

$$|\mathbf{I}_m| \underset{l=0}{=} a_m \left(\frac{U_1}{2}\right)^m = a_m m! \cdot \left[\frac{1}{m!}\left(\frac{U_1}{2}\right)^m\right] = \left.\frac{\partial^m I}{\partial U^m}\right|_{U=0} \left[\frac{U_1^m}{2^m \cdot m!}\right]. \tag{C.11}$$

C.3 The Schottky barrier as a special case

As described in sec. 4.4, the higher-harmonic current contributions of Schottky barriers are investigated in the experimental part of this thesis. Thereby, a Schottky barrier inside an industrial Schottky diode was used as a reference for comparison with the LNO domain walls. The characteristic IV-curve, which corresponds to the well-known (Shockley) diode equation (discussed also in sec. 2.3), and its series expansion is given by:

$$I = I_s \left[\exp\left(\frac{U}{nU_T}\right) - 1\right] = \sum_{k=1}^{\infty} \underbrace{\frac{I_s}{k! \cdot (nU_T)^k}}_{=a_k,\, a_0=0} U^k. \tag{C.12}$$

Here, I_s is the reverse leakage current, n the ideality factor, and $U_T = \frac{k_B T}{q}$ the thermal voltage. The harmonic contributions can by calculated by the simplified version given in equation C.10a, since the coefficients fulfill the assumption of $\forall k \in \mathbb{N}_0 : a_k \geq 0$. The harmonic current contributions are given by:

$$\begin{aligned} |\mathbf{I}_m| &= \sum_{l=0}^{\infty} \frac{I_s}{(2l+m)!(nU_T)^{2l+m}} \left(\frac{U_1}{2}\right)^{2l+m} \binom{2l+m}{l} \\ &= I_s \sum_{l=0}^{\infty} \frac{1}{(2l+m)!} \left(\frac{U_1}{2 \cdot nU_T}\right)^{2l+m} \binom{2l+m}{l} \\ &= I_s \cdot \mathrm{I}_m \left(\frac{U_1}{nU_T}\right). \end{aligned} \tag{C.13}$$

Thereby I_m (in non-italic letter) denotes the modified Bessel function of first kind (not to be confused with Bessel functions of first kind J) of order m, with the definition as given by Abramowitz and Stegun [76, equ. 9.6.10]. In this special case, the Fourier expansion can be derived directly from equ. 9.6.35 in in the same reference.
We are further interested in the harmonic coefficients for the case of a finite offset voltage U_0, which can be calculated using equ. C.3, leading to:

$$\sum_{k=1}^{\infty} \frac{I_s}{k!(nU_T)^k} U^k = \sum_{l=0}^{\infty} \tilde{a}_l (U - U_0)^l = \sum_{l=0}^{\infty} \tilde{a}_l \sum_{k=0}^{l} \binom{l}{k} U^k (-U_0)^{(l-k)}. \tag{C.14}$$

As this will be helpful later on, we change the summation limits on the right hand side from $\sum_{l=0}^{\infty} \sum_{k=0}^{l}$ to $\sum_{k=0}^{\infty} \sum_{l=k}^{\infty}$. It can be easily confirmed that the new summation covers the same pairs of (k, l). Since the coefficients $\tilde{a}_l$ are independent on U, we can perform a comparison of coefficients and get a conditional equation for each k. Performing the two conversions results in:

$$\forall k \in \mathbb{N} : \frac{I_s}{k!(nU_T)^k} = \sum_{l=k}^{\infty} \tilde{a}_l (-U_0)^{(l-k)} \binom{l}{k}. \tag{C.15}$$

Since the coefficients $\tilde{a}_l$ are equal to a_l in case of $U_0 = 0$, we use the Ansatz:

$$\tilde{a}_l = a_l \cdot g(U_0, nU_T, l) = \frac{I_s}{l!(nU_T)^l} \cdot g(U_0, nU_T, l) \tag{C.16}$$

with $g(U_0 = 0, nU_T, l) = 1$. Inserting the Ansatz into the right hand side expression of

equ. C.15 clarifies the structure of g:

$$\begin{aligned}
&\sum_{l=k}^{\infty} \frac{I_s}{\cancel{l!}(nU_T)^l} g(U_0, nU_T, l)(-U_0)^{(l-k)} \frac{\cancel{l!}}{k!(l-k)!} \\
&\underset{m=k-l}{=} \sum_{m=0}^{\infty} \frac{I_s}{(nU_T)^{(k+m)}} g(U_0, nU_T, k+m)(-U_0)^m \frac{1}{k!m!} \\
&= \frac{I_s}{k!(nU_T)^k} \sum_{m=0}^{\infty} \frac{1}{m!} \left(\frac{-U_0}{nU_T}\right)^m g(U_0, nU_T, k+m).
\end{aligned} \tag{C.17}$$

The last line indicates that $g = \exp(U_0/U_T)$ fulfills equ. C.15, because the summation over m then represents the exponential series of $-U_0/U_T$, which cancels with g and the left side of equ. C.15 remains. This means that in case of $U_0 \neq 0$, the current amplitude of each harmonic contribution is given by:

$$|\mathbf{I}_m|(U_0) = |I_m|(U_0 = 0) \cdot \exp\left(\frac{U_0}{U_T}\right) = I_s \cdot \mathrm{I}_m \left(\frac{U_1}{nU_T}\right) \exp\left(\frac{U_0}{nU_T}\right). \tag{C.18}$$

Equation C.18 is an extension of equ. C.13. It makes a quantitative prediction for the higher-harmonic contributions as a function of the intrinsic diode properties I_s and nU_T and the excitation-voltage parameters U_0 and U_1. These predictions are used in sec. 4.4 to be compared with the results on an industrial Schottky diode and a LNO domain wall.

C.4 Influence of higher-harmonic excitation

In the previous sections, we assumed the excitation voltage to be perfectly sinusoidal. Nevertheless, in every experimental realization higher-harmonic excitations as discussed in app. A.2 exist. In the following, we analyze the influence of higher-harmonic voltage excitation on the higher-harmonic current generation. We therefore assume now the following form of excitation taking only one single order r of harmonic distortion into account:

$$\begin{aligned}
U(t) &= U_1 \sin(\omega t) + U_r \sin(r\omega t + \phi_r) \\
&= U_1 \sin(\omega t) + U_r \cos\phi_r \sin(r\omega t) + U_r \sin\phi_r \cos(r\omega t).
\end{aligned} \tag{C.19}$$

For the analytical derivation, we restrict our considerations to the case of $r = 2$, $\phi_2 = \pi/2$, and $U_2 \ll U_1$. As seen in equ. C.7, we have to evaluate powers of $U(t)$, which now exhibit

the form:

$$
\begin{aligned}
U(t)^k &= [U_1 \sin(\omega t) + U_2 \sin(2\omega t + \phi_2)]^k \\
&= \sum_{l=0}^{k} U_2^l \sin^l(2\omega t + \phi_2) U_1^{(k-l)} \sin^{(k-l)}(\omega t) \\
&\approx \underbrace{U_1^k \sin^k(\omega t)}_{l=0} + \underbrace{U_1^{k-1} \sin^{k-1}(\omega t) \cdot U_2 \sin(2\omega t + \phi_2)}_{l=1} \\
&= U_1^k \sin^k(\omega t) + U_1^{k-1} U_2 \sin^{k-1}(\omega t) \sin\phi_2 \cos(2\omega t) \\
&\underset{[76,\ \text{equ. } 4.3.25],\ \sin\phi_2=1}{=} U_1^k \sin^k(\omega t) + U_1^{k-1} U_2 [\sin^{k-1}(\omega t) - 2\sin^{k+1}(\omega t)].
\end{aligned}
\tag{C.20}
$$

By inserting this result into equ. C.8, the following expression for the real part components is achieved:

$$
\begin{aligned}
\Re(I_m) = &\sin\left(-m\frac{\pi}{2}\right) \sum_{l=0}^{\infty} \frac{U_1^{2l+m-2}}{2^{2l+m}} \binom{2l+m}{l} \cdot \\
&\cdot [a_{2l+m} U_1^2 + a_{2l+m+1} U_1^2 U_2 - 2a_{2l+m-1} U_2].
\end{aligned}
\tag{C.21}
$$

Obviously, the term in the square brackets determines, whether the higher-harmonic excitation distorts the measurement significantly. The term inside the bracket can be specified for the Schottky barrier model by inserting the coefficients a_k from equ. C.12 and factor out U_1^2:

$$
\left[1 + \frac{U_2}{(2l+m+1)(nU_T)} - 2\frac{U_2(nU_T)(2l+m)}{U_1^2}\right]. \tag{C.22}
$$

Since the terms of low l are the dominant ones and m is of the order of one, the terms $(2l+m+1)$ and $(2l+m)$ can be neglected. The harmonic distortion is therefore mainly influenced by the ratio of the distortion amplitude U_2 and the modified thermal voltage nU_T (second term), as well as by the harmonic-excitation amplitude U_1 (third term).
To investigate the influence of harmonic excitations with $r > 2$, the harmonic current contributions (equ. C.4) can be evaluated numerically for a specific characteristic curve, e.g., the Schottky barrier (equ. C.12) with distorted excitation voltage (equ. C.19). The result is shown in fig. C.1, depicting the change in the mth order current contribution due to a higher-harmonic excitation of rth order. Independent on the IV-curve of the investigated circuit element, we expect a non-constant curve in case of $m = r$, since the distortion causes an increase of the amplitude by interfering via the linear term of the

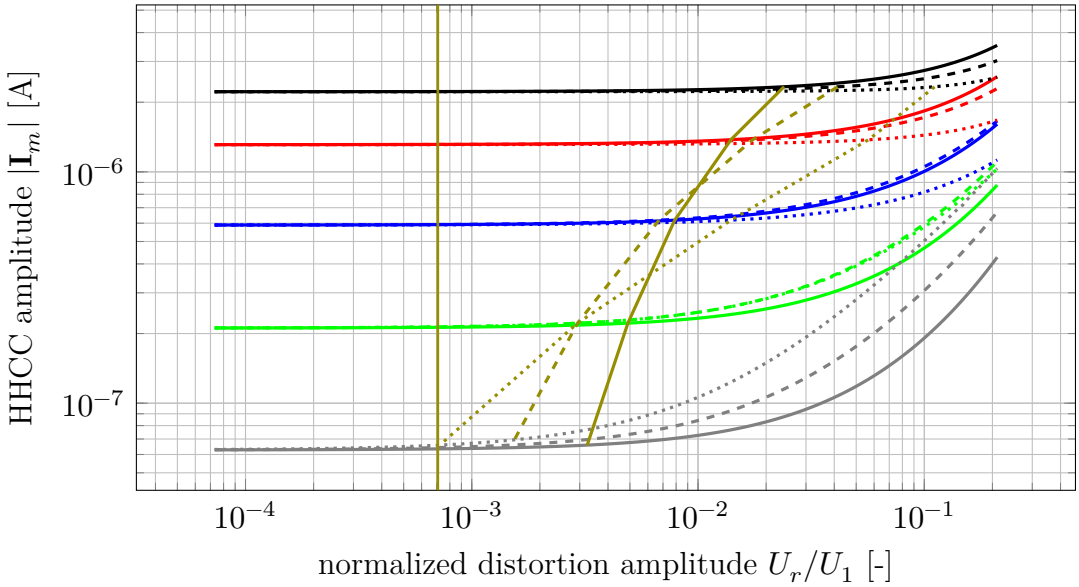

Figure C.1: Simulated change of HHCCs of mth order for a Schottky barrier due to distortion by an excitation voltage of rth harmonic order. The figure shows $m = 1$ (black) to $m = 5$ (gray) in case of $r = 2$ (solid), $r = 3$ (dashed), and $r = 5$ (dotted). Constant quantities are $U_0 = 0$, $U_1 = 80\,\text{mV}$, $I_s = 73.8\,\text{nA}$, and $nU_T = 24.9\,\text{mV}$. The chosen parameters are motivated by the experimental results in sec. 4.4. The straight vertical line represents the measured total harmonic distortion of the simple lock-in amplifier based dielectric spectroscopy setup of $-63\,\text{dB}$. The olive-colored curves connect all points with same r with a relative change of 5 % compared to the undisturbed value.

characteristic curve:

$$|\mathbf{I}_{m=r}| = \alpha \cdot a_{m=r} U_1^{m=r} + \beta \cdot a_1 U_{m=r}^1 + \ldots \quad \text{with real coefficients } \alpha, \beta. \tag{C.23}$$

A first observed trend is that the responses of higher order m get disturbed already by smaller distortion amplitudes. Consequently, measuring higher current orders requires a signal source of low total harmonic distortion (THD). By the presented numerical evaluation, one can estimate whether a fixed signal purity is sufficient to excite a certain harmonic order and a certain characteristic curve. According to fig. C.1, the total harmonic distortion of $-63\,\text{dB}$ observed in our experiments (sec. A.2) was sufficient to measure the first five current harmonics on the diode test device with a deviation of less than 5 %.

Since the vertical sequence of the curves for constant m in fig. C.1 follows no obvious rule, it is worth to investigate the current distortion for a constant distortion amplitude U_r as a function of m and r, which is shown in fig. C.2. Nevertheless, in commonly available signal generators, the distortion amplitude drastically decreases with increasing r, meaning that the low order excitations are the most crucial ones.

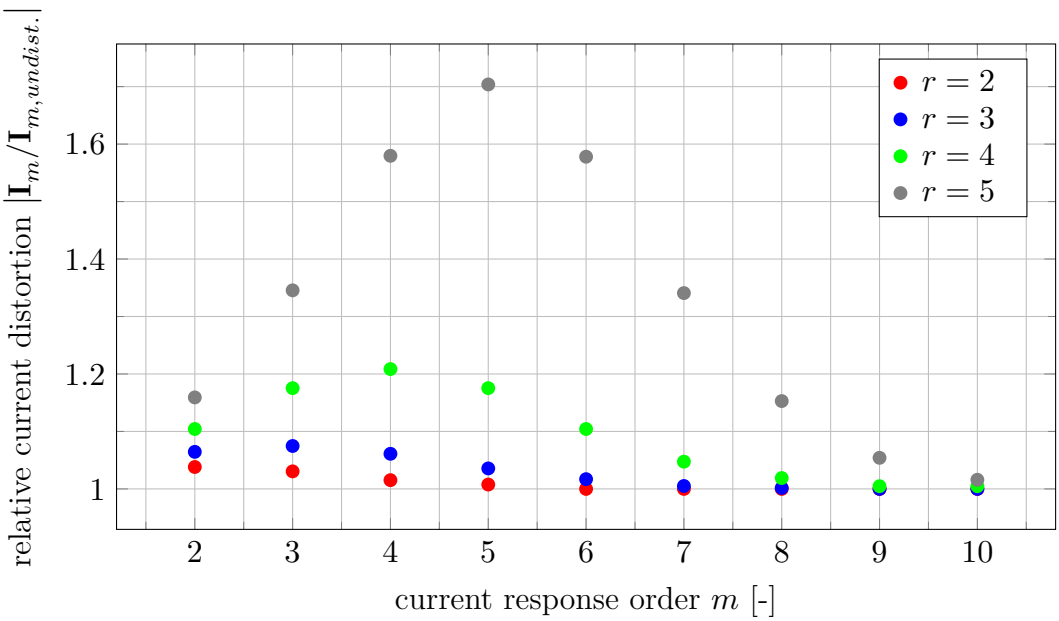

Figure C.2: Distortion of higher-harmonic currents I_m at fixed distortion amplitude $U_r = 0.82\,\mathrm{mV}$ with $U_1 = 80\,\mathrm{mV}$ and $U_0 = 0$.

As already observed in fig. C.1, the relative current distortion increases with increasing r. This can be explained qualitatively by the fact that the distortion voltage can influence a certain order m via a Taylor coefficient a_k of lower k with larger value. Furthermore, we observe a maximum distortion with respect to m in the already mentioned case of $m = r$ (equ. C.23). This is also encoded in fig. C.1 in the fact, that for constant $m \in \{2, 3, 5\}$, the most left crossing with an olive colored curve (5 % deviation already at small distortion amplitudes) is always the one with $m = r$. For practical applications we can conclude, that high-order current contributions are usually more susceptible to harmonic distortion (fig. C.1) and the distortion amplitudes are in real signals in general small, while this is vice versa for lower-order current contributions.

References

[1] Bureau International des Poids et Mesures, "SI Brochure: The International System of Units" tech. rep., Bureau International des Poids et Mesures, 2009.

[2] R. Burdett, "Amplitude Modulated Signals: The Lock-in Amplifier" in *Handbook of Measuring System Design*, ch. 181, John Wiley & Sons, 2005.

[3] J. Groß, *Linear regression*, vol. 175 of *Lecture notes in statistics*. Berlin: Springer, 2003.

[4] M. Tanabashi *et al.*, "Review of Particle Physics", Physical Review D *98* (3), 030001, 2018.

[5] V. Gopalan, V. Dierolf, and D. A. Scrymgeour, "Defect–Domain Wall Interactions in Trigonal Ferroelectrics", Annual Review of Materials Research *37* (1), 449–489, 2007.

[6] A. Mansingh and A. Dhar, "The AC conductivity and dielectric constant of lithium niobate single crystals", Journal of Physics D: Applied Physics *18* (10), 2059–2071, 1985.

[7] D. M. Evans, V. Garcia, D. Meier, and M. Bibes, "Domains and domain walls in multiferroics", Physical Sciences Reviews *5* (9), 20190067, 2020.

[8] J. Malmodin and D. Lundén, "The electricity consumption and operational carbon emissions of ICT network operators 2010-2015" tech. rep., Centre for Sustainable Communications, KTH Royal Institute of Technology, Stockholm, 2018.

[9] P. Messerli *et al.*, "Global Sustainable Developement Report 2019: The Future is Now – Science for Achieving Sustainable Development" tech. rep., United Nations, New York, 2019.

[10] G. Moore, "Cramming More Components Onto Integrated Circuits", Electronics *38* (8), 114–117, 1965.

[11] K. Rupp, "42 Years of Microprocessor Trend Data", 2018, `https://www.karlrupp.net/2018/02/42-years-of-microprocessor-trend-data/` (2021-09-09).

[12] S. Krohns, P. Lunkenheimer, S. Meissner, A. Reller, B. Gleich, A. Rathgeber, T. Gaugler, H. U. Buhl, D. C. Sinclair, and A. Loidl, "The route to resource-efficient novel materials", Nature Materials *10* (12), 899–901, 2011.

[13] T. Kämpfe, B. Wang, A. Haußmann, L.-Q. Chen, and L. M. Eng, "Tunable Non-Volatile Memory by Conductive Ferroelectric Domain Walls in Lithium Niobate Thin Films", Crystals *10* (9), 804, 2020.

[14] M. Schröder, A. Haußmann, A. Thiessen, E. Soergel, T. Woike, and L. M. Eng, "Conducting Domain Walls in Lithium Niobate Single Crystals", Advanced Functional Materials *22*, 3936–3944, 2012.

[15] C. Godau, T. Kämpfe, A. Thiessen, L. M. Eng, and A. Haußmann, "Enhancing the Domain Wall Conductivity in Lithium Niobate Single Crystals", ACS Nano *11* (5), 4816–4824, 2017.

[16] A. Thiessen, "Photoinduzierter Ladungstransport in komplexen Oxiden", PhD Thesis, Technische Universität Dresden, Dresden, 2013. urn: urn:nbn:de:bsz:14-qucosa-124227.

[17] T. Volk and M. Wöhlecke, *Lithium niobate defects, photorefraction and ferroelectric switching*. Berlin, Heidelberg: Springer, 2008.

[18] C. Thierfelder, S. Sanna, A. Schindlmayr, and W. G. Schmidt, "Do we know the band gap of lithium niobate?", physica status solidi c *7* (2), 362–365, 2010.

[19] S. Messerschmidt, A. Krampf, L. Vittadello, M. Imlau, T. Nörenberg, L. M. Eng, and D. Emin, "Small-Polaron Hopping and Low-Temperature (45–225 K) Photo-Induced Transient Absorption in Magnesium-Doped Lithium Niobate", Crystals *10* (9), 809, 2020.

[20] R. S. Weis and T. K. Gaylord, "Lithium niobate: Summary of physical properties and crystal structure", Applied Physics A *37* (4), 191–203, 1985.

[21] A. Haußmann, "UV-unterstützte Erzeugung ferroelektrischer Domänenmuster in Lithiumniobat zur selektiven Abscheidung von Adsorbaten", Diploma Thesis, Technische Universität Dresden, Dresden, 2006.

[22] A. Haußmann, "Ferroelektrische Lithografie auf magnesiumdotierten Lithiumniobat-Einkristallen", PhD Thesis, Technische Universität Dresden, Dresden, 2011. urn: urn:nbn:de:bsz:14-qucosa-66638.

[23] B. Faust, H. Müller, and O. Schirmer, "Free small polarons in $LiNbO_3$", Ferroelectrics *153* (1), 297–302, 1994.

[24] O. F. Schirmer, M. Imlau, C. Merschjann, and B. Schoke, "Electron small polarons and bipolarons in LiNbO3", Journal of Physics: Condensed Matter *21* (12), 123201, 2009.

[25] E. A. Eliseev, A. N. Morozovska, G. S. Svechnikov, V. Gopalan, and V. Y. Shur, "Static conductivity of charged domain walls in uniaxial ferroelectric semiconductors", Physical Review B *83* (23), 235313, 2011.

[26] S. Y. Xiao, T. Kämpfe, Y. M. Jin, A. Haußmann, X. M. Lu, and L. M. Eng, "Dipole-Tunneling Model from Asymmetric Domain-Wall Conductivity in $LiNbO_3$ Single Crystals", Physical Review Applied *10* (3), 034002, 2018.

[27] I. S. Akhmadullin, V. A. Golenishchev-Kutuzov, S. A. Migachev, and S. P. Mironov, "Low-temperature electrical conductivity of congruent lithium niobate crystals", Physics of the Solid State *40* (7), 1190–1192, 1998.

[28] R. Gerson, J. F. Kirchhoff, L. E. Halliburton, and D. A. Bryan, "Fundamental Mechanisms Of Photoconductivity In Magnesium Doped Lithium Niobate" in *Integrated Optical Circuit Engineering IV*, vol. 704, 221–226, SPIE, 1987.

[29] M. Schröder, X. Chen, A. Haußmann, A. Thiessen, J. Poppe, D. A. Bonnell, and L. M. Eng, "Nanoscale and macroscopic electrical ac transport along conductive domain walls in lithium niobate single crystals", Materials Research Express *1*, 035012, 2014.

[30] C. S. Werner, S. J. Herr, K. Buse, B. Sturman, E. Soergel, C. Razzaghi, and I. Breunig, "Large and accessible conductivity of charged domain walls in lithium niobate", Scientific Reports *7* (1), 9862, 2017.

[31] A. S. Lofty, "Investigation of the factors that affect the stability of enhanced domain wall conductivity in single-crystalline lithium niobate", Master's Thesis, Technische Universität Dresden, Dresden, 2021.

[32] R. Hoffmann, "How Chemistry and Physics Meet in the Solid State", Angewandte Chemie International Edition *26* (9), 846–878, 1987.

[33] S. Baranovski, *Charge transport in disordered solids with applications in electronics*. Chichester, England: Wiley, 2006.

[34] A. Miller and E. Abrahams, "Impurity Conduction at Low Concentrations", Physical Review *120* (3), 745–755, 1960.

[35] J. Schnakenberg, "Polaronic Impurity Hopping Conduction", physica status solidi (b) *28* (2), 623–633, 1968.

[36] N. F. Mott, "Conduction in non-crystalline materials", Philosophical Magazine *19* (160), 835–852, 1968.

[37] A. L. Efros and B. I. Shklovskii, "Coulomb gap and low temperature conductivity of disordered systems", Journal of Physics C: Solid State Physics *8* (4), L49–L51, 1975.

[38] M. Born and R. Oppenheimer, "Zur Quantentheorie der Molekeln", Annalen der Physik *389* (20), 457–484, 1927.

[39] N. F. Mott and E. A. Davis, *Electronic Processes in Non-Crystalline Materials.* International series of monographs on physics, Oxford: University Press, 2012.

[40] R. Laiho, K. G. Lisunov, E. Lähderanta, M. A. Shakhov, V. N. Stamov, V. S. Zakhvalinskii, V. L. Kozhevnikov, I. A. Leonidov, E. B. Mitberg, and M. V. Patrakeev, "Mechanisms of hopping conductivity in weakly doped $La_{1-x}Ba_xMnO_3$", Journal of Physics: Condensed Matter *17* (21), 3429–3444, 2005.

[41] P. Reichenbach, T. Kämpfe, A. Haußmann, A. Thiessen, T. Woike, R. Steudtner, L. Kocsor, Z. Szaller, L. Kovács, and L. M. Eng, "Polaron-Mediated Luminescence in Lithium Niobate and Lithium Tantalate and Its Domain Contrast", Crystals *8* (5), 214, 2018.

[42] E. H. Rhoderick and R. H. Williams, *Metal-semiconductor contacts.* No. 19 in Monographs in electrical and electronic engineering, Oxford: Clarendon Press, 1988.

[43] W. Shockley, "The theory of p-n junctions in semiconductors and p-n junction transistors", The Bell System Technical Journal *28* (3), 435–489, 1949.

[44] U. Tietze, C. Schenk, and E. Gamm, *Electronic Circuits.* New York: Springer, 2008.

[45] N. Meyer, G. F. Nataf, and T. Granzow, "Field induced modification of defect complexes in magnesium-doped lithium niobate", Journal of Applied Physics *116* (24), 244102, 2014.

[46] Y. Kim, H. Song, F. Strigl, H.-F. Pernau, T. Lee, and E. Scheer, "Conductance and Vibrational States of Single-Molecule Junctions Controlled by Mechanical Stretching and Material Variation", Physical Review Letters *106* (19), 196804, 2011.

[47] S. Krohns, "Grenzflächenpolarisationen in Übergangsmetalloxiden: Von der Grundlagenforschung zur Anwendung", PhD Thesis, Universität Augsburg, Augsburg, 2010. urn: urn:nbn:de:bvb:384-opus-15823.

[48] E. Ruff, S. Krohns, M. Lilienblum, D. Meier, M. Fiebig, P. Lunkenheimer, and A. Loidl, "Conductivity Contrast and Tunneling Charge Transport in the Vortexlike

Ferroelectric Domain Patterns of Multiferroic Hexagonal $YMnO_3$", Physical Review Letters *118* (3), 036803, 2017.

[49] P. Horowitz and W. Hill, *The Art of Electronics | Electronics for physicists.* New York, NY: Cambridge University Press, 2015.

[50] U. Nandi, D. Jana, and D. Talukdar, "Scaling description of non-ohmic direct current conduction in disordered systems", Progress in Materials Science *71*, 1–92, 2015.

[51] M. Schröder, "Conductive domain walls in ferroelectric bulk single crystals", PhD Thesis, Technische Universität Dresden, Dresden, 2014. urn: urn:nbn:de:bsz:14-qucosa-142571.

[52] Oxford Instruments, "OptistatDN, Variable Liquid Nitrogen Cryostat", Tubney Woods, Oxfordshire, UK, 2000.

[53] K. Ayeva and S. Kasampalis, *Mastering Python design patterns - a guide to creating smart, efficient, and reusable software.* Birmingham, UK: Packt Publishing, 2018.

[54] E. Gamma, R. Helm, R. Johnson, and J. Vlissides, *Design Patterns: Elements of Reusable Object Oriented Software.* Boston, MA: Addison-Wesley, 1994.

[55] J. Schilling *et al.*, "Die verschiedenen Phasen der COVID-19-Pandemie in Deutschland: Eine deskriptive Analyse von Januar 2020 bis Februar 2021", Bundesgesundheitsblatt - Gesundheitsforschung - Gesundheitsschutz *64* (9), 1093–1106, 2021.

[56] T. Kämpfe, P. Reichenbach, M. Schröder, A. Haußmann, L. M. Eng, T. Woike, and E. Soergel, "Optical three-dimensional profiling of charged domain walls in ferroelectrics by Cherenkov second-harmonic generation", Physical Review B *89* (3), 035314, 2014.

[57] B. Kirbus, C. Godau, L. Wehmeier, H. Beccard, E. Beyreuther, A. Haußmann, and L. M. Eng, "Real-Time 3D Imaging of Nanoscale Ferroelectric Domain Wall Dynamics in Lithium Niobate Single Crystals under Electric Stimuli: Implications for Domain-Wall-Based Nanoelectronic Devices", ACS Applied Nano Materials *2* (9), 5787–5794, 2019.

[58] J. Zhao, M. Rüsing, M. Roeper, L. M. Eng, and S. Mookherjea, "Poling thin-film x-cut lithium niobate for quasi-phase matching with sub-micrometer periodicity", Journal of Applied Physics *127* (19), 193104, 2020.

[59] M. A. Branch, T. F. Coleman, and Y. Li, "A Subspace, Interior, and Conjugate Gradient Method for Large-Scale Bound-Constrained Minimization Problems", SIAM Journal on Scientific Computing *21* (1), 1–23, 1999.

[60] R. Johansson, *Numerical Python, Scientific Computing and Data Science Applications with Numpy, SciPy and Matplotlib.* New York: Apress, 2019.

[61] R. G. Kirchhoff, "Ueber den Durchgang eines elektrischen Stromes durch eine Ebene, insbesondere durch eine kreisförmige", Annalen der Physik und Chemie *64* (4), 497, 1845.

[62] M. Grundmann, *The physics of semiconductors. An introduction including nanophysics and applications.* Graduate texts in physics, Cham, CH: Springer, 2016.

[63] S. Gambhir, A. Singh, and M. Singh, "Intrinsic nonlinearity of a PN-junction diode and higher order harmonic generation", Physics Education *34* (2), 3, 2018.

[64] M. P. Campbell, J. P. V. McConville, R. G. P. McQuaid, D. Prabhakaran, A. Kumar, and J. M. Gregg, "Hall effect in charged conducting ferroelectric domain walls", Nature Communications *7* (1), 13764, 2016.

[65] B. Wolba, J. Seidel, C. Cazorla, C. Godau, A. Haußmann, and L. M. Eng, "Resistor Network Modeling of Conductive Domain Walls in Lithium Niobate", Advanced Electronic Materials *4* (1), 1700242, 2018.

[66] T. S. Holstad *et al.*, "Application of a long short-term memory for deconvoluting conductance contributions at charged ferroelectric domain walls", npj Computational Materials *6* (1), 163, 2020.

[67] Z. Chen, L. He, F. Zhang, J. Jiang, J. Meng, B. Zhao, and A. Jiang, "The conduction mechanism of large on/off ferroelectric diode currents in epitaxial (111) $BiFeO_3$ thin film", Journal of Applied Physics *113* (18), 184106, 2013.

[68] Keysight Technologies, "Impedance Measurement Handbook - A Guide to Measurement Technology and Techniques", Santa Rosa, CA, 2020. Keysight publication number: 5950-3000.

[69] S. Butterworth, "On the theory of filter amplifiers", Wireless Engineer *7* (6), 536–541, 1930.

[70] S. Groner, "Low Distortion Oscillator Design", Master's Thesis, Zurich University of the Arts, Zurich, CH, 2010.

[71] P. F. Van Oorschot and J. W. Pustjens, "The resistor guide, the complete guide to the world of resistors", 2012. `https://www.resistorguide.com` (2022-01-29).

[72] W. Weißgerber, *Elektrotechnik für Ingenieure 3: Ausgleichsvorgänge, Fourieranalyse, Vierpoltheorie. Ein Lehr- und Arbeitsbuch für das Grundstudium.* Wiesbaden: Springer, 2018.

[73] B. D. Hall, "On the propagation of uncertainty in complex-valued quantities", Metrologia *41* (3), 173–177, 2004.

[74] H. Fischer and H. Kaul, *Mathematik für Physiker Band 2: Gewöhnliche und partielle Differentialgleichungen, mathematische Grundlagen der Quantenmechanik*, vol. 2. Wiesbaden: Vieweg+Teubner, 2008.

[75] I. S. Gradštejn and I. M. Ryžik, *Table of integrals, series, and products.* San Diego, CA: Elsevier, 2007.

[76] M. Abramowitz and I. A. Stegun, *Handbook of mathematical functions - with formulas, graphs, and mathematical tables.* No. 55 in Applied Mathematics Series, Washington, DC: U. S. Government Printing Office, 1972.

Acknowledgment

I gradefully acknowledge the following persons who contributed in numerous different ways to this thesis:

- **Prof. Dr. Lukas Eng**, for promoting extensively the topic of nonlinear and ac conductivity on LNO domains walls I was working on during the last years at the institute of applied physics and supervising this thesis as part of this track.
- **Dr. Elke Beyreuther**, for her all-encompassing, motivated and kind help on experimental design, data interpretation up to intensive proofreading of the manuscript.
- **PD Dr. Stephan Krohns**, for teaching me on the theoretical concepts and practical realizations of dielectric spectroscopy and his willingness to act as a referee for this thesis.
- **Dr. Michael Rüsing**, for sharing his overwhelming knowledge on lithium niobate and contributing a lot to my current picture on this material.
- **Julius Ratzenberger** and **Peter Hegarty**, for the great teamwork on smaller and larger projects starting from data interpretation up to sustainable design of hopefully long-term usable experimental setups.
- **Ralf Raupach**, for intensive technical support and numerous valueable discussions on electronics also beyond the topics involved in this projects.
- **Ekta Singh**, **Henrik Beccard** and all other members of the **Ferroix** and **SPM^2 group**, for their help and ideas to bring this project forward, providing a kind working atmosphere and maintain, as far as possible also in difficult times, a vivid "Mensa culture".
- **Dr. Susann** and **PD Dr. Peter Zahn**, for proofreading the manuscript and providing the opportunity of having a distance of 322 m between home-office and lab, which turned out especially during the phases of more restrictive Corona rules as a valuable geostrategic advantage.
- **Helen Vogt** and **Felix Kunzmann**, who accompanied me on numerous climbing trips and helped a lot to refresh my mental abilities.

Erklärung

Hiermit erkläre ich, dass ich diese Arbeit im Rahmen der Betreuung am Institut für Angewandte Physik der TU Dresden ohne unzulässige Hilfe Dritter verfasst und alle Quellen als solche gekennzeichnet habe.

Manuel Zahn
Dresden, 31.01.2022